MASSACHUSETTS INSTITUTE OF TECHNOLOGY

The RESEARCH LABORATORY *of* ELECTRONICS

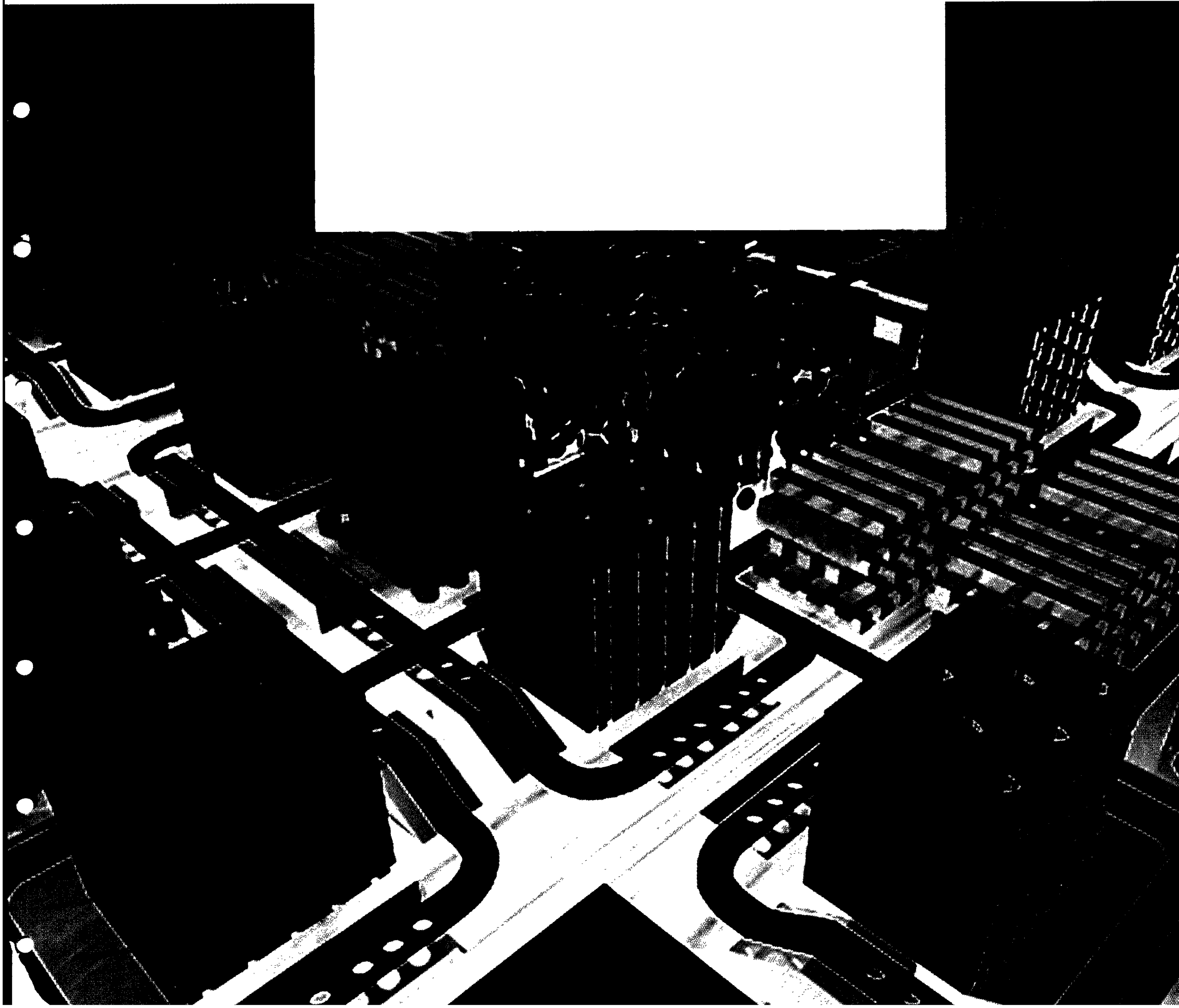

Gravitational Lens 0218 + 357 as a Probe of the Geometry of the Universe

By: Aaron S. Gohen

RLE Technical Report No. 641

June 12, 2000

Gravitational Lens 0218 + 357 as a Probe of the Geometry of the Universe

By: Aaron S. Gohen

RLE Technical Report No. 641

June 12, 2000

Gravitational Lens 0218+357 as a Probe of the Geometry of the Universe

by

Aaron S. Cohen

Bachelor of Science in Physics
Bachelor of Science in Mathematics
University of California, Santa Barbara
June, 1995

Submitted to the Department of Physics
in partial fulfillment of the requirements for the degree of

Doctor of Philosophy

at the

MASSACHUSETTS INSTITUTE OF TECHNOLOGY

September 2000

Author ....Aaron Cohen..
Department of Physics
June 12, 2000

Certified by....Jacqueline N. Hewitt....................
Jacqueline N. Hewitt
Professor of Physics
Thesis Supervisor

Accepted by ....Thomas J. Greytak
Thomas J. Greytak
Professor, Associate Department Head for Education
Chairman, Physics Graduate Committee

Gravitational Lens 0218+357 as a Probe of the Geometry of the Universe

by

Aaron S. Cohen

Submitted to the Department of Physics
on June 12, 2000, in partial fulfillment of the
requirements for the degree of
Doctor of Philosophy

Abstract

A gravitational lens is the result of a massive object lying along the line of sight to a more distant object, such as a quasar, so that the light from the quasar is deflected before it reaches earth. Often the distortion caused by the lensing mass can cause multiple images of the same object to be seen. Such systems provide an opportunity to measure the effective angular diameter distance to high redshift objects, and thereby deduce Hubble's Constant (H_o). There are two steps to this procedure. First, the mass distribution of the lensing object must be determined so that a model can be made of the relationship between the angular diameter distance to the lens and the difference in path lengths among the multiple images. Second, this path length difference must be measured in the form of a time delay between flux variations among the multiple components.

In this thesis, I present a time delay measurement of the gravitational lens 0218+357 as well as VLBA observations of this lens which are used to model the mass distribution of the lensing object. With the time delay and lens model, we determine that Hubble's Constant is in the range 9 km/s/Mpc $\leq H_o \leq$ 68 km/s/Mpc at 95% confidence. Cosmological implications are discussed.

Thesis Supervisor: Jacqueline N. Hewitt
Title: Professor of Physics

Acknowledgments

There are many people whose help and advice provided me with the means to conduct the research that makes up this thesis. First I would like to thank my advisor, Jackie Hewitt, who gave me the opportunity to work on this project and the guidance to be successful. Jackie also was responsible for me spending the final stages of my thesis research at NRAO in Socorro, New Mexico, which has an incredible experience for which I am very grateful. I would also like to thank the other members of my thesis committee, Paul Schechter and Alan Guth. Paul was always available for advice or to chat, and his general enthusiasm for astrophysics was quite contagious. Alan, who only recently became involved in this thesis, has shown genuine interest and an extremely quick grasp of the details in this project which has made it fun to explain things to him. I also appreciate the help of other MIT students and former students who provided me with advice, fun times and, when necessary, empathy including Chris Moore, Debbie Haarsma, Andre Fletcher, Max Avruch, Charlie Katz, Froney Crawford, Josh Winn and Cathy Trotter. I would also like to thank Rick Perley who was my co-advisor at NRAO, and who always provided interesting perspective and fun conversations. Miller Goss was also very supportive. Many other people at NRAO were very helpful in teaching me the finer techniques of VLBI observing including Ketan Desai, Leonia Kogan, Greg Taylor, Jim Ulvestad and Craig Walker. Special thanks goes to Chris Kochanek at Harvard who provided not only the computer code for LensClean, but also a great deal of advice and guidance in its use and subtleties.

My office mates at NRAO, Cornelia Lang, Chris Fassnacht, Kumar Golap, Neal Miller, Geoff Bower and Marc Verheijen, provided me with useful companionship during my days in the New Mexico desert. I would also like to thank Boguslaw Zdzieblo and Albert Chan for being such good friends. And of course, to my family, including my grandparents, aunts, uncles, cousins, siblings and especially my parents who I always knew were rooting for me from California, I am also extremely grateful.

Contents

List of Figures

List of Tables

Chapter 1

Introduction

1.1 What is a Gravitational Lens?

1.1.1 Basic Concept.

According to Albert Einstein's theory of general relativity, the perceived force of gravity is a result of the curvature of space-time by massive objects. Light, which normally travels along a straight line path, is deflected when it travels through a region of curved space. Therefore, the curved space in the vicinity of a very massive object acts like a lens and can bend, concentrate or spread light rays that pass through it.

It then follows that light paths should be bent by the gravitational field of the Earth as well. This is in fact the case; however, the enormous speed of light makes this difficult to observe. For example, if one were to aim a laser beam perfectly horizontal to the ground at a target that was 300 meters away, the light would take only one millionth of a second to reach its target. The gravitational pull of the earth will cause the light to hit somewhat lower than its target, but only by an amount that is less than the width of a single atom! So the effect of gravity is not noticeable in any normal situation on Earth. Even an object as massive as the Sun can only cause very small deflections of passing starlight.

When very large masses are involved, such as an entire galaxy or even a cluster

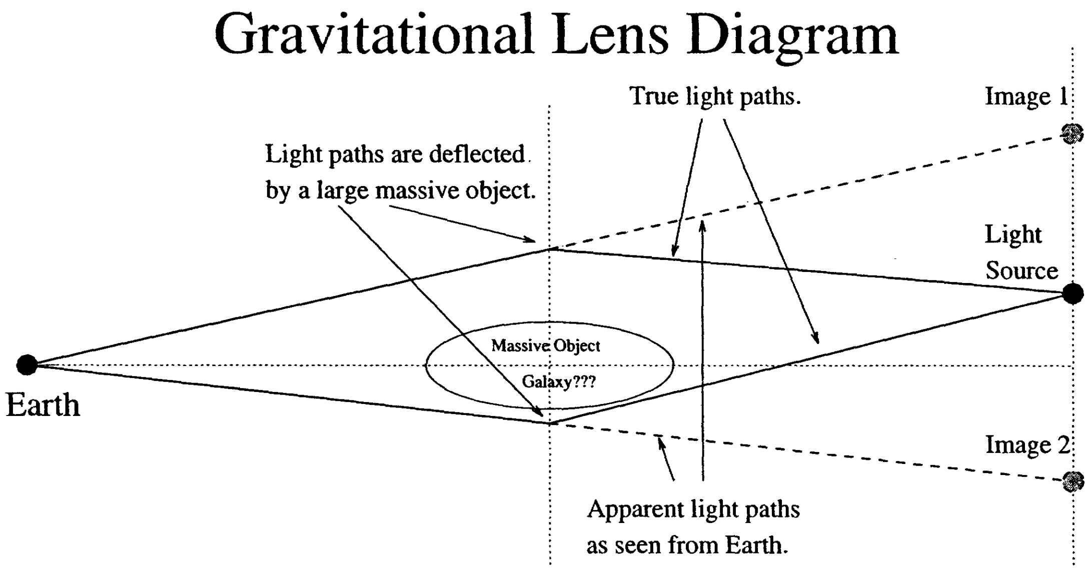

Figure 1-1: The basic concept behind gravitational lensing. The lensing mass bends the light emitted by the source so that two (or more) separate paths reach Earth. An observer will then see the two (or more) images of the same source, both of which are offset from the true source position.

of galaxies, the lensing effect can be quite striking. In some instances such a massive object lies along the line of sight to a more distant object. When this happens, the light rays from the background object are bent and distorted before they reach Earth. Often the distortion caused by the lensing mass can cause multiple images of the same background object to be seen (see Figure 1-1). Astronomers refer to this phenomenon as a gravitational lens. Such objects had long been predicted, but it was not until 1979 that the first gravitational lens, named by its coordinates 0957+561, was discovered (Walsh Carswell & Weymann 1979). There are now more than 50 such objects confirmed as gravitational lenses.

1.1.2 Review of Cosmology

Gravitational lensing in which multiple images can be resolved by existing telescopes occurs only for objects at distances that are a significant fraction of the size of the observable universe. For this reason, the structure and dynamics of the universe as a whole have a large effect on gravitational lensing. This makes gravitational lenses a valuable tool for studying cosmology. In order to demonstrate this, it is necessary to summarize some of the basics of quantitative cosmology.

The space-time structure of the universe as a whole can be described by the Robertson-Walker metric which is simply the most general space-time metric which is both homogeneous and isotropic. It has the form:

$$ds^2 = dt^2 - a(t)\left[\frac{dr^2}{1-kr^2} + r^2(d\theta^2 + \sin^2\theta d\phi^2)\right] \tag{1.1}$$

where k is the curvature of space and $a(t)$ is the scale factor of the universe. As $a(t)$ changes in time, space expands or contracts. At the present time, $a(t)$ is increasing, causing the distances between galaxies in the universe to increase with time. The redshift of an object, z, is directly the result of the changing scale factor. If the light we observe from the object was emitted at time t, and time at present is t_o, then the redshift is:

$$z \equiv \frac{a(t_o)}{a(t)} - 1 \tag{1.2}$$

The cosmological equations governing how $a(t)$ evolves in time in a universe dominated by non-relativistic matter are:

$$\frac{\ddot{a}}{a} = -\frac{4}{3}\pi G\rho + \frac{\lambda}{3} \tag{1.3}$$

$$\left(\frac{\dot{a}}{a}\right)^2 = \frac{8}{3}\pi G\rho - \frac{k}{a^2} + \frac{\lambda}{3} \tag{1.4}$$

where G is the Newtonian gravitational constant, ρ is the matter density of the universe and λ is a constant term related to the energy density of the vacuum which causes "negative" pressure and increases the expansion rate.

The expansion rate of the universe, H, is directly related to the rate of change of the scale factor, $a(t)$, in the following way:

$$H_o \equiv \frac{\dot{a}(t)}{a(t)} \tag{1.5}$$

where H can change throughout the lifetime of the universe. Typically the present day values of cosmological parameters are denoted by a subscript "o" and so the present day expansion rate, is denoted as H_o and is called Hubble's Constant.

If there is no cosmological constant ($\lambda = 0$) then there is a critical matter density, ρ_c, above which the universe is gravitationally bound and will eventually begin to contract:

$$\rho_c = \frac{3H_o^2}{8\pi G} \tag{1.6}$$

It is therefore convenient to define a normalized matter density:

$$\Omega_o \equiv \frac{\rho_o}{\rho_c} = \frac{8\pi G \rho_o}{3H_o^2} \tag{1.7}$$

If there is no matter ($\Omega_o = 0$) then there is a similar critical value for the cosmological constant, λ_c, which allows us to similarly normalize the cosmological constant:

$$\Lambda_o \equiv \frac{\lambda_o}{\lambda_c} = \frac{\lambda_o}{3H_o^2} \tag{1.8}$$

The cosmological constants Ω_o and Λ_o determine how the scale factor, $a(t)$ changes with time and therefore how the universe will evolve and has evolved. Together, they also determine the curvature of space-time:

$$\begin{gathered}\Omega_o + \Lambda_o > 1 \Rightarrow \text{Spacetime has negative curvature}\\ \Omega_o + \Lambda_o = 0 \Rightarrow \text{Spacetime is flat (Euclidean)}\\ \Omega_o + \Lambda_o < 1 \Rightarrow \text{Spacetime has positive curvature}\end{gathered}$$

1.1.3 Cosmological Distances and Gravitational Lenses

Gravitational lensing occurs when the lensing object and the source are at cosmological distances from the observer. Objects are said to be at cosmological distances when the time it took their light to reach us is a significant fraction of the age of the universe. Thus the light we receive has traveled for billions of years through expanding and possibly curved spacetime. Before describing quantitatively how gravitational lenses work, it is necessary to define precisely what we mean by distance in a universe that is vast, expanding and possibly consists of curved space. Normally we can imagine the distance between two points in space as the length of a string used to connect them in a straight line. However, we see objects only by the light they emit which takes time to travel to us. Objects at cosmological distances are separated from us not only in space but also in time, because we only see the object as it existed when the light we are now receiving from it was emitted. How do we define the distance to an object we are looking at when we are seeing it where it was billions of years ago and in a universe that has expanded significantly since that time? In addition, for a curved universe, it is not immediately obvious how we even define a straight line.

One way to define distance for cosmological objects is called the lookback time. Lookback time is simply how far back in time was the light we now observe from this object emitted. If the present time (now) is t_o and if the light we see from an object was emitted at time t, then the lookback time is $t_o - t$. The lookback "distance" is simply the lookback time multiplied by the speed of light. This is perhaps the most intuitively satisfying way of defining distance, and will be referred to as the "true" distance or just the distance throughout this thesis.

Another definition of cosmological distance, which may be less intuitive but is much easier to calculate and to observe, is called angular diameter distance. Angular diameter distance is defined for an object of known physical size, R, and observed angular size, θ, as:

$$D_{ad} \equiv \frac{R}{\theta} \tag{1.9}$$

This, of course, is an exact way to calculate "true" distance in flat and static Euclidean space. However, in a curved or dynamic universe, this formula no longer results in the "true" distance, but is still a very useful quantity. Angular diameter distance is particularly useful for the modeling of gravitational lenses.

1.1.4 Quantitative Explanation of Lensing.

In order to make quantitative predictions about gravitational lensing one must consider the nature in which gravitational fields distort space-time. In the limit of a weak gravitational field, ϕ, the space-time metric is the following:

$$ds^2 = (1 + \frac{2\phi}{c^2})c^2 dt^2 - (1 - \frac{2\phi}{c^2})\delta_{\alpha\beta} dx^\alpha dx^\beta \quad . \tag{1.10}$$

For light, $ds^2 = 0$, so in the case of one dimension, we have:

$$(1 + \frac{2\phi}{c^2})c^2 dt^2 = (1 - \frac{2\phi}{c^2})dx^2 \tag{1.11}$$

To first order in ϕ, we get:

$$\frac{dx}{dt} = \frac{c}{(1 - \frac{2\phi}{c^2})} \tag{1.12}$$

So the speed of light appears to an outside observer to be slowed down by a factor of $(1 - \frac{2\phi}{c^2})^{-1}$. In this way, we can think of the gravitational potential as giving space an effective index of refraction, $n = 1 - \frac{2\phi}{c^2}$, for light. Now we can apply Fermat's Principle from optics, which states that light will travel only along paths for which the travel time is an extremum. The travel time of light along a given path is equal to the following line integral:

$$\tau = \int \frac{n(\vec{x})}{c} dl \tag{1.13}$$

When this principle is applied to a situation such as that in Figure 1-1, it is useful to start off with some reasonable approximations. In all known gravitational lenses, the deflection of light is extremely small, about six arcseconds or less. Therefore, we can approximate this bending as an instantaneous deflection that occurs at the moment the light passes through the image plane (see Figure 1-2). Since all paths we need to consider begin at the light source and end at the observer, the travel time, τ, can be considered a function only of the point at which the path intersects the image plane. This is referred to as the "Thin Lens" approximation.

According to Fermat's Principle, images will appear only at points (x, y) on the

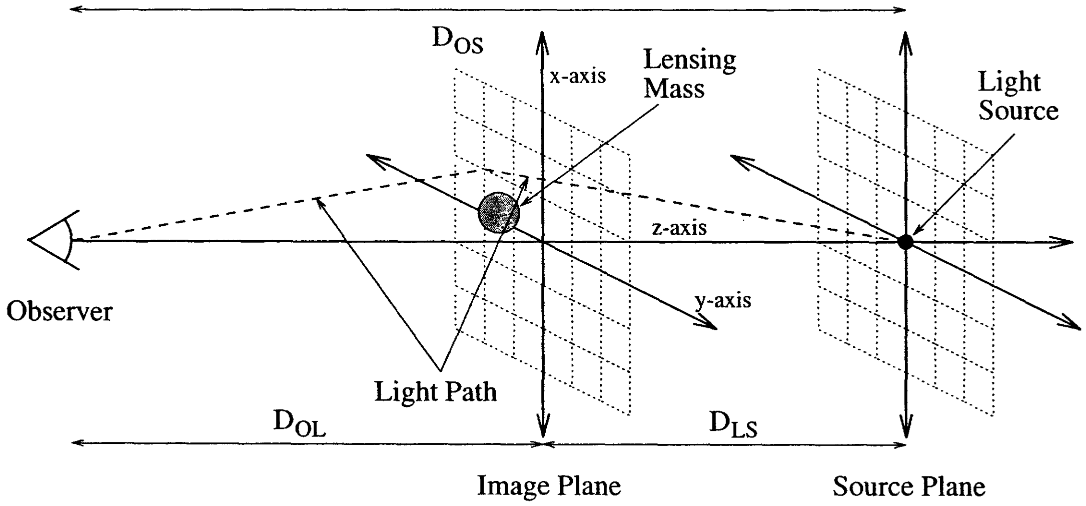

Figure 1-2: An idealized picture of the bending of light by a gravitational lens. All of the bending takes place as the light passes through the image plane. Therefore, an observer will see the object as if it were in the position at which the light path intersects the image plane, rather then its true position as shown in the source plane. The gravitational potential that a photon will "feel" as it takes this trajectory can be approximated as that it would feel if it traveled along a line parallel to the z-axis through the image plane at a given point (x,y). These approximations are valid only because the bending angle is in reality extremely small. For the sake of visual clarity, the bending angle is depicted in this diagram as far larger than it really is.

image plane for which:

$$\frac{d\tau}{dx} = \frac{d\tau}{dy} = 0 \tag{1.14}$$

Rather than directly evaluating Equation 1.13, it is useful to separate the travel time, τ, into the following components:

$$\tau = \tau_o + \tau_{geometry} + \tau_{gravity} \tag{1.15}$$

where τ_o is the travel time for an undeflected light path in the case that there is no lensing mass, $\tau_{geometry}$ is the increase in travel time due to the extra distance in the real light path over a straight line path, and $\tau_{gravity}$ is the increase in travel time due to the gravitationally induced effective index of refraction along the light path.

Let us name the position at which the true light path intersects the lens plane with the vector $\vec{r}$. Let us also name the position at which a straight line between the observer and the source intersects the image plane as $\vec{s}$. Then if we also use the quantities labeled in Figure 1-2, we can immediately calculate the travel time term $\tau_{geometry}$, to second order in $r_x - s_x$ and $r_y - s_y$ as:

$$\tau_{geometry}(x,y) = \frac{1}{2c}\left(1+z_L\right)\frac{D_{OS}}{D_{OL}D_{LS}}|\vec{r}-\vec{s}|^2 \tag{1.16}$$

where z_L is the redshift of the lens, and with the convention that the point $(x,y) = (0,0)$ will be located where the image plane intersects the straight line connecting the observer to the source. The term $(1+z_L)$ is included to convert $\tau_{geometry}(x,y)$ from the restframe of the lens to that of the Earth. These equations were derived assuming a flat, Euclidean geometry. They are valid for curved cosmologies only when the distances, D_{OS}, D_{OL} and D_{LS} are angular diameter distances. (Here, D_{LS} is the angular diameter distance measured by an observer at the lens at the time the light passed the lens.)

The remaining term, $\tau_{gravity}$, depends on the mass distribution of the lensing object. If we rely on the assumption that the path deflection by the lensing object is extremely small, we can form the following general expression for $\tau_{gravity}$ for a lens gravitational potential, ϕ:

$$\tau_{gravity}(x,y) = \frac{2}{c^3}\left(1+z_L\right)\int_{w_b}^{w_a}\phi(x,y,w)dw \tag{1.17}$$

Again, the term $(1+z_L)$ is included to convert $\tau_{gravity}(x,y)$ into the restframe of the Earth rather than that of the lens in which the gravitational potential, $\phi(\vec{x})$, is having its effect. The limits of integration, w_a and w_b, must enclose the region in which different possible light paths will "feel" different parts of the potential. Far from the lens, the potential is practically the same for all paths. As long as this condition is met, the actual values of the limits of integration are unimportant. This is because we are only interested in differences in $\tau_{gravity}(x,y)$ among the various paths, and so extending the integrals beyond the point where the various paths pass through non-negligibly different potentials will not change the difference in time delays.

We can simplify the above formulas with a change of notation. First we define a new quantity called the effective potential:

$$\psi(x,y) \equiv \frac{2D_{LS}}{c^2 D_{OL} D_{OS}} \int \phi(x,y,w)dw \tag{1.18}$$

which is just a scaled two-dimensional potential formed by integrating the three-dimensional potential along the line of sight. Also, instead of using length coordinates in the image plane, we will use angular coordinates. Thus we have:

$$\vec{\theta} = (\theta_x, \theta_y) = \frac{1}{D_{OL}}(x,y) \tag{1.19}$$

Now we plug in Equations 1.16, 1.17 and 1.18 into Equation 1.15 to get:

$$\tau(\vec{\theta}) = \tau_o + (1+z_L)\frac{D_{OL} D_{OS}}{2cD_{LS}}\left[|\vec{\theta} - \vec{\beta}|^2 - 2\,\psi(\vec{\theta})\right] \tag{1.20}$$

where $\vec{\beta}$ is the angular position of the source object in the absence of lensing. One convenient property of the effective potential is that its gradient at the image position is equal to the difference between the image position and the true source position in the absence of lensing as follows:

$$\vec{\nabla}\,\psi(\vec{\theta}) = \vec{\beta} - \vec{\theta} \tag{1.21}$$

This allows us to rewrite Equation 1.20 so that the light travel time can be expressed entirely in terms relating to the effective potential and its derivatives:

$$\tau(\vec{\theta}) = \tau_o + (1+z_L)\frac{D_{OL} D_{OS}}{2cD_{LS}}\left[|\vec{\nabla}\,\psi(\vec{\theta})|^2 - 2\,\psi(\vec{\theta})\right]. \tag{1.22}$$

Knowing $\psi(\vec{\theta})$ for a given lensing object, we can then plot τ as a function of $\vec{\theta}$ in the image plane. According to Equation 1.14, images of the source object will appear at places in the image plane where the function $\tau(\vec{\theta})$ (calculated from Equation 1.20) is a local maximum, local minimum or a saddle point. In figure 1-3, several lensing scenarios are shown along with the resulting images as seen by the observer. Notice

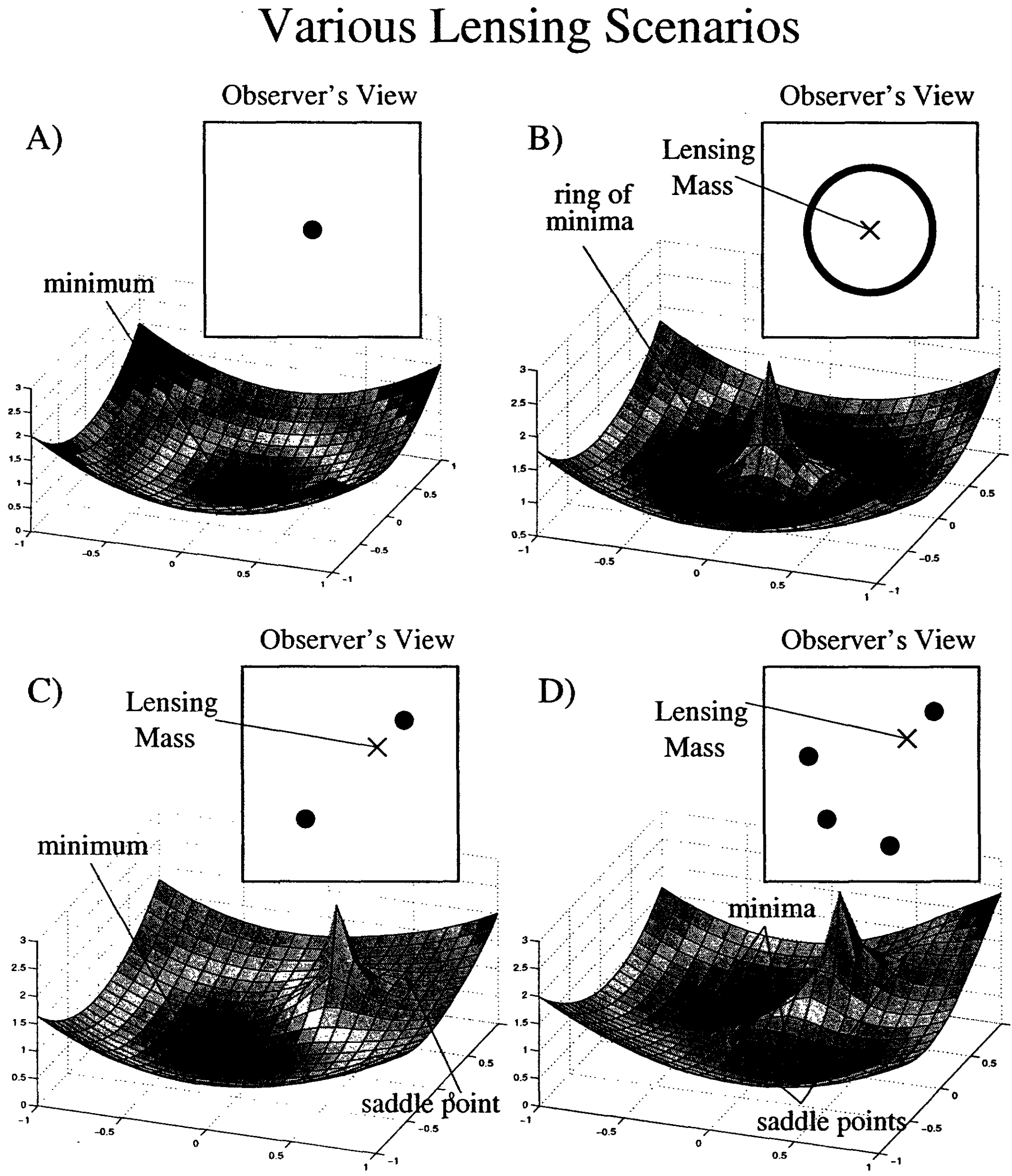
Various Lensing Scenarios

Figure 1-3: The τ-surfaces of various lensing configurations are shown here, along with the resulting image positions that an observer would see in the sky. In case A, there is no lensing mass, so the observer sees the undistorted image of the background light source. In case B, there is a point mass located exactly along the line of sight to the background object. This results in an Einstein ring image. Case C is similar to case B except that the point mass is not quite lined up with the background source. This results in two images of the same background source. Case D is like case C except that instead of a point mass, we have an elliptical mass distribution, which can cause the background object to be quadruply imaged.

that, in addition to determining where the images will fall, the τ-surface also predicts the time delays among the images. Also, the curvature at these points determines the magnification of the background source. So knowing the mass distribution of the lensing object, and thus $\phi(\vec{x})$, we can deduce the image positions, relative magnifications and time delays. In gravitational lens modeling we seek to reverse this procedure. Using empirically determined factors such as the image positions and flux ratios, the lens position and the redshifts of the lens and source, we seek to model the mass distribution of the lensing object.

1.2 What Can We Learn from Gravitational Lenses?

The field of cosmology, which deals with the overall structure and evolution of the universe, can potentially be advanced greatly by the study of gravitational lenses. This is for two main reasons. First, strong gravitational lensing (in which the image separation is great enough to resolve with existing telescopes) only occurs when the foreground object is extremely massive, on the scale of an entire galaxy or larger. Currently among the primary unknown factors in cosmology are the mass density of the universe and the nature in which this mass is distributed. All astronomers can observe directly is the distribution of light sources in the universe. Lately, the evidence seems to be mounting that the light distribution is very different from the mass distribution. Studying a single gravitational lens allows us to measure directly the mass distribution in the lensing object by its gravitational effect on the light from the background source. Studying the overall density of gravitational lenses in the sky allows us to estimate the number density of such massive objects in the universe as a whole.

The second way in which gravitational lenses are useful for cosmology will comprise the main part of this thesis. This is a use that had been theoretically predicted by Refsdal in the 1960's, long before any gravitational lenses had been discovered

(Refsdal, 1964 ;Refsdal, 1966). He proposed using gravitational lenses to measure the distance to objects at cosmological distances, a task that has long proven difficult.

Gravitational lenses provide a unique opportunity to measure directly cosmological distances. This is done by relating the angular diameter distances among the objects in the lens to the difference in travel time among the various light paths to a multiply imaged background object. The travel time difference, known as the time delay, can be measured observationally if the brightness of the background object varies. The brightness variations among the images will be separated in time by their respective time delays. This will be discussed in greater detail in Chapter 2.

Suppose we want to calculate the time delay between two images, A and B, of the same background source. We start with the simple equation:

$$\Delta\tau = \tau_A - \tau_B. \tag{1.23}$$

Since τ_o is the same for each image, and using equation 1.22, we get the following expression:

$$\Delta\tau = (1+z_L)\frac{D_{OL}D_{OS}}{2cD_{LS}}\left[|\vec{\nabla}\,\psi(\vec{\theta_A})|^2 - |\vec{\nabla}\,\psi(\vec{\theta_B})|^2 - 2\,\psi(\vec{\theta_A}) + 2\,\psi(\vec{\theta_B})\right] \tag{1.24}$$

In this expression, we know z_L by observation. All angles in this expression are measured with respect to the lens center so if we can determine the center of the lensing mass in the image plane, we can determine $|\vec{\theta_A}|^2$ and $|\vec{\theta_B}|^2$. Also, through lens modeling, $\psi(\vec{\theta})$ can be determined for all $\vec{\theta}$. With these quantities known, we can combine them into a single known constant of proportionality, $G(z_L, \vec{\theta_A}, \vec{\theta_B}, \psi(\vec{\theta_A}), \psi(\vec{\theta_B}))$. Thus we have:

$$\frac{D_{OL}D_{OS}}{D_{LS}} = \frac{2c}{G}\Delta\tau \tag{1.25}$$

where G is determined by lens modeling and $\Delta\tau$ is measured observationally. In this way, a time delay and a lens model can determine a scaled distance in the lens system called the effective distance which we define as:

$$D_{eff} \equiv \frac{D_{OL}D_{OS}}{D_{LS}} \tag{1.26}$$

In order to use knowledge of D_{eff} to determine H_o, we must first relate angular diameter distance to redshift. This relation depends on which cosmological model we use, and in general we can write:

$$D(z_1, z_2) = \frac{c}{H_o} f(z_1, z_2) \tag{1.27}$$

where $D(z_1, z_2)$ is the angular diameter distance from an object of redshift z_1 to an object of redshift z_2, assuming both object lie along the same line of sight. The function $f(z_1, z_2)$ is independent of H_o. The functional form of f depends only on the cosmological parameters Ω_o and Λ_o. With a filled beam assumption[1] we have:

$$f(z_1, z_2) = \begin{cases} \dfrac{\sin(\chi_2 - \chi_1)}{(1+z_2)\sqrt{\Omega_o + \Lambda_o - 1}} & \text{for } \Omega_o + \Lambda_o > 1 \\ \dfrac{\chi_2 - \chi_1}{1+z_2} & \text{for } \Omega_o + \Lambda_o = 1 \\ \dfrac{\sinh(\chi_2 - \chi_1)}{(1+z_2)\sqrt{1 - \Omega_o - \Lambda_o}} & \text{for } \Omega_o + \Lambda_o < 1 \end{cases} \tag{1.28}$$

---

[1] The filled beam angular diameter distance assumes that the matter in the universe is uniformly distributed. Empty beam assumes that matter exists mainly in isolated clumps and so looking out through a small-angled cone there is likely to be no mass in the cone. Filled beam assumes that the cone is filled with matter of density Ω_o. Because of the lensing effect of matter, the different assumptions result in different angular diameter distances to objects of a given redshift. The difference is greatest for high redshifts and high Ω_o universes.

where

$$\chi_2 - \chi_1 = \begin{cases} \displaystyle\int_{z_1}^{z_2} \frac{\sqrt{|\Omega_o + \Lambda_o - 1|}\, dz}{\sqrt{\Omega_o(1+z)^3 + (1-\Omega_o-\Lambda_o)(1+z)^2 + \Lambda_o}} & \text{for } \Omega_o + \Lambda_o \neq 1 \\ \displaystyle\int_{z_1}^{z_2} \frac{dz}{\sqrt{\Omega_o(1+z)^3 + (1-\Omega_o)}} & \text{for } \Omega_o + \Lambda_o = 1 \end{cases} \tag{1.29}$$

(see Fukugita Futamase Kasai & Turner, 1992 and Dyer & Roeder 1972). Combining Equations 1.26 and 1.27, we get:

$$D_{eff} \equiv \frac{c}{H_o} \frac{f(0,z_L)\, f(0,z_S)}{f(z_L,z_S)} \tag{1.30}$$

where z_S is the redshift of the source and z_L is the redshift of the lensing object. In this equation, D_{eff} is determined by measuring the time delay and modeling the lens. For the given redshifts, z_L and z_S, the quantity $\frac{f(0,z_L)f(0,z_S)}{f(z_L,z_S)}$ depends only on the values of Ω_o and Λ_o in the model we choose. With most reasonable cosmological models, this quantity does not vary by more than a few percent. For example, if we take a typical case with $z_L = 0.5$ and $z_S = 1$, the difference between the angular diameter distance calculated for an $\Omega_o = 1$, $\Lambda_o = 0$ universe versus an $\Omega_o = 0.25$, $\Lambda_o = 0$ universe is only 6.6%. This error is small compared to the errors from lens modeling and time delay measurements. With all the other terms in the equation known, H_o is therefore determined.

1.3 Implications for Cosmology

In the previous section we showed that the method for determining H_o uses only knowledge of the effective distance and has a relatively weak dependence on the choice of cosmological model. By itself, H_o is the scale factor that tells us the distance to objects with low redshift, thus determining the geometry of the "nearby" universe with redshifts of about 0.2 or less, which contains most of the galaxies and galaxy clusters that are close enough to study in detail. Knowing the distances to these objects would immediately tell us their size, luminosity and age at which we see them. This is extremely useful for studies of galaxies, clusters of galaxies and estimates of the mass density of the universe.

However, some quantities that are bypassed in this method are themselves useful for cosmology. For example, the angular diameter distance to the lens, D_L, is a very useful quantity in its own right. With the method described in the previous section, D_L is never isolated. Only D_{eff} which is a ratio of D_L and other distances is determined (see Equation 1.26). As described by (Narayan, 1991), the way to isolate D_L from D_{eff} is to obtain, independently from lens modeling, information about the mass distribution of the lensing object. Such information usually consists of velocity dispersion measurements or cluster dynamics. That information is not available for the lenses discussed in this thesis at this time. However, measuring D_L to many lenses at a variety of redshifts would determine directly the relation between redshift and angular diameter distance out to high redshifts ($z > 0.5$) and thus represents the ultimate potential of studying gravitational lenses. As this thesis presents research concerning the first steps towards this goal, it is necessary to discuss the implications of this ultimate result as part of the motivation for this research.

Knowing the correlation between distance and redshift for a range of redshifts extending well beyond 0.5 will constrain much more than just the current expansion rate of the universe. This is because over the very long time its light has taken to reach us from these high redshift objects, the expansion rate of the universe may have changed. This can be determined in a plot of redshift versus distance. In Figure 1-4 the predicted redshift-distance curves are shown for several cosmological models. For a universe with a high mass density, the gravity will cause the expansion rate to slow down over the life of the universe, and possibly even to eventually start contracting. For a very low mass density, the expansion rate is expected to remain more or less constant. It is also conceivable, though not necessarily intuitive, that the expansion rate could increase. This is the case in models with a high value of the cosmological constant, Λ_o. Each cosmological model predicts a different history of the expansion rate of the universe from the big bang forward. Therefore, an empirical determination of the relationship between distance and redshift to very distant objects will help determine which cosmological model is correct.

The physical basis for a cosmological constant comes from the possibility that the vacuum energy density is not quite zero. Recent work with high redshift supernovae indicate that the expansion rate of the universe could in fact be increasing, which indicates a high value for Λ_o (Perlmutter et al. 1999). Knowing the energy density of the vacuum is fundamental to our understanding of physics. With experimental cosmology, it could actually be measured.

1.4 Radio Astronomy

1.4.1 Radio Waves

Visible light is the relatively small section of the entire electromagnetic spectrum, with wavelengths between about 400 nm and 750 nm, to which the human eye is sensitive (see Figure 1-5). Electromagnetic waves with longer or shorter wavelengths than visible light can also be used to gain valuable information about astronomical objects. Most of the data used in this thesis was obtained by observing the radio emission from gravitational lenses.

Radio emission has frequencies that range from a few tens of megahertz to many tens of gigahertz. This is much lower than that of visible light and is in the range where the oscillating electric fields can be measured directly and amplified with available electronics. For higher frequency radiation, such as visible light or X-rays, this is not currently possible and the light is detected instead by counting the number of electrical or chemical reactions the individual photons cause to occur in the detector (whether a charged coupled device, photographic film or even a retina).

1.4.2 Imaging the Radio Sky

Radio emission produces an oscillating electromagnetic field causing a varying voltage across an antenna which can be amplified by a transistor or other such device. This

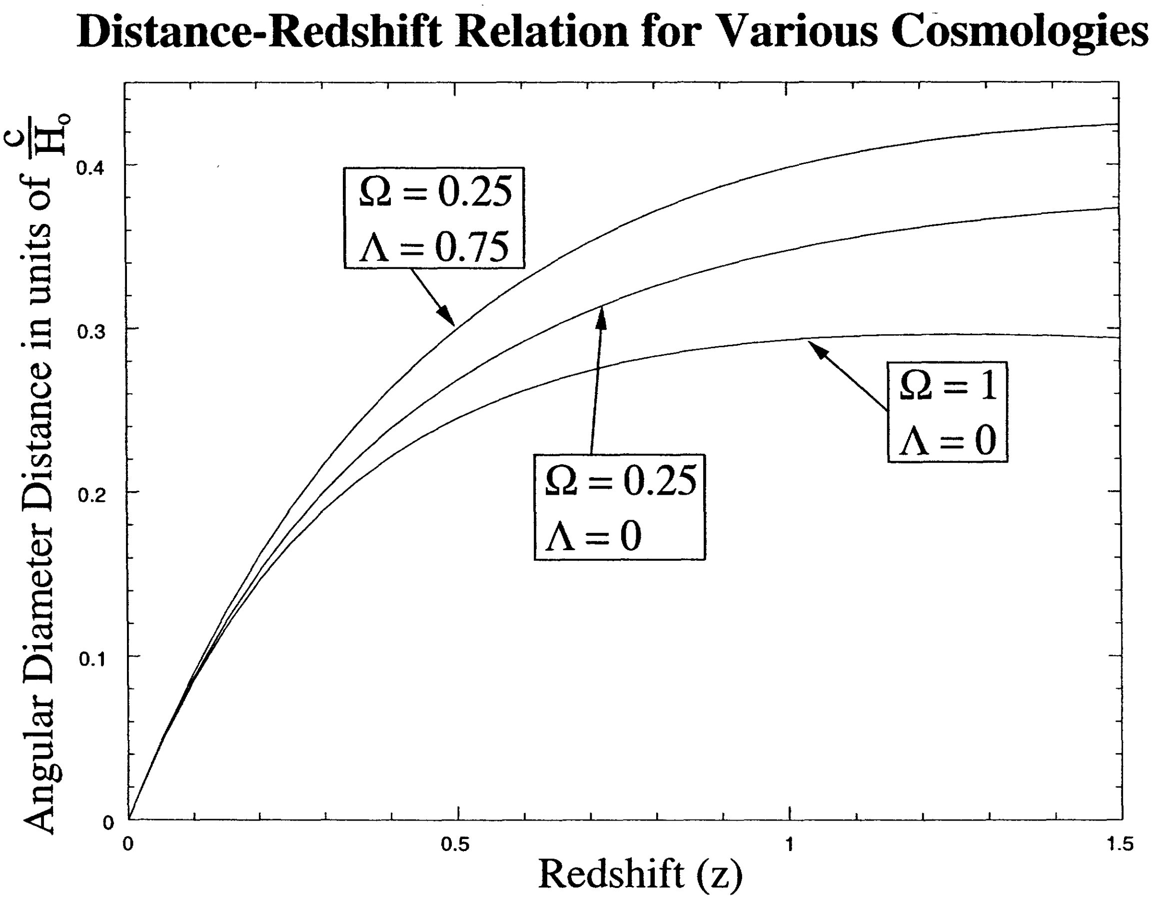

Figure 1-4: This diagram shows the relation between redshift and filled beam angular diameter distance (see Equations 1.28 and 1.29) for cosmologies containing various amounts of mass density (Ωo) and cosmological constant (Λ_o). The gravitational lens 0218+357 has a redshift of 0.685, so knowing its angular diameter distance would establish one point on the redshift-distance curve on the line shown. If the distance to many gravitational lenses at a variety of redshifts can be determined, it would help to not only to determine H_o, but also to distinguish among the curves shown here and therefore determine Ω_o and Λ_o as well.

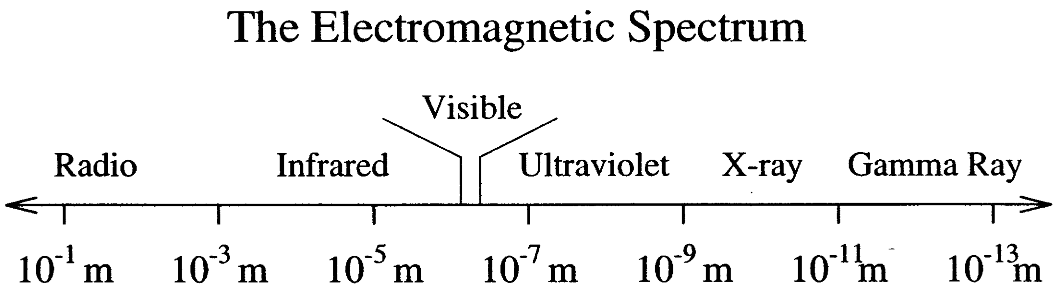

Figure 1-5: The full spectrum of electromagnetic radiation is shown here according to wavelength. Notice that visible light (400nm to 750nm) is a small part of this entire spectrum. Radio waves have wavelengths ranging from a few millimeters to over a meter and are not detectable by the human eye.

is how hand held radios work to use the radio emission from commercial broadcasters as the signal that is then converted into sound. The main difference between a radio telescope and a communication radio is that radio telescopes seek not only to detect the radio emission, but to determine precisely from where that emission is coming. In contrast, hand held radios have no need for directional information and simply accept radio signals from all directions. Another difference is that for radio astronomy, the signals received are far weaker than for artificial radio broadcasts. This means that the receiver design is extremely important.

One method of making a radio receiver sensitive to direction is to place the feed at the focal point of a reflecting paraboloidal dish. Radio emission that comes from the direction parallel to the axis of the paraboloid is maximally concentrated on the feed. In addition, the feed can be shielded from most of the emission that does not come from the reflective dish. The directional sensitivity is limited mainly by diffraction. A dish with diameter D will be mostly sensitive to a circular cone centered on the paraboloidal axis and with a diameter of θ in radians, where:

$$\theta = 1.22\frac{\lambda}{D} \tag{1.31}$$

This is called the primary beam of a radio dish, and the beam size, θ, is the image resolution achievable with this dish. For the same wavelength, λ, the beam size decreases as the dish diameter increases.

Suppose one wants to observe an object with 0.25" resolution at a wavelength of 3.6 cm, or 8.4 GHz. According to Equation 1.31, the dish size needed for such resolution would be 36 km! This is of course impractical. Yet, with a more "practical" size dish of $D = 25$ m, the primary beam would have a diameter of 360", which is about one fifth as large as the full moon. This would make imaging of most sources impossible.

The solution to this problem is to take advantage of the ability of radio receivers to measure the amplitude and phase of incoming radiation. That allows for the technique of interferometry, which involves combining the signals from radio telescopes that are far apart. For example, the Very Large Array (VLA) telescope in Socorro, New Mexico, uses 27 radio dishes, each 25 m in diameter, which are placed in a three-arm array in which the maximum separation is 36 km. The VLA *is* capable of achieving 0.25" resolution at a wavelength of 3.6 cm with interferometry, just as if it were a single 36 km-wide dish. The Very Large Baseline Array (VLBA) consists of ten 25 m-diameter radio dishes placed at various locations throughout the North American continent. The VLBA is capable of resolutions of less than 0.001", which is the angular size of a golf ball in New York as seen from Los Angeles.

To illustrate how interferometry works, first consider the case of a single pair of radio telescopes. Radio emission from a particular direction in the sky will arrive at one telescope at a slightly different time than at the other telescope depending on the relative positions of the two radio dishes. Both telescopes will measure the same signal, but with a different phase depending on the light path length difference. This path length difference between the two telescopes will depend very strongly on the angle from where the emission is coming (see Figure 1-6). As the angle is gradually increased, the interference goes from constructive to destructive and back to constructive, in what is a striped pattern that is perpendicular to the line from one telescope to the other. The "striped" pattern is actually a sinusoid, and so the two antennas together measure not the total radio emission within the primary beam, but that emission multiplied by a sine wave. The angle and frequency of the sine wave depends on the angle and spacing of the antenna pair. So essentially each antenna pair measures one two-dimensional Fourier component of the image in the sky. With the

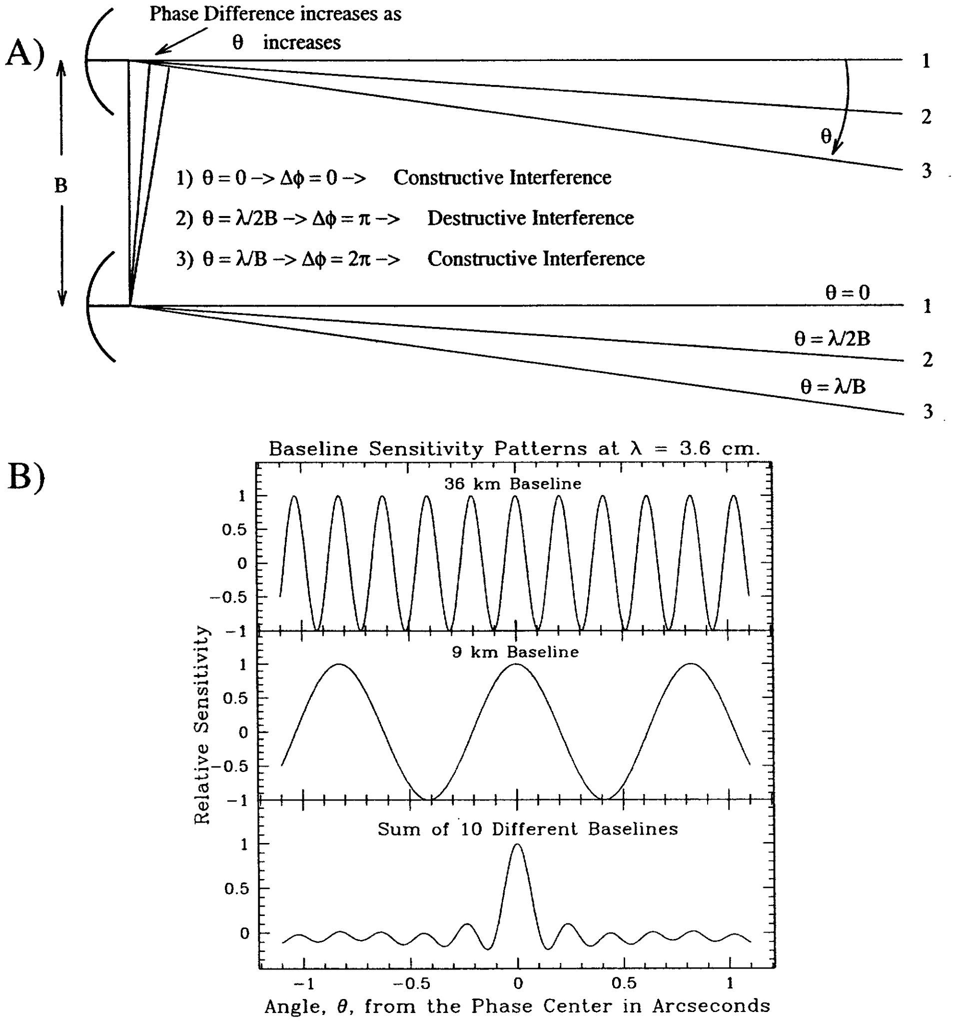

Figure 1-6: A). A pair of telescopes aimed in the same direction will see an interference pattern that varies with angle in the sky. The interference pattern is a sinusoidal striped pattern across the entire primary beam. The longer the baseline, the narrower the stripes become. That is why long baselines are necessary to obtain fine resolution in an image. B) As shown in part A, the combined sensitivity of a single pair of antennas will form a sinusoidal striped pattern in the sky. The stripes are thinner for longer baselines. This diagram shows the sensitivity patterns for various baselines at a wavelength of λ = 3.6 cm. The top pattern is for a 36 km baseline, while the second pattern is for a 9 km baseline. The combination of the sensitivity patterns of 10 different baselines is shown on the bottom. Notice how most of the sensitivity is contained in a small region near the phase center. This is called the synthesized beam, and for an array, this is analogous to the primary beam of a single antenna. For the VLA, the synthesized beam is over 1000 times smaller than the primary beam.

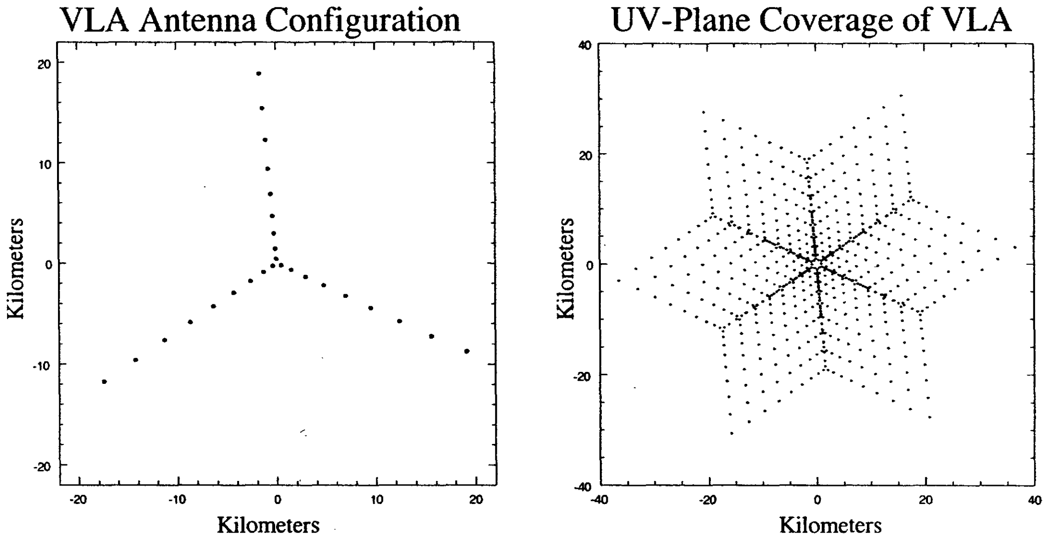

Figure 1-7: The layout of the 27 VLA antennas is shown in the left plot. The right plot consists of all possible vectors from one antenna to another. This is referred to as the instantaneous *uv*-coverage of the array.

VLA, there are 27 antennas and therefore 351 antenna pairs. Each pair of antennas can be represented by a point defined as the vector from one antenna to the other projected on a plane perpendicular to the line of sight of observing. Such a vector is called the baseline. Figure 1-7 shows the antenna configuration for the VLA along with all the baselines such a configuration produces. The plane in which baselines are plotted is called the *uv* plane because the coordinate axes are commonly labeled as u and v. A visibility is a measurement taken at one baseline, or one point in the *uv* plane. The *uv* plane consists of the two dimensional Fourier transform of the actual image in the sky. With interferometric arrays, the direct measurements are of data points in the *uv* plane, which must then be Fourier transformed back to obtain an image.

However, the fact that the entire *uv* plane is not sampled will result in errors in its Fourier transform and hence the final image. To determine how incomplete *uv*-coverage will effect the final image, it is useful to first consider the response of a given array to a point source of radio emission. If the point source falls in the primary beam of the antennas in the array, all the antennas will receive the following signal

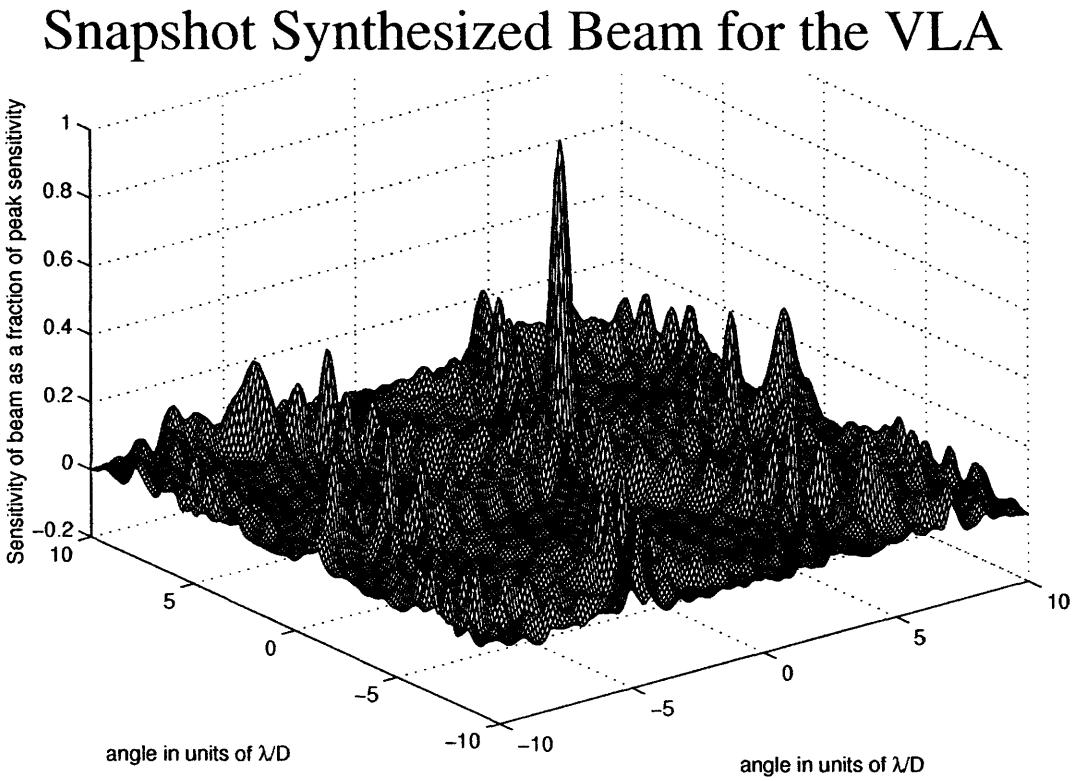

Figure 1-8: The synthesized beam for the VLA snapshot *uv* coverage. The image originally produced by such *uv* coverage consists of the brightness distribution on the sky convolved with this synthesized beam pattern.

$S(t)$ with complex value:

$$S(t) = F\,e^{i\,(\nu\,t + \phi_{geometry})}. \tag{1.32}$$

This signal is simply the sinusoidally varying electromagnetic field of frequency ν and strength F that is received from the point source. Because of the different locations of each antenna, the signal will not arrive at all antennas simultaneously, so there will be a phase offset, $\phi_{geometry}$, unique to each antenna. This can be adjusted for by adding an electronic delay to the signal received at the central correlator that exactly cancels the phase offset at each antenna location. Now, the point source is said to be at the phase center of the array, and all the antennas will receive the same signal:

$$S(t) = F\,e^{i\,(\nu\,t)}. \tag{1.33}$$

The complex visibility between two given antennas, i and j, is:

$$V_{ij} = S_i(t) * S_j^*(t) = |F|^2 \tag{1.34}$$

where S^* denotes the complex conjugate of S. So for a point source at the phase center, all visibilities from all baselines are equal. The response of the array to a point source can be determined by giving each sampling in the *uv*-plane the same value (usually 1 for convenience) and then inverse Fourier transforming this *uv* data. This is called the synthesized beam for a particular *uv* coverage, and is analogous to the point spread function in optical astronomy. In Figure 1-8 the synthesized beam is shown for the instantaneous *uv* coverage of the VLA as shown in Figure 1-7. This beam pattern consists of a central peak where the array is most sensitive, the width of which will determine the resolution of the image. There are other, smaller peaks and valleys in the area surrounding the main peak which are called sidelobes. The more complete the *uv* coverage is, the lower the sidelobes will be. The lower the sidelobes, the better the initial image fidelity will be. The image originally produced by a given *uv* coverage, called a dirty image, consists of the brightness distribution on the sky convolved with the synthesized beam pattern of the given *uv* coverage. The degrading of the image caused by the convolution of the true sky brightness with the synthesized beam pattern is the ultimate effect of incomplete *uv* coverage.

Knowing the beam pattern it is desirable to deconvolve it from the dirty image to recover the undistorted sky brightness distribution. There is no analytical way to do this, however some numerical algorithms seem to perform quite well. The most widely used of such algorithms is called "CLEAN". CLEAN is an iterative procedure which finds the brightest point in the dirty image and subtracts a fraction of the synthesized beam pattern from the dirty image. It then goes on to the brightest point in the resulting image and repeats the process. This can go on for thousands of iterations until virtually all the flux in the image is subtracted. Then, at the points where the beam pattern was subtracted, it is replaced by a two dimensional Gaussian of the same dimensions as the central peak of the synthesized beam. The idea is to replace the flux of the image but without the sidelobes from the beam pattern. The result is called a CLEANed map and is generally a huge improvement over the dirty map. Virtually all images produced by interferometry need to be CLEANed in order to be useful. Over time there have been improvements made to both the efficiency and stability of the CLEAN algorithm (see Högbom (1974), Schwarz (1978), Clark (1980) and Cornwell (1983)). However, the core idea of CLEAN remains the same. It is likely that in the near future, new radio telescope arrays will be built with hundreds or even thousand of elements, making the *uv*-coverage so complete that CLEANing will be unnecessary.

1.4.3 Sources of Extragalactic Radio Emission

In order to get a better feel for how radio astronomy can be useful in experimental cosmology it is useful to discuss how the extragalactic universe appears at radio wavelengths. As at optical wavelengths, the universe is dominated by galaxies. However, not all galaxies are luminous radio sources. The few that are, usually have what is called an Active Galactic Nucleus (AGN) at their core. The nature of AGN is still a matter of debate, but it is likely that they consist of super-massive black holes which are still in the process of forming by accreting matter from their surroundings. As the matter falls into the deep gravitational potential well of the black hole, it gains kinetic energy in the form of heat. The falling matter spirals into the black hole forming a very hot and luminous accretion disk. The accretion disk can easily become far more luminous than all the rest of the hundreds of billions of stars in the host galaxy combined. In the optical part of the spectrum, AGN are the most luminous steady state light sources known in the universe. Originally mistaken for stars, these objects were named QSO's (Quasi-Stellar-Objects) or quasars. Their existence is fortunate for astronomers, because it allows us to see objects that are at the very edges of the observable universe.

Virtually all radio bright galaxies are associated with an AGN. Unlike at optical wavelengths, the radio image of an AGN often includes not only a bright central core, but also bipolar jets and lobes (see Figure 1-9). These jets and lobes shine in the radio

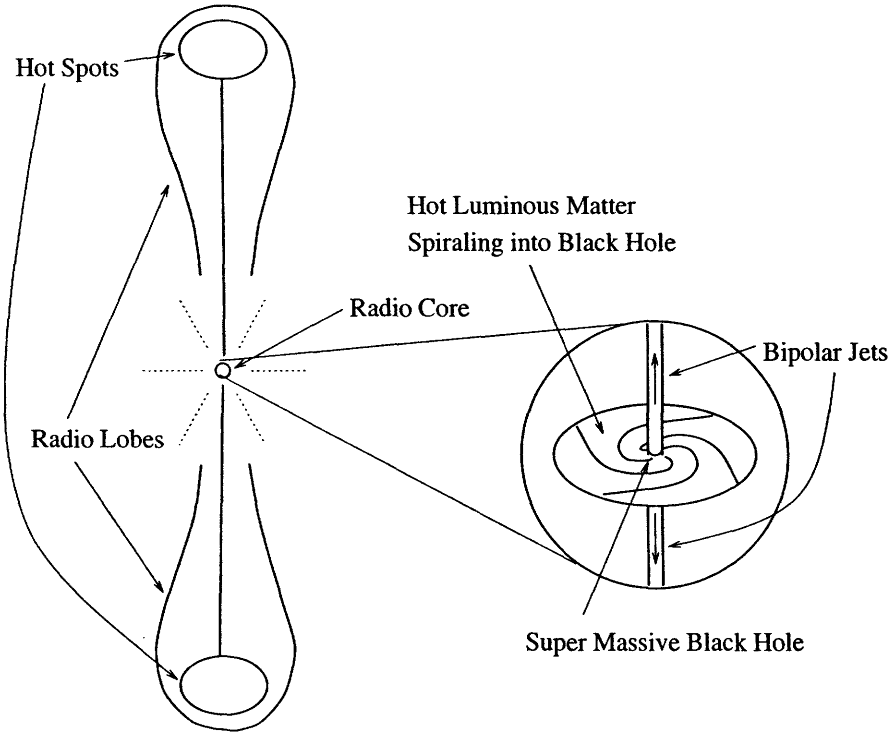

Figure 1-9: An artists rendition of a generic radio galaxy. The main features are the central radio core (AGN), the bipolar jets and the lobes. A "Hot spot" refers to the bright region within a lobes which is assumed to be where the fast moving jets meet the intergalactic medium forming a hot, luminous shock front. A magnified view of the radio core is shown to demonstrate a possible mechanism for the formation of the AGN. No such magnified view has actually been directly observed.

because they contain relativistic charged particles, which in the presence of magnetic fields emit synchrotron radiation. The lobes are clearly fed by the jets, but what causes the jets is not well understood. Some fraction of the very energetic particles near the center of the accretion disk must somehow be ejected at high speeds along the polar axes. Though no completely satisfactory explanation yet exists, the existence of these lobes is also fortunate for astronomers. This is because, among other things, the extended emission in the lobes provides more structure to the background objects in gravitational lenses. With more structure being multiply imaged, it becomes much easier to model such gravitational lenses, as will become apparent later in this thesis.

1.4.4 Background on the Gravitational Lens 0218+357

The majority of the scientific information in this thesis comes from observations of the gravitational lens 0218+357. Therefore, some background information and history on this lens will now be discussed.

The radio source 0218+357 was first proposed as a gravitational lens by Patnaik, et al., 1993 and O'Dea et al., 1992. It consists of two images of a background BL Lac type AGN, including a radio Einstein ring and a more distant radio lobe that is not multiply imaged (see Figure 1-10). The radio ring has an unusually small diameter, only $0.35''$. The small ring, the detection of absorption lines attributed to neutral hydrogen (Carilli, Rupen & Yanny, 1993) and various molecules (Wiklind & Combes, 1995), and the large rotation measure observed in linear polarization suggest that the lensing object is a gas-rich spiral galaxy. The images of the radio core reveal a flat-spectrum component that has been imaged on VLBI scales (Patnaik, Porcas & Browne, 1995). The lens redshift, based on optical (Browne et al., 1993) and radio absorption lines, is 0.685; the source redshift is 0.96 (Lawrence 1996).

In this lens system, the two bright point sources are in fact two images of the same AGN. The double image occurs because the AGN is offset slightly from the direction of the center of the lensing mass (as in Figure 1-3 part C). The separation between the two AGN images is only 0.33", making this the smallest gravitational lens yet known. From the AGN, there is a single radio jet and lobe that extends away from the AGN by about 1". Unlike the AGN core, the jet and lobe are large enough to produce extended emission. Presumably a part of the jet falls directly behind the center of the lensing mass, and its image is therefore expanded into a full Einstein ring (as in Figure 1-3 part B). The end of the jet and the lobe are too far from the lensing center to be multiply imaged, but most likely the single image we see is nevertheless distorted by the lens.

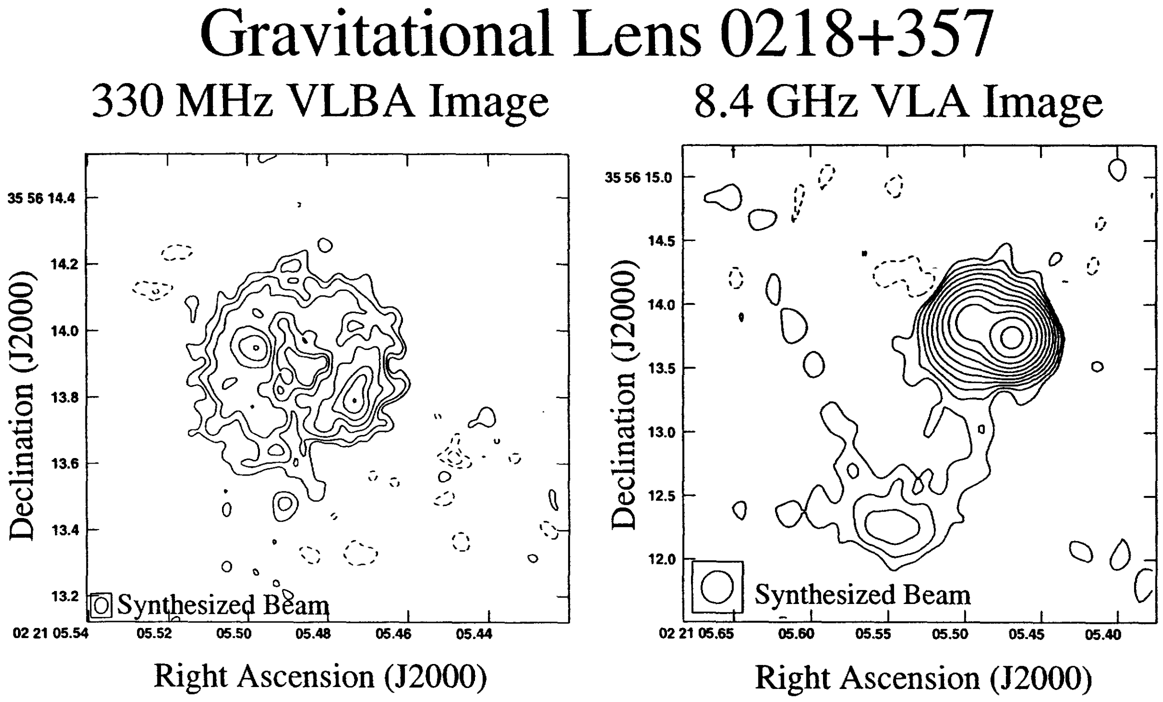

Peak Flux Density = 65.5 mJy/beam
Contour Levels = 1 mJy * (-4, -2, -1, 1, 2, 4, 8, 16, 32, 64)

Peak Flux Density = 836 mJy/beam
Contour Levels = 0.6 mJy * (-4, -2, -1, 1, 2, 4, 8, 16, 32, 64, 128, 256, 1024, 2048)

Figure 1-10: Two images of gravitational lens 0218+357. The left image was taken at 330 MHz with the VLBA and has a resolution of 48 by 38 mas. The Einstein ring appears as a diffuse annulus. The two images of the radio core are seen as well. The right image was taken at 8.4 GHz with the VLA and at a resolution of about 220 mas. Here the resolution is too low to easily distinguish the two AGN images, A and B, much less the Einstein ring that surrounds them. However, the jet that extends to more than 1″ to the south is clearly visible. Notice that the two images are at different scales.

1.5 Thesis Summary

This thesis will concentrate on the use of the gravitational lens 0218+357 to measure the effective angular diameter distance to the lensing galaxy in that system which has a redshift of 0.685. That provides a direct estimate of H_o and is therefore one step in the process of measuring the geometry of the universe.

First I will describe our lens monitoring project, in which we made periodic observations of eight different gravitational lenses with the aim of measuring time delays based on time shifted variations in multiply imaged components. We were able to measure a time delay in the lens 0218+357 to the highest precision, so I will concentrate on the data from that lens and then describe how we determined the time delay from that data and our statistical analysis that set our confidence limits. Then, I will describe the modeling of this system which relies partly on additional observations that we made. With the time delay and model, H_o is determined. I will then discuss what this result implies for cosmology as well as future research in this area.

REFERENCES

Browne, I. W. A., Patnaik, A. R., Walsh, D. & Wilkinson, P. N. 1993, MNRAS, 263, L32

Carilli, C. L., Rupen, M. P. & Yanny, B. 1993, ApJ, 412, L59

Clark, B. G. 1980, A&A, 89, 377

Cornwell, T. J. 1983, A&A, 121, 281

Dyer, C. C. & Roeder, R. C. 1972, ApJ, 174, L115

Fukugita, M., Futamase, T., Kasai, M. & Turner, E. L. 1992, ApJ, 393, 3

Högbom, J. A. 1974, A&AS, 15, 417

Lawrence, C. R. 1996, IAU Symp. 173: Astrophysical Applications of Gravitational Lensing, 173, 299

Narayan, R. 1991, ApJ, 378, L5

O'Dea, C. P., Baum, S. A., Stanghellini, C. , Dey, A. , Van Breugel, W. , Deustua, S. & Smith, E. P. 1992, AJ, 104, 1320

Patnaik, A. R., Browne, I. W. A., King, L. J., Muxlow, T. W. B., Walsh, D. & Wilkinson, P. N. 1993, MNRAS, 261, 435

Patnaik, A. R., Porcas, R. W. & Browne, I. W. A. 1995, MNRAS, 274, L5

Perlmutter, S., et al. 1999, ApJ, 517, 565

Refsdal, S. 1964, MNRAS, 128, 307

Refsdal, S. 1966, MNRAS, 132, 101

Schwarz, U. J. 1978, A&A, 65, 345

Walsh, D., Carswell, R. F. & Weymann, R. J. 1979, Nature, 279, 381

Wiklind, T. & Combes, F. 1995, A&A, 299, 382

Chapter 2

Gravitational Lens Monitoring

2.1 How to measure a time delay?

In order to measure the distance to a particular gravitational lens by the method described in Chapter 1, one first needs to measure at least one time delay among the multiply imaged components. This is done by taking a series of measurements over time of the brightness of each component. Plots can be made for each component of its flux as a function of time, called light curves. If the flux varies, it will vary at different times in the different components due to the time delay between them. Therefore, comparing the light curves can reveal the time delay between those two components.

Since this can be done only if the multiply imaged light source has a variable brightness, it is useful to have an idea beforehand which components in which lenses are likely to vary. One general rule is that a light source can change its brightness no faster than the time it takes for light to travel across that source. In other words, smaller sources can vary faster than large sources. If we are hoping for variations on a time scale of about a week, our light source must be smaller than the distance light can travel in one week. If we assume a typical distance to a cosmologically distant object, say 4 billion light years then a one-light-week sized object will have an angular size of roughly 5×10^{-12} radians, or about one millionth of an arcsecond. This is much smaller than the resolution of any current telescopes, so any source that is large enough to be resolved can be ruled out as a variable source. That leaves only the radio cores as possible variable objects (see figure 1-9). Most unlensed radio cores in radio galaxies have been observed to vary over timescales ranging from days to months, so it is reasonable to expect that the multiple images of a lensed radio core will vary as well.

2.2 Previous Time Delay Measurements

This method was first applied to the gravitational lens 0957+561, with time delays reported by Florentin-Nielsen, 1984; Vanderriest et al., 1989; Lehar et al., 1992 and Press, Rybicki & Hewitt, 1992(a&b) among others. (For a comprehensive review of time delay measurements in 0967+561 see Haarsma et al., 1997.) The results were conflicting and somewhat controversial, and have only recently been resolved (Kundic, et al. (1997); Haarsma et al., 1999). These measurements, particularly those of Kundic et al., determine the delay with 1% accuracy, which makes this by far the best determined time delay. However, uncertainties in the lens model at present limit the accuracy of a distance determination in the 0957+561 system (Falco, Gorenstein & Shapiro, 1991; Grogin & Narayan, 1996(a&b); Bernstein et al., 1997). Recently, time delays have been reported in other lens systems, including PG 1115+080 (Schechter, et al. (1997)), B0218+357 (Biggs, et al. (1999)), PKS 1830-211 (Lovell et al., 1998), HE 1104-1805 (Wisotzki Wucknitz Lopez & Sorensen, 1998) and B1608+656 (Fassnacht et al., 1999). In many of these systems, additional data will be needed to reduce the uncertainties in the time delay. And for most of these systems, the lens modeling currently limits the determination of angular diameter distance. In order to refine significantly our investigations in cosmography, it will probably be necessary to consider measurements of many lens systems as well as to improve individual lens models. With this goal in mind a number of lens monitoring programs are under way. In this chapter, we will present the VLA monitoring of five lenses, of which two have so far produced time delay measurements.

2.3 The Data

All the lens monitoring data presented in this thesis comes from the MIT-VLA Lens Monitoring Survey (October, 1996 to May 1997), in which eight gravitational lenses were monitored for various lengths of time with the VLA. In this chapter, the light curves for five of those lenses will be presented along with discussion of the data reduction and image processing methods used to achieve accurate flux measurements.

2.3.1 Data Calibration

The VLA produces raw data in the form of visibilities. Each visibility corresponds to the combined data from a single pair of antennas and is represented by the amplitude and phase of the correlation of the signals measured by each antenna. The amplitude measures the product of the signal strengths received by both antennas, and the phase is the phase difference of the light between the two points in space that the antennas occupy.

Each antenna receiver directly measures a voltage caused by the electric field of the radio emission. We need to relate this measured voltage to the electric field strength of the incoming light. Specifically, we would like to know the gain of the system, G, which we use as the coefficient of proportionality between these two quantities. In this case, we define

$$|\vec{E}| = \frac{V_m}{G} \tag{2.1}$$

where $|\vec{E}|$ is the electric field strength, and V_m is the measured voltage produced by that electric field. The gain depends on many factors including the antenna collecting area, the receiver electronics, the gain of the amplifier and the integrated opacity of the atmosphere along the line of sight. Since all but the last two of these factors are known beforehand, we can make a reasonable guess of the overall antenna gain based on knowledge of the antenna itself. Because of atmospheric effects, and the amplifier gain which can vary, the overall gain will vary. In order to produce the best possible images from the visibility data, we need to calibrate the gains of each antenna of the array by observing calibrator sources which have known characteristics. The best way to determine G is to observe a source with known $|\vec{E}|$ and take note of the value of V_m that the antenna returns.

The largest effect of the atmosphere is not to change $|\vec{E}|$ from its natural value, but to change the phase of the incoming light. This is because the index of refraction of the atmosphere for radio emission varies with position and time. In an array like the VLA, the antennas are kilometers apart, and therefore each antenna will have a unique atmosphere-induced phase offset. (Electronics also contribute to this phase offset, but such variations are expected to be on much longer time scales.) The total phase offset can be corrected by giving the gain term G a phase as well as magnitude which will correct this phase offset. In this sense, G is a complex number with amplitude defined by Equation 2.1 and a phase that corresponds to the atmosphere-induced phase offset of that antenna. The best way to determine this phase offset is again by observing a calibrator source, which we call the phase calibrator. The phase calibrator source should be close enough to being a point source that even the longest baselines can't resolve it. In this case, if the source is placed at the phase center of the array, all visibilities should have the same magnitude and zero phase. Since there are 351 baselines in the 27-element VLA, that yields 351 equations for 27 unknown antenna gains. Therefore, this is an overdetermined system and so the complex gains can be calibrated to a high degree of accuracy.

It so happens that virtually all point-like sources have variable fluxes. Therefore, in addition to a phase calibrator, we need to observe a flux calibrator which should be a source of large and constant flux. The flux calibrator need not be a perfect point source like the phase calibrator. The visibilities of the phase calibrator can be compared to those of the flux calibrator to determine the flux of the phase calibrator at the time of observation.

Since it is uncalibrated, we observed (in addition to the lenses of interest) a flux calibrator source, either 3C286 or 3C48, which both have constant and published flux values, as well as point source calibrators which are unresolved sources used to set the complex gain of each antenna. The data reduction was done with NRAO's Astronomical Imaging Processing System (AIPS). We used AIPS to first calibrate the

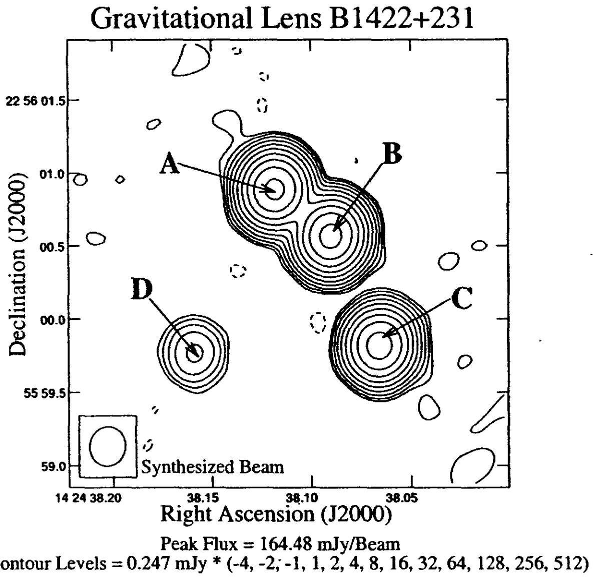

Figure 2-1: VLA image of Gravitational Lens 1422+231.

lens visibilities according to the calibrator visibilities. The calibration process was the same for each lens. Once the data were calibrated, the data reduction differed somewhat for each lens depending on its morphology.

2.3.2 Gravitational Lens 1422+231

The gravitational lens 1422+231 was the first lens for which light curves were produced. It was discovered by Patnaik et al. in 1992, and consists simply of one radio core which is quadruply imaged by the lensing mass (see Figure 1-3, case D). The four images are labeled A, B, C and D as shown in Figure 2-1. The four radio cores are unresolved to the VLA and there is no extended emission. Time delays have been predicted, with the delays among A, B, and C expected to be much less than a day, and the delay from A, B and C to D expected to be $15h^{-1}$ (Kundic et al., 1997). The h here is defined as:

$$h \equiv \frac{H_o}{100\ km/s/Mpc}. \tag{2.2}$$

Therefore, our lens monitoring will attempt to measure a time delay between the D image and the other images. The time delays among the A, B and C images is too small to measure with our sampling rate.

The monitoring data for this lens consisted of 45 separate observations taken with the VLA between October 9, 1996 and May 2, 1997. The VLA was in both the A and B-array configurations during this period. The observations were at 8 GHz with a 100 MHz bandwidth. Observation times varied but averaged about 15 minutes on source. The flux density scale was set by observing the flux calibrator source 3C286. The phase calibrator 1407+284 was used to calibrate the complex antenna gains.

Each observation can be completely described by 10 parameters. Six parameters specify the relative positions of three of the four point sources relative to the first (absolute positional information is irrelevant to our measurements). The other four parameters specify the flux of each of the four images. Previous VLBA observations of this lens have already determined the six positional parameters to milliarcsecond accuracy. These data were shared with us courtesy of Cathy Trotter. We therefore had a model with only four free parameters to describe each observation. With such a simple model, it was not necessary to create images with the UV data, but rather we fit our four parameter model directly to the UV data with the AIPS task UVFIT. We identify the flux of each of the four images with the corresponding best fit parameter produced by UVFIT.

At this point we must consider the possibility that differing UV coverage of each observation might affect our ability to make flux measurements of consistent accuracy over the course of the light curves. Not only does the UV coverage change because of the different LST of each observation, but about halfway through our monitoring of 1422+231, the VLA went from A-array configuration to B-array configuration. To correct for these variations in UV coverage, we create a set of synthetic data sets in which the visibilities of the real data sets are replaced by those of a static source model. The synthetic data sets are then put through the exact same data reduction procedure as the real data sets to produce a synthetic light curve. Since the source model is static, any variability in the light curves is due only to the differing UV coverage. By isolating this effect we were able to remove it from the real light curves by dividing by the simulated flux measurements.

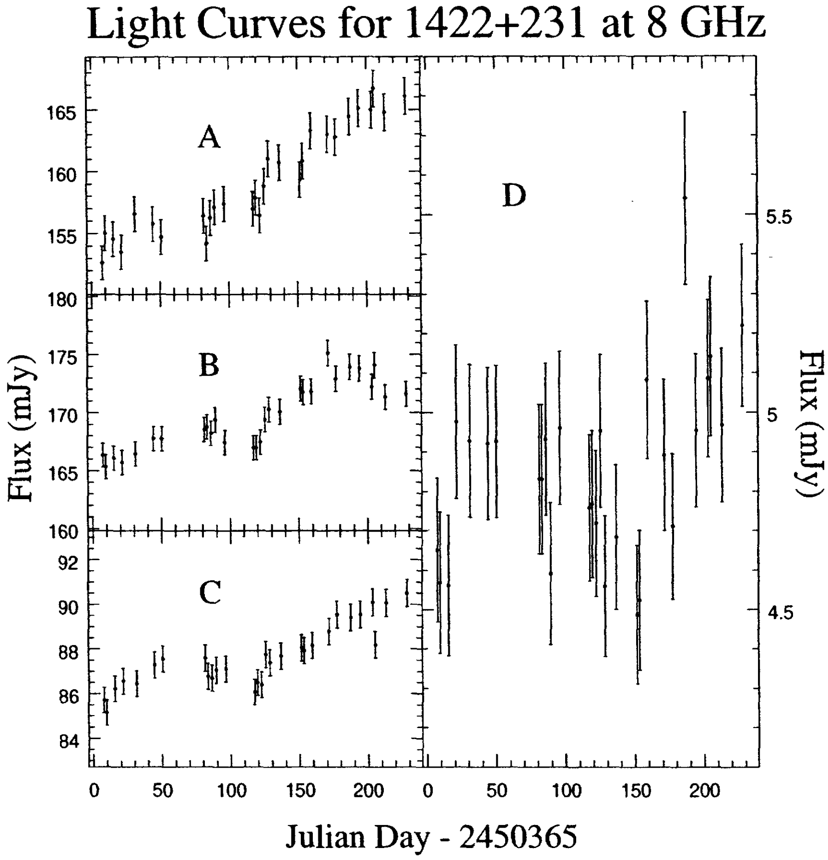

Figure 2-2: Light curves for 1422+231.

Of the 45 observations, some were not included in the final light curves because of bad weather or other effects. Data points in which the flux calibration errors or the χ^2 value of the model fitting were much higher than normal were removed. The resulting light curves have 29 data points and are shown in Figure 2-2. The error bars were determined by calculating the average scatter of nearby points in each light curve as will be discussed in more detail in the next chapter. The source object in this lens system clearly shows variability as can be seen in the A, B and C light curves. The error bars in the D light curve are fractionally much larger, mainly because it is much fainter than the other source images. As a result, the D light curve does not show any features at a high enough signal to noise ratio necessary to measure a time delay by comparing it to the other light curves. Therefore we cannot make a time delay estimate from this data.

Since the time delays among the A, B and C light curves are too small to measure,

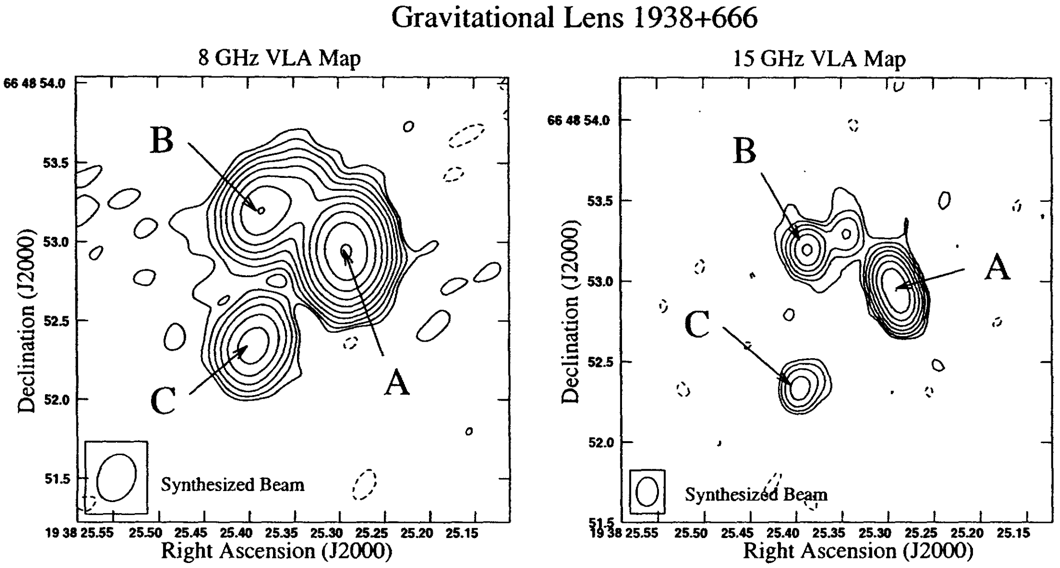

Peak Flux = 133.7 mJy
Contour Levels = 0.25 mJy * (-4, -2, -1, 1, 2, 4, 8, 16, 32, 64, 128, 256, 512, 1024)

Peak Flux = 64.2 mJy
Contour Levels = 0.5 mJy * (-4, -2, -1, 1, 2, 4, 8, 16, 32, 64, 128, 256, 512, 1024)

Figure 2-3: VLA images of 1938+666.

these light curves should be identical in shape. It is clear that this is not the case. Possible reasons for this result will be discussed in the next chapter.

2.3.3 Gravitational Lens 1938+666

Gravitational Lens 1938+666 was also monitored over roughly the same time period as 1422+231. This object was first identified as a lens by King et al., 1997. It has a cat's paw type morphology, similar to 1422+231, however many of the "points" are resolved. The three brightest components, labeled A, B and C, (Figure 2-3) are all resolved, and component A actually appears to be an arc of some sort. Components B and C also are resolved, indicating that if any point sources are present, they are surrounded by extended emission. Of course resolved sources cannot vary, so we produce light curves of these three components in the hopes that they are combinations of extended emission on top of points sources which may in fact vary. We hope to see these variations as variations in the combined flux of each component. Our observations are at both 8 GHz and 15 GHz. No time delay has yet been predicted for this system.

Since the morphology of this lens is much more complicated than that of 1422+231, we are unable to use UVFIT to fit for the fluxes. Therefore it is necessary to produce images from each observation. We use the AIPS task IMAGR to create images from the UV data. First IMAGR simply does a two-dimensional Fourier transform to change the UV data into an image. This image is initially of poor quality because it is convolved with the synthesized beam, which has significant sidelobes. There is no analytic way to deconvolve such a beam, but it can instead be done numerically with a method called "CLEAN" (Hogbom, 1983, Clark (1980)). CLEAN is an iterative algorithm which on each step subtracts a fraction of the beam from the point of highest flux level. This process is repeated until it there is no flux in the map higher than some previously specified level. Then, at each point where the beam pattern was subtracted, it is replaced with a two-dimensional Gaussian that best fits the center of the synthesized beam. Thus all the flux is replaced, but without the sidelobes, creating a cleaned image. It should be noted that this method is not mathematically proven, but is widely used since it performs quite well based on empirical tests.

Since the locations on the map where flux was subtracted are recorded during the "cleaning" process, we automatically produce a point-source model of the source. If we suspect that the initial calibration of the UV data could be improved, as is usually the case, we can then go back to the UV data and use AIPS to readjust the complex antenna gains so as to best fit the model we have produced. This is called self calibration, and a few such iterations can greatly reduce the noise in an image. Like the "CLEAN" algorithm, self calibration is not mathematically proven, yet appears to work quite well empirically. For our data, including that in Figure 2-3, we perform three iterations of self calibration, allowing only the phases of the gains to be adjusted. This is because the gain amplitudes are better determined in the initial calibration, and in the interests of being as conservative as possible, we don't want to have too many free parameters in the self calibration.

Once the final maps had been produced, the measurement of the fluxes of A, B and C were done by measuring the peak flux of each of the "blobs" associated with each component. As for the 1422+231 data, simulated data sets were created to remove

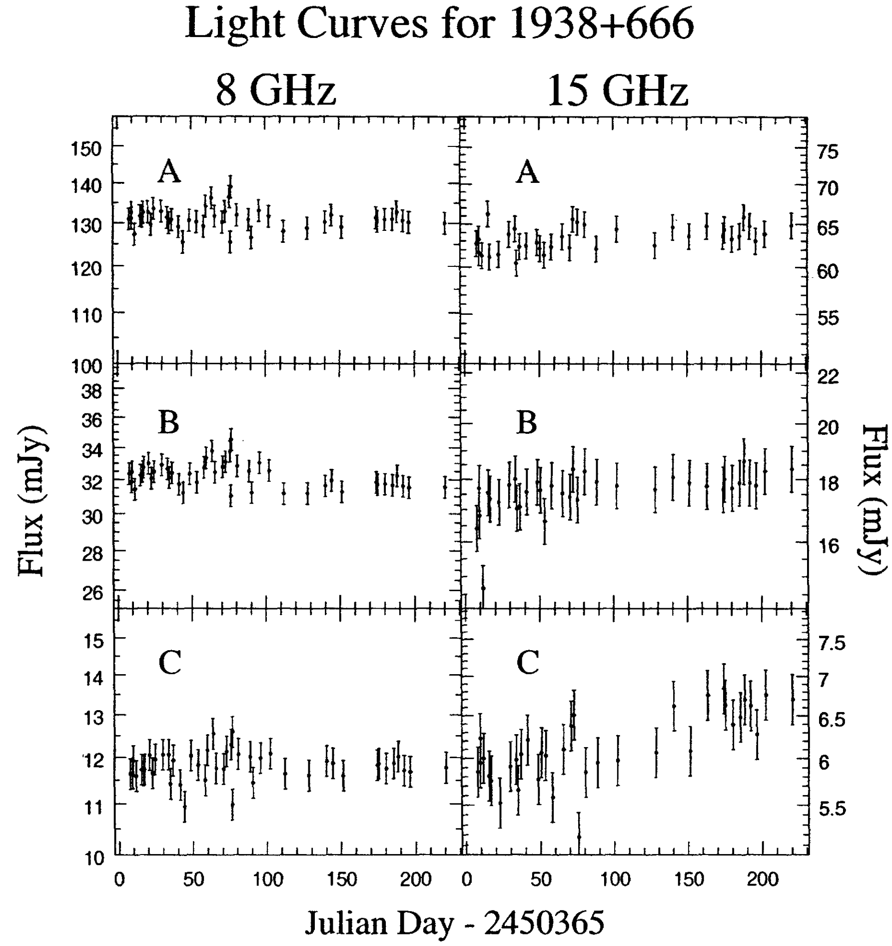

Figure 2-4: Light curves for 1938+666.

the effects of varying UV coverage for each observation. Again, observations for which the weather was bad, or the flux calibration was unsuccessful, were removed.

The resulting light curves are shown in Figure 2-4. Unfortunately there is no variation in any component that is greater than the noise. Therefore, for this lens no time delay measurement is possible based on this data.

2.3.4 Gravitational Lens 1131+0456

Another lens we monitored was 1131+0456, which includes the first Einstein ring to be discovered (Hewitt et al., 1988). It consists not only of the ring, but also a doubly imaged radio core, labeled A and B (see Figure 2-5). Presumably, the source object consists of one bright radio core which falls slightly off-center of the lensing mass and

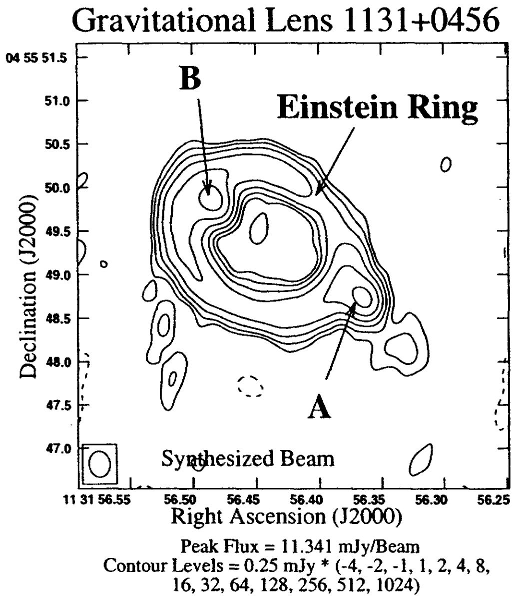

Figure 2-5: VLA map of 1131+0456 at 8 GHz.

so is lensed into two images (see Figure 1-3, case C). In addition to the radio core, there is some extended emission, probably a jet, that happens to fall exactly behind the center of the lensing object and is transformed into a large ring as seen from Earth (see Figure 1-3, case B). We hope to measure a time delay between the point-like components A and B. The predicted delay is about $58h^{-1}$ days (Chen, Kochanek & Hewitt (1995)).

Gravitational lens 1131+0456 was too complicated a source to fit a simple model to the UV data, so images were produced in the same manner as for 1938+666. The observations were calibrated with AIPS and then phase-only self calibrated three times. The flux values of A and B were taken to be the peak flux value of each point source. This likely included some flux from the ring, however, the ring is a constant source and shouldn't add any variability to the light curves. Of course this is only true because, as for the previous lenses, we made simulated light curves to remove the effects of varying UV coverage.

The resulting light curves are shown in Figure 2-6. Unfortunately there is again no variation in either component that is greater than the noise. Therefore, for this lens as well, no time delay measurement is possible based on this data.

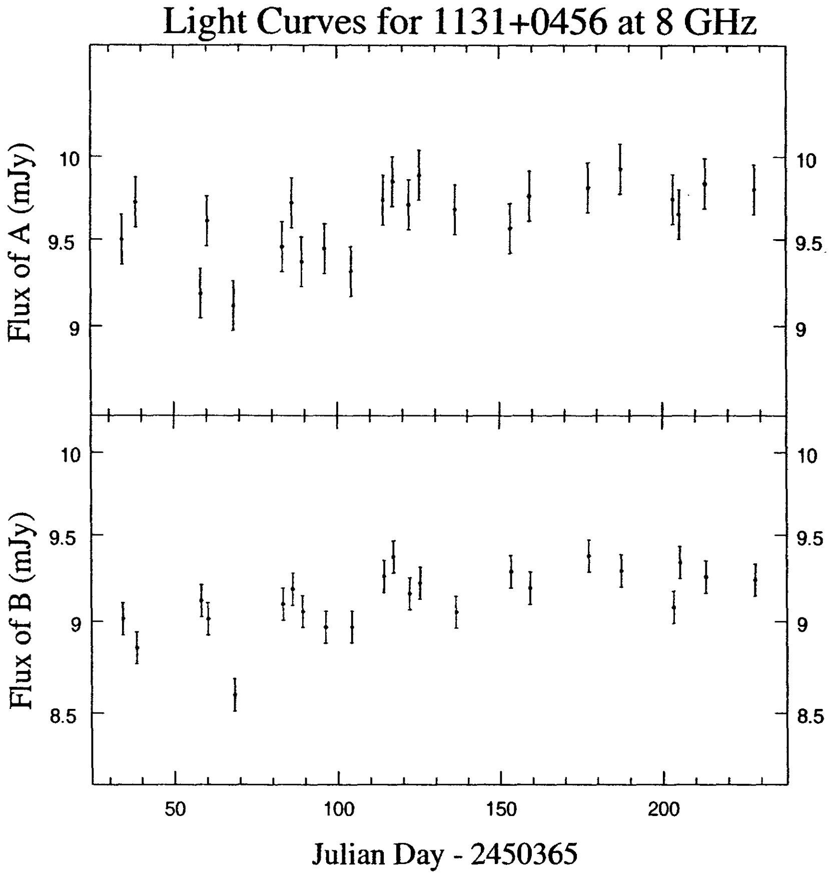

Figure 2-6: Light curves for gravitational lens 1131+0456 at 8 GHz.

2.3.5 Gravitational Lens 1830-211

Also monitored was gravitational lens 1830-211, discovered by Jauncey et al., 1991. This lens consists of two points sources with a small amount of emission from protruding arcs that don't quite form a complete Einstein ring (see Figure 2-7). The arcs probably arise from jets emanating from the radio core point source and coming close to, but not quite covering the point directly behind the center of the lensing mass. Again, we will monitor the point source images of the radio core, A and B, to try measure a time delay.

Because the extended emission in the arcs makes this source too complicated fit a model to the UV data, we made images of each observation just as we did for lenses 1938+666 and 1131+0456. For this lens however, the radio core points source images are clearly identifiable since they are much brighter than the surrounding emission.

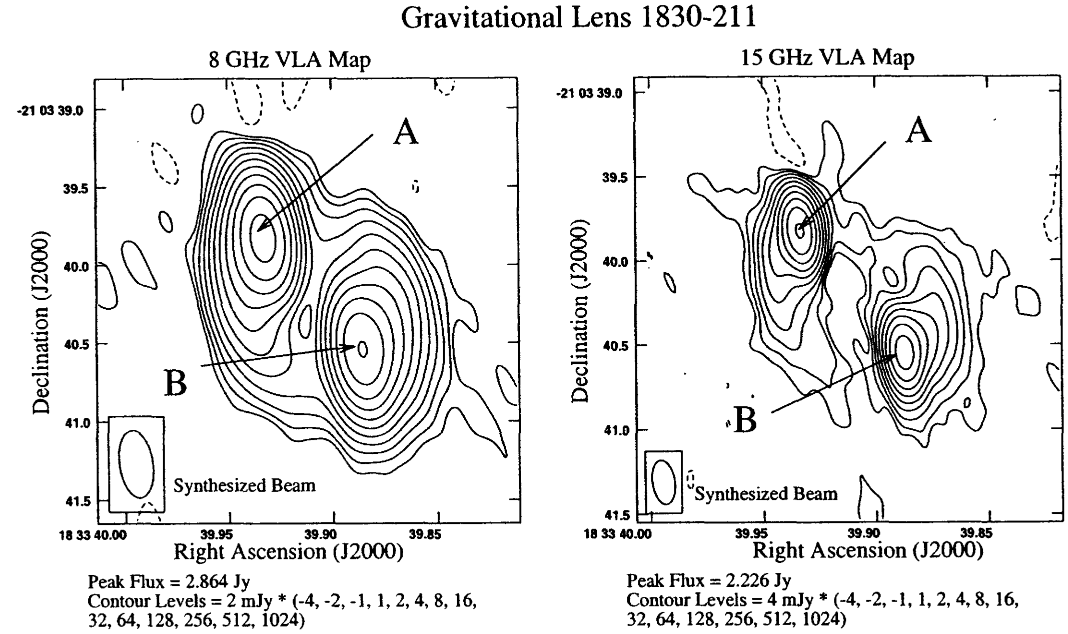

Figure 2-7: VLA maps of 1830-211 at 8 GHz and 15 GHz.

In this case, we found it advantageous to scale and rotate the map so that each of the points sources was located exactly in the center of a map pixel. The flux of this pixel was then taken as our flux measurement. Since the pointing of the VLA is only accurate to about 0.1", and our pixels were about 0.02" on a side, it was necessary to align spatially all the images to make sure the point sources were located on the intended pixels. This was done by taking a model of 1830-211 from one of our better images to which we phase-only self calibrated each data set. Since the shifting of the image corresponds only to a constant phase correction to all the visibilities in the data set, calibrating all the data sets to the same model was sufficient to attain spatial alignment. This calibration to another data set has the potential to bias the flux values of the point sources which could have varied from the model to the data set of interest. To correct for this, we then perform several iterations of self calibration to restore the flux values to there natural level at that epoch. In our experience, the flux values had converged by the third iteration of self calibration.

The resulting light curves are shown in Figure 2-8. There is clear variability visible at both 8 GHz and 15 GHz and in both components. It also seems that at each frequency, one can visually identify subtle features in the A and B light curves

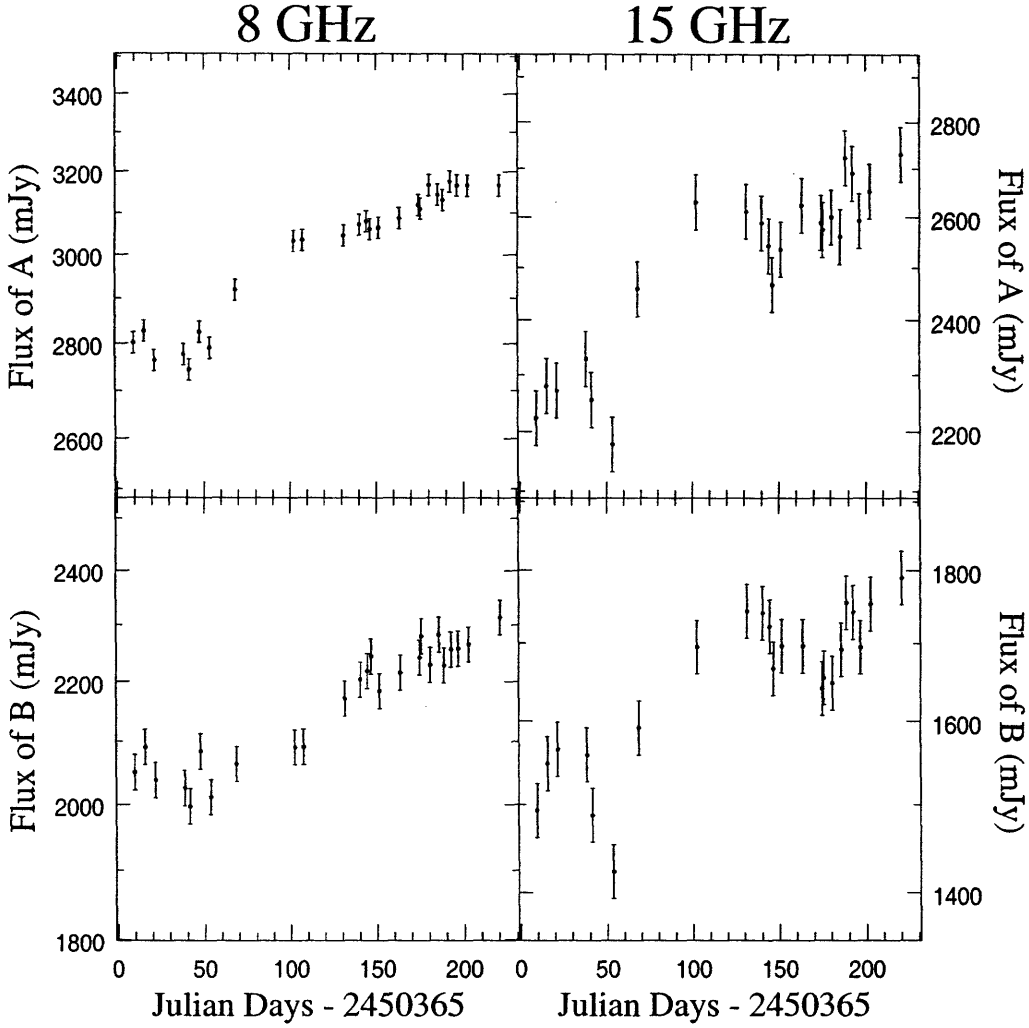

Figure 2-8: Light curves for 1830-211 at 8 GHz and 15 GHz.

that are similar but shifted in time from one to the other. Therefore these light curves represent a reasonable potential for a time delay measurement. However because the variations are small compared to the measurement errors, it is unlikely that a very accurate result could be obtained from these data alone.

2.3.6 Gravitational Lens 0218+357

The final lens in this chapter for which we will present light curves is 0218+357, which was introduced in Chapter 1. This lens consists of a doubly imaged radio core as well as an Einstein ring (see Figure 2-9) and a faint jet that is not multiply imaged (best

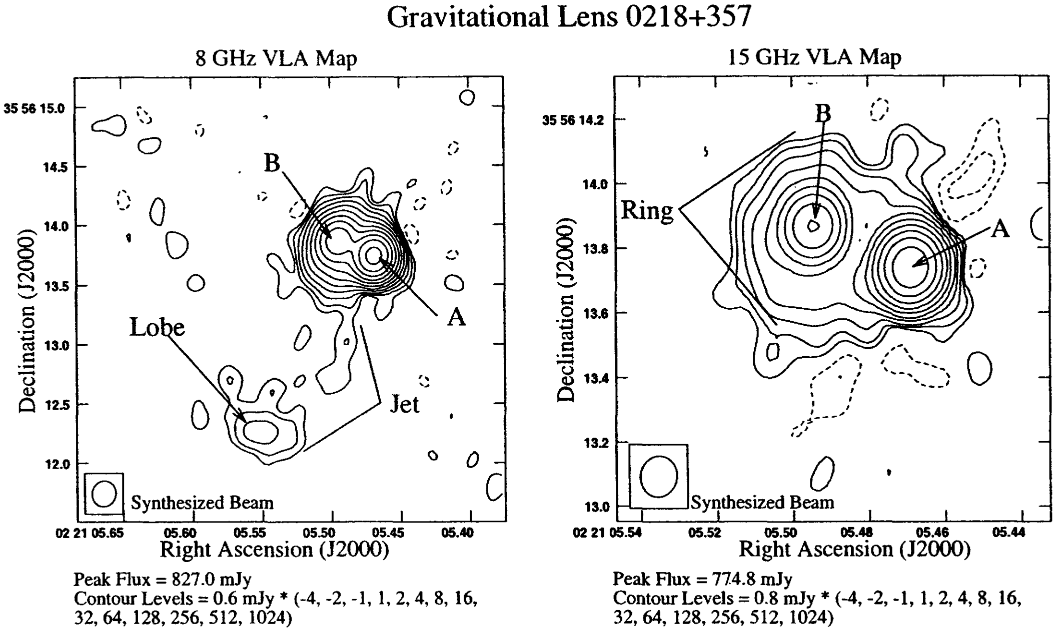

Figure 2-9: These are VLA maps of 0218+357 at 8 GHz and 15 GHz.

seen in the 8 GHz map of Figure 2-9). Presumably it is a portion of this jet that is located just behind the center of mass of the lensing object and is therefore imaged into a full Einstein ring. The separation of the radio core images is only about .35" making this by far the smallest gravitational lens known.

Again we will be measuring the flux of the two point sources to measure a time delay. The method used is virtually identical to that used for 1830-211. The maps produced from the UV data are once again scaled and rotated so that the point sources fall on the centers of map pixels. Variations due to different UV coverage are removed by creating synthetic light curves.

The resulting light curves are shown in Figure 2-10. At both frequencies we see a clear "up and down" change in the flux of each component. Also clear is that this feature occurs slightly later in the B image than in the A image. This lens therefore has very good potential for time delay measurement, which will be discussed in the next chapter.

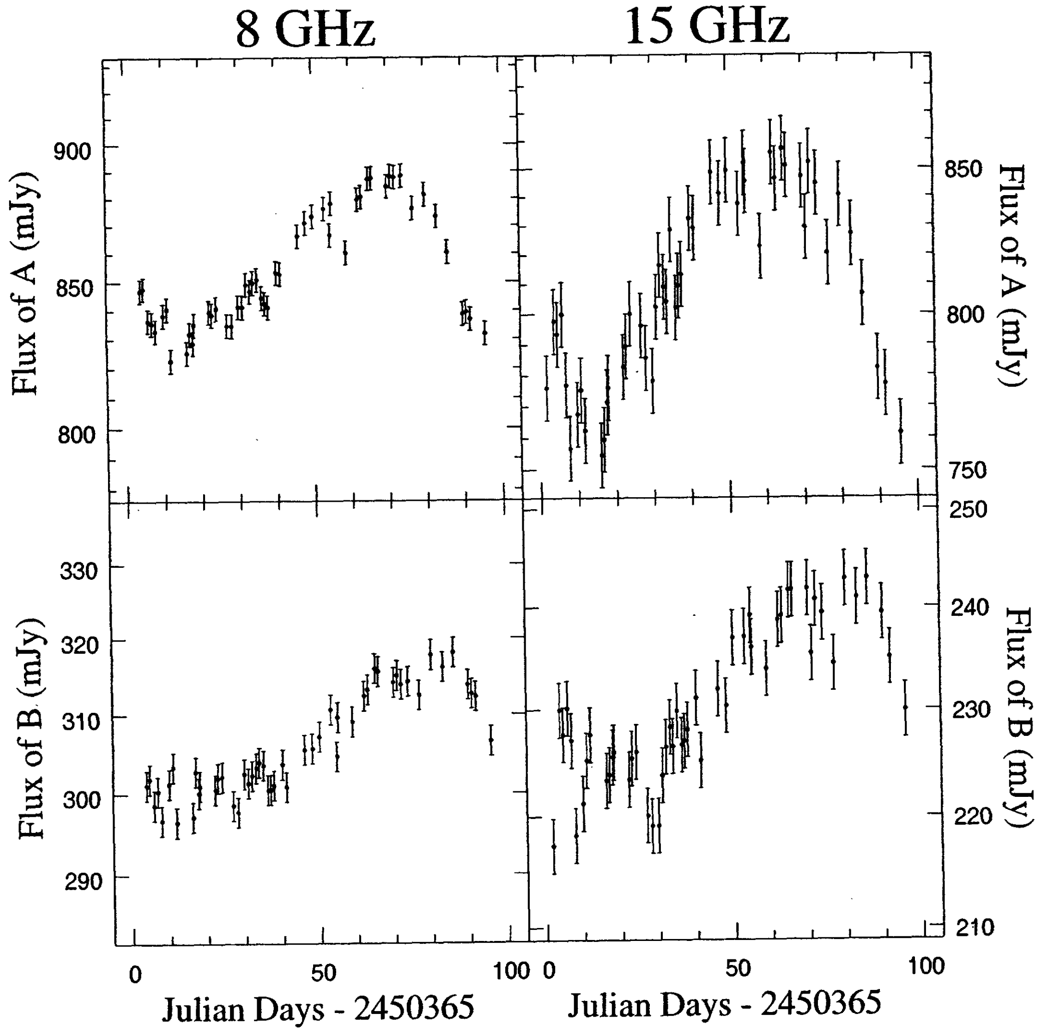

Figure 2-10: Light curves for 0218+357.

REFERENCES

Bernstein, G. , Fischer, P. , Tyson, J. A. & Rhee, G. 1997, ApJ, 483, L79

Biggs, A. D., Browne, I. W. A., Helbig, P., Koopmans, L. V. E., Wilkinson, P. N. & Perley, R. A. 1999, MNRAS, 304, 349

Chen, G. H., Kochanek, C. S. & Hewitt, J. N. 1995, ApJ, 447, 62

Clark, B. G. 1980, A&A, 89, 377

Falco, E. E., Gorenstein, M. V. & Shapiro, I. I. 1991, ApJ, 372, 364

C. D. Fassnacht, T. J. Pearson, A. C. S. Readhead, I. W. A. Browne, L. V. E. Koopmans, S. T. Myers, P. N. Wilkinson, 1999, astro-ph/9907257 (Accepted by ApJ)

Florentin-Nielsen, R. 1984, A&A, 138, L19

Grogin, N. A. & Narayan, R. 1996, ApJ, 464, 92

Grogin, N. A. & Narayan, R. 1996, ApJ, 473, 570

Haarsma, D. B., Hewitt, J. N., Lehar, J. & Burke, B. F. 1997, ApJ, 479, 102

Haarsma, D. B., Hewitt, J. N., Lehar, J. & Burke, B. F. 1999, ApJ, 510, 64

Hewitt, J. N., Turner, E. L., Schneider, D. P., Burke, B. F. & Langston, G. I. 1988, Nature, 333, 537

Hogbom, J. A. 1983, Indirect Imaging. Measurement and Processing for Indirect Imaging. Proceedings of an International Symposium held in Sydney, Australia, August 30-September 2, 1983. Editor, J.A. Roberts; Publisher, Cambridge University Press, Cambridge, England, New York, NY, 1984. LC # QB51.3.E43 I53 1984. ISBN # 0-521-26282-8. P.247, 1983, 247

Jauncey, D. L., et al. 1991, Nature, 352, 132

King, L. J., Browne, I. W. A., Muxlow, T. W. B., Narasimha, D., Patnaik, A. R., Porcas, R. W. & Wilkinson, P. N. 1997, MNRAS, 289, 450

Kundic, T. , et al. 1997, ApJ, 482, 75

Kundic, T. , Hogg, D. W., Blandford, R. D., Cohen, J. G., Lubin, L. M. & Larkin, J. E. 1997, AJ, 114, 2276

Lehar, J., Hewitt, J. N., Burke, B. F. & Roberts, D. H. 1992, ApJ, 384, 453

Lovell, J. E. J., Jauncey, D. L., Reynolds, J. E., Wieringa, M. H., King, E. A., Tzioumis, A. K., MCCulloch, P. M. & Edwards, P. G. 1998, ApJ, 508, L51

Patnaik, A. R., Browne, I. W. A., Walsh, D., Chaffee, F. H. & Foltz, C. B. 1992, MNRAS, 259, 1P

Press, W. H., Rybicki, G. B. & Hewitt, J. N. 1992, ApJ, 385, 404

Schechter, P. L., et al. 1997, ApJ, 475, L85

Vanderriest, C., Schneider, J., Herpe, G., Chevreton, M., Moles, M. & Wlerick, G. 1989, A&A, 215, 1

Wisotzki, L. , Wucknitz, O. , Lopez, S. & Sorensen, A. N. 1998, A&A, 339, L73

Chapter 3

Time Delay Determinations for the Gravitational Lens 0218+357.

This chapter is largely based on a paper submitted for publication to the Astrophysical Journal, (Cohen et. al., 2000).

3.1 Time Delay Analysis

From the light curves for the gravitational lens 0218+357 (Figure 2-10) we seek to derive the time delay in this system. One can easily estimate the time delay between the light curves of components A and B by eye, but it is preferable to have an objective method that gives reproducible results and a quantitative estimate of the errors. Two such methods are presented and applied in this chapter. The first is the maximum likelihood method of Press, Rybicki & Hewitt (1992a,b; henceforth PRH). The second method is the "minimum dispersion method" of Pelt et. al (see Pelt et al., 1994, and Pelt et al., 1996).

VLA monitoring observations of 0218+357 have also been carried out by another research group (Biggs, et al. (1999)), and they report a time delay of 10.5 ± 0.4 days (95% confidence). They also report significantly different flux ratios of 3.57 ± 0.01 and 3.73 ± 0.01 (68% confidence) at 8 GHz and 15 GHz, respectively. These results are based on data spanning approximately the same 100 day period for which our data were taken. We report in this chapter our estimate of the time delay which is based on our independent VLA measurements of 0218+357, in which we used data reduction and parameter fitting techniques that differed from those of Biggs et al. We also adopt a more general model of the source variability, including the possibility of constant and variable components with different magnification ratios. At the end of this chapter the we will compare the results of both efforts and discuss any differences.

A comparison of the results addresses the issue of the robustness of the parameter estimates. We caution, however, that since our monitoring observations occurred at the same epoch as those of Biggs et al. and are based on the same feature in the light curve, the effect of any unmodeled scintillation or microlensing cannot be assessed.

3.2 Basic Ideas in Time Delay Analysis

Inherent in all methods of time delay analysis is the assumption that the light curves for components A and B are identical except for a shift along the time axis caused by the time delay and a scale factor difference in the flux density axes caused by the different magnifications of each image. This assumption can be expressed with the following equation:

$$F_A(t) = R\,F_B(t+T) \tag{3.1}$$

where $F_A(t)$ and $F_B(t)$ represent the flux density as a function of time for components A and B respectively, T is the time delay and R is the magnification ratio between A and B. The light curves are simply measurements of $F_A(t)$ and $F_B(t)$ over the time interval of the observations. Time delay analysis consists of using the light curves to determine the two remaining parameters in Equation 3.1, T and R.

The reasoning behind Equation 3.1 is the fact that the two components are images of the same object. After correcting for the time delay and the magnification of each component, each of the two light curves should become the same light curve – that of the single, unlensed source object. This is generally the case, however there are complications.

The first complication has to do with the fact that the different light paths travel through different regions of space. It is possible that one of the light paths might be gravitationally microlensed by a compact object in the lensing galaxy or in the halo of our own galaxy. Also possible is that scintillation by the interstellar medium could affect each light path differently. These conditions are probably rare for radio sources; however, they do raise the possibility that light curves for multiple images of the same source object could differ in shape. The initial controversy over the time delay in 0957+561 was likely caused by such a factor, which was resolved only when light curves over much longer time periods became available. It is also possible that one of these factors may be responsible for the apparent differences in shape among the light curves we observed for the lens 1422+231 (see Figure 2-2). The best way to eliminate this complication in determining time delays is to measure light curves over a long time period that ideally includes many features. That way the effect of any incidence of microlensing or scintillation will be minimized.

Another complication to Equation 3.1 is much more common. This is the fact that often what is identified as the radio core in a VLA image turns out to be made up of more than one component when observed under much higher resolution. This was in fact demonstrated to be the case for 0218+357 with VLBA images presented by Patnaik et al. (1995). For any AGN, there is only one true core, so the other components must be small bright sections of the jets. Only the core's brightness can vary over the time scales in which we are interested. Therefore, the total flux density we measure with the VLA could be comprised of both the variable core as well as other emission that is not variable. This alone does not violate Equation 3.1. Different magnification gradients across the core and jets of each image will cause the flux ratio of the variable and constant components in each image to be different. Therefore the variations in each light curve could comprise different fractions of the total flux of each component. That would violate Equation 3.1. However, unlike the first complication, this effect can be modeled while performing the time delay analysis. This is done by modifying Equation 3.1 to include the constant parts of each component. Letting C_A and C_B be flux densities of the constant components in images A and B respectively, we then have:

$$F_A(t) + C_A = R\,(F_B(t+T) + C_B) \tag{3.2}$$

where we define R as the flux ratio of the variable components only. This nominally implies that time delay analysis requires the fitting of four different parameters: T, R, C_A and C_B. However, as shown by Press & Rybicki, 1998, we cannot fit for both C_A and C_B. A parameter for which we can solve is $C_o = R\,C_B - C_A$, which essentially tells us the difference in constant flux densities in images A and B. Now our model of the relation between the light curves for A and B an be expressed as follows:

$$F_A(t) = R\,F_B(t+T) + C_o \tag{3.3}$$

Thus there are three independent parameters, T, R, and C_o, that determine the difference between light curves A and B. All three of these parameters must be solved for in order to determine the time delay. The difference between various methods of time delay analysis is that each one employs different techniques for using the light curves to determine the most likely values of these three parameters.

3.3 The PRH Method

3.3.1 Summary of PRH Method

The first method we consider for determining the time delays is the maximum likelihood method developed by PRH. The PRH method is based first on determining the statistical qualities of the A and B light curves individually. Then the B light curve is transformed according to trial values of T, R, and C_o and then combined with the A light curve to create a single light curve with twice as many points. Then the statistical properties of the combined light curve are determined. The parameters T, R, and C_o are fit so that the statistical qualities of the combined light curve best match that of the individual light curves.

The statistical quality used by the PRH method is the amount of correlation between points on the light curve as a function of the time lag between measurements. We expect a greater correlation between measurements with smaller separations in time. The difference between any two flux measurements is caused by two factors, the measurement errors and the actual flux variations in the source. We need to understand both of these.

3.3.2 Flux Measurement Errors

First, we estimate the measurement errors. This is done empirically for each light curve by taking as our error estimate the average flux difference between points separated in time by less than some small time interval D. D is chosen small enough so that there will be little intrinsic variation in the source yet large enough so that there will be a fair sampling of points with time lags less than D. For 0218+357 we choose $D = 2$ days. This assumes that within any time period of length D, the variations are dominated by measurement errors and not actual source variability. To the extent that this is not true, we can consider our result to be an upper limit on the measurement errors.

Normally one would assume that the measurement errors for different points in the light curve are uncorrelated. This is mostly true, but as discussed in Chapter 2, the measurement errors are caused partly by errors in the flux calibration in each image. Therefore, the measurement error for the A and B components taken from a single image will share the portion of the measurement error that comes from flux calibration. In the combined light curve, the A and B points from a single image will be separated in time by the trial time delay, T. But the errors *will* be correlated between these two points. To estimate how much of the total error is correlated versus uncorrelated between the A and B light curves, we create a light curve such that each point has a value equal to the ratio of the flux densities of A and B. In this A/B light curve, all the correlated errors will divide out. So we can estimate the error in the A/B light curve just as we did for the individual light curves to estimate the uncorrelated error. We take the total error to be the average of the error from the A

Estimated Measurement Errors for 0218+357

frequency ν (GHz)	A error	B error	Total error (averaged)	A/B error (uncorrelated)	remaining error (correlated)
8.4	0.49%	0.62%	0.56%	0.34%	0.44%
15	1.3%	1.2%	1.25%	0.90%	0.87%

Table 3.1: Estimated errors for individual light curves and estimated correlated and uncorrelated errors at each frequency for gravitational lens 0218+357.

light curve and B light curve. Then the correlated error has the value such that when added to the uncorrelated error in quadrature it gives the total error. The results for each light curve are shown in Table 3.1.

3.3.3 The Structure Function

Next we need to evaluate the statistical properties of the true source variation. This is done by estimating the structure function, $V(\tau)$, of the light curve. The structure function is defined as one half the average square of the flux difference between points as a function of the time difference, τ, between the measurements. If we separate the measurement errors, $e(t)$ from the true flux density, $s(t)$, then the measured flux density is:

$$f(t) = s(t) + e(t), \tag{3.4}$$

and the structure function is defined as:

$$V(\tau) \equiv \frac{1}{2} < [s(t) - s(t-\tau)]^2 > \tag{3.5}$$

where $f(t)$ is the flux value at time t and the brackets $< >$ denote the expected value. Since we can't measure $s(t)$ directly, in order to determine empirically the functional form of Equation 3.5, we need the following relation:

$$\frac{1}{2} < [s(t) - s(t-\tau)]^2 >= \frac{1}{2} < [f(t) - f(t-\tau)]^2 > - < [e(t)]^2 > \tag{3.6}$$

We already know the expected value of $e(t)$ from the error estimates in Table 3.1. We can apply Equation 3.6 to the data in the light curves to come up with an empirical structure function. Every pair of points in the light curve will result in one point on the structure function. With 51 points in the 0218+357 light curves, there are 1275 points estimates of the structure function. Since we do not know yet the flux ratio between components A and B, we take $f(t)$ to be the natural logarithm of the flux density measured at time t referred to 1 mJy, removing the dependence of our analysis on the unknown flux ratio. (We will continue to use log units throughout the analysis.) The point estimates were binned in groups of 100 to produce the plot shown in Figure 3-1.

Initially the most surprising feature of the empirical structure functions was the fact that they appear very different for light curves A and B at each frequency. Component B appears more strongly auto-correlated at small time lags than component A. This is of course unexpected since components A and B are images of the same source object. Since radiation from the two components travels along different paths to reach the observer, such a comparison may reveal differences in propagation characteristics, such as scintillation or gravitational microlensing, as discussed in Section 3.2.

To investigate this possibility it is necessary to first determine if the differences between the structure functions of different components is statistically significant. We do this empirically with Monte Carlo simulations. First, a power law model of the form:

$$V(\tau) = K\,\tau^{\alpha} \tag{3.7}$$

is fit to each structure function. The four resulting structure function models were used to generate four sets of Gaussian Monte Carlo simulations, of 1000 realizations each, and empirical structure functions were computed for all the simulated data sets. From these the mean and the 68% confidence interval were computed for each value of τ. The results are the error bars shown in Figure 3-1. Although our error estimates are to some extent model dependent, it is clear that the differences in the structure

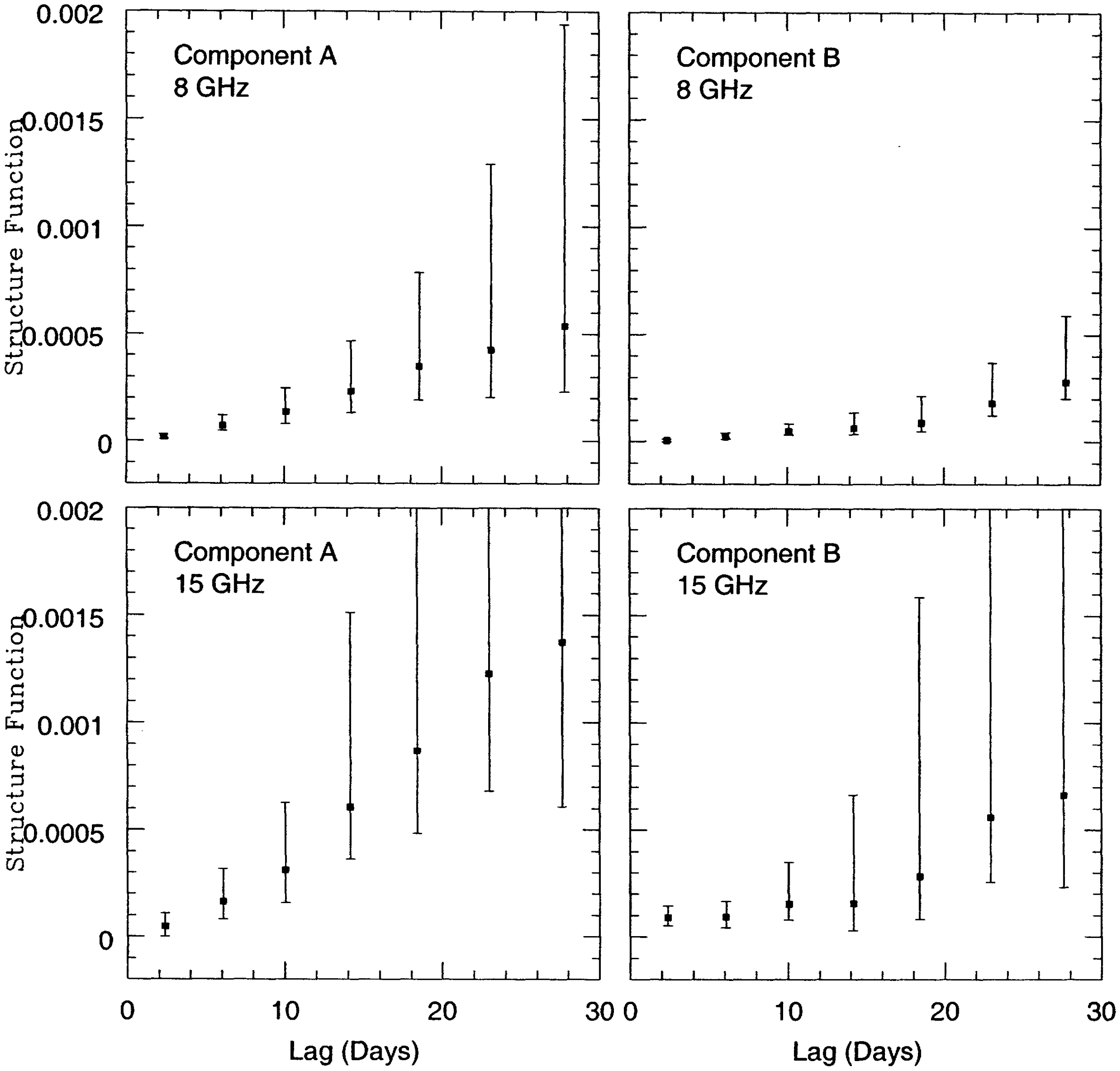

Figure 3-1: Empirical point estimates of the structure function for the 8 GHz and 15 GHz light curves for A and B of the gravitational lens 0218+357. The points are binned in groups of 100. The error bars are derived from Monte Carlo simulations and show that the differences in the structure functions are not significant. Structure functions are computed according to Equation 3.6, with flux densities expressed in natural logarithm units referenced to 1 mJy.

functions are not significant. Much longer time series would be necessary to explore propagation effects in this way.

It is also clear that we do not have enough data to measure the intrinsic structure function with a high degree of accuracy. Therefore, we have to refer to other data and theory about extragalactic variable sources in general to make reasonable assumptions. In particular, over 25 years of monitoring the flux density of many quasars and BL Lac objects (Hughes, Aller & Aller, 1992) show that for quasars, the structure function value of α is 1.04 ± 0.18 for light curves which are not dominated by a single feature (which tends to give an upward bias on the measurement of α). For BL Lac objects, $\alpha = 0.94 \pm 0.37$. There are also theoretical arguments that are consistent with this; the value of α is exactly unity for such natural random processes as shot noise and random walk. It is reasonable, therefore, to assume that $\alpha = 1$ in the intrinsic structure function and only solve for K. We will use this assumption throughout our analysis.

3.3.4 Fitting for T, R and C_o.

As described in Section 3.3.1 the PRH method is based on combining the A and B light curves according to trial parameters and then investigating how closely the statistical qualities of the combined light curve match that of the original light curves. For the individual light curves the error estimates and a power law fit to the structure function comprise the statistical characteristics we will use. As for the expected measurement error, we use the average of the error estimates for each A and B light curve (see Table 3.1). Our estimate of the structure function is the average of the two power law fits (Equation 3.7) to the empirical structure functions for light curves A and B. Since we assume that $\alpha = 1$ for each light curve, the averaged power law will also have $\alpha = 1$. The value of K will be different for each light curve, so we average them by taking the geometric mean. This gives us one value for the fractional measurement error and one power law fit to the structure function. For 0218+357, the results were $< K >= 1.2 \times 10^{-5}$ at 8 GHz and $< K >= 3.1 \times 10^{-5}$ at 15 GHz.

Now we must determine how well the combined light curve matches these statistical factors. As shown by PRH and Rybicki & Kleyna, 1994, the degree of "matching" can be quantified by what is referred to as the "Q-statistic":

$$Q = y^T B^{-1} y - \ln \det(B^{-1}) \tag{3.8}$$

where y is the vector of flux density values for the recombined light curve and B is the total covariance matrix as defined by PRH. Using Equation 3.4, we can use the following expression for the elements of the covariance matrix, B:

$$B_{ij} =< s^2(t) > -V(\tau)+ < e(t_i)e(t_j) > \tag{3.9}$$

The first term on the right-hand side is simply the average square of the flux density values and is the same for all B_{ij}. The second term is the structure function that we have estimated empirically. Because the measurement error in different measurements is uncorrelated, last term is always zero except for two cases. The first case is when $i = j$ and $< e(t_i)e(t_j) >=< e^2(t) >$, the average square of the measurement errors. The other case occurs when $i \neq j$ but (because of the shift by the time delay) the two flux density measurements come from the same observation and so the errors are not uncorrelated. In this case we must use the expected value of the *correlated* errors as calculated in Table 3.1. In this way we account for the correlated flux density scale errors. Combining the light curves for trial values of T, R, and C_o, we find the best-fit values of these parameters by minimizing the Q-statistic. The final results for 0218+357 were T = 9.6 days, R = 3.2, and C_o = 110 mJy for 8 GHz; and T = 11.3 days, R = 4.3, and C_o = 180 mJy for 15 GHz.

3.4 The Minimum Dispersion Method

3.4.1 Summary of the Minimum Dispersion Method

The Pelt et al. minimum dispersion method is similar to the PRH method in that it also attempts to find recombination parameters that minimize a statistical quantity associated with the combined light curve. The quantity in this case is the "dispersion," which is defined as the average square of the difference in flux density values of nearby points in the light curve. "Nearby" is defined as points that are spaced apart in time by less than the decorrelation length, δ. The contribution of any such pair of points is then weighted by the factor $(1 - \tau/\delta)$ where τ is the time between the two points (Pelt et al., 1996). Since we give all the points in the light curves equal weight, our dispersion statistic is:

$$D = \frac{\sum_{i,j} S_{i,j}(f(t_i) - f(t_j))^2(1 - \frac{\tau}{\delta})}{\sum_{i,j} S_{i,j}(1 - \frac{\tau}{\delta})} \tag{5}$$

where

$$\tau = |t_i - t_j| \quad \text{and} \quad S_{i,j} \begin{cases} = 1 & \text{if } \tau < \delta \\ = 0 & \text{if } \tau \geq \delta \end{cases} \tag{6}$$

As in the PRH method, we fit T, R, and C_o so as to minimize the dispersion in the combined light curve. It is unclear, however, what value to use for δ. Therefore, we tried a range of values of δ and found best-fit values of the parameters as a function of δ.

3.4.2 Results of the Minimum Dispersion Method

The results of the minimum dispersion method are shown in Figure 3-2, plotted as a function of the assumed decorrelation length δ. The results vary by ±10% as a function of δ, even without any consideration of the errors in the parameters. The values of T are generally centered around the values we found with the PRH method. However, since we have no knowledge of the actual value of δ for either light curve, we conclude that no definitive determination of the parameters could be made with the dispersion method. Although successful in determining the time delay in 0957+571 (Pelt et al. 1996), the method is inconclusive here, probably because in this case we have a much shorter monitoring period.

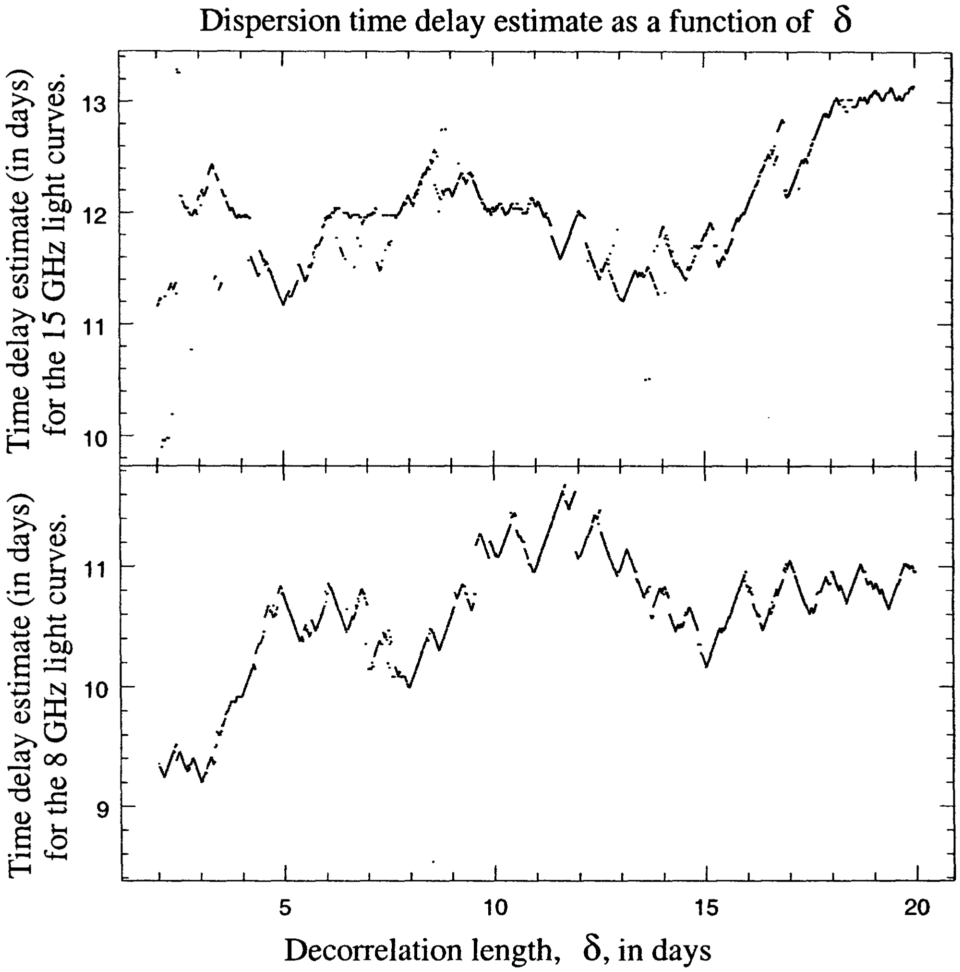

Figure 3-2: The best fit time delay and variable ratio as determined by the minimum dispersion method, plotted as a function of the "decorrelation length", δ (in days). Since we have no a priori knowledge of δ, this technique does not provide definitive values for the parameters.

3.5 Error Analysis for PRH Results

To estimate the accuracy of the PRH parameter fitting procedure for our case, we repeated the PRH analysis with two sets of simulated data. The first set assumes that the underlying process producing the light is Gaussian; the second makes no such assumption and instead derives the simulated data from the real data.

3.5.1 Gaussian Monte Carlo Simulations

As described by PRH, we created simulated light curves with the same sampling in time as the true light curves, with flux density values produced by assuming a Gaussian process with the same structure function and errors that we derived from the measured light curves. The measurement errors consisted of both correlated and uncorrelated parts, as described in Sections 3.3.2 and 3.3.4.

Errors Due to an Incorrect Structure Function

As described in section 3.3.3, with our limited time series, we could not measure the structure functions to high precision. It is necessary to determine how this could affect the final results. Therefore, our first application of the Monte Carlo simulations was to investigate the effect of an incorrect structure function on our estimate of the time delay, T. For each light curve, simulations were performed with the time delay varying randomly and uniformly between 0 and 20 days. The differences between the actual time delays and the fitted time delays were computed, and standard deviations of the set of differences were calculated. It is important to realize that for these calculations *two* structure functions are involved. The first is used to create the simulated data, and we call this the "true" structure function. The second is the one we fit to the simulated data in the process of estimating the time delay; we call this the "assumed" structure function. Varying both the true and assumed structure functions in our simulations allows us to test the effects of an incorrect assumed structure function on our time delay estimation, as a function of the true structure function.

Of the two free parameters in a structure function, K and α, the value of α was

Error Estimates as a Function of "True" α and "Assumed" α

"Fitted" α	$\alpha_{true} = 0.5$	$\alpha_{true} = 0.75$	$\alpha_{true} = 1.00$	$\alpha_{true} = 1.25$	$\alpha_{true} = 1.50$
0.5	$1\sigma = 0.42$	$1\sigma = 0.42$	$1\sigma = 0.48$	$1\sigma = 0.59$	$1\sigma = 0.82$
	$2\sigma = 1.72$	$2\sigma = 1.35$	$2\sigma = 1.40$	$2\sigma = 1.46$	$2\sigma = 1.73$
0.75	$1\sigma = 0.48$	$1\sigma = 0.41$	$1\sigma = 0.44$	$1\sigma = 0.56$	$1\sigma = 0.70$
	$2\sigma = 1.81$	$2\sigma = 1.23$	$2\sigma = 1.32$	$2\sigma = 1.41$	$2\sigma = 1.80$
1.00	$1\sigma = 0.60$	$1\sigma = 0.42$	$1\sigma = 0.42$	$1\sigma = 0.54$	$1\sigma = 0.69$
	$2\sigma = 2.04$	$2\sigma = 1.16$	$2\sigma = 1.11$	$2\sigma = 1.23$	$2\sigma = 1.59$
1.25	$1\sigma = 0.67$	$1\sigma = 0.49$	$1\sigma = 0.48$	$1\sigma = 0.49$	$1\sigma = 0.68$
	$2\sigma = 2.29$	$2\sigma = 1.42$	$2\sigma = 1.22$	$2\sigma = 1.30$	$2\sigma = 1.68$
1.50	$1\sigma = 0.98$	$1\sigma = 0.67$	$1\sigma = 0.26$	$1\sigma = 0.55$	$1\sigma = 0.62$
	$2\sigma = 2.82$	$2\sigma = 1.79$	$2\sigma = 1.18$	$2\sigma = 1.49$	$2\sigma = 1.49$

Table 3.2: Results of Monte Carlo simulations for various "true" and "assumed" structure functions. In each case, the synthetic light curves were created using a structure function with a given α (the "true" α). A structure function was then fit to the synthetic light curves with the condition that α be fixed at a given value (the "assumed" α). This fitted structure function was then used to get the time delay. The time delay derived from this technique was compared to the actual time delay in each case. For each pair of true α and assumed α, 1,000 synthetic light curves were produced. In each case the accuracy of the time delay fitting was expressed as 1σ and 2σ error bars, given in units of days.

chosen and the value of K was fitted, reproducing our analysis procedure. For the "true" structure functions a "true" α was chosen and the "true" K was fit to the real (measured with the VLA) light curves. For the "assumed" structure functions an "assumed" α was chosen and the "assumed" K was fit to the simulated light curves. Then the effectiveness of the PRH method was tested for values of "true" α and "assumed" α that ranged in five steps from 0.50 to 1.50. For each case, we performed 1,000 Monte Carlo simulations. The first result of this test showed that the average deviation between the actual time delay and the PRH-deduced time delay was less than .02 days. This was the case regardless of how the "true" and "assumed" values of α were varied. Therefore, it seems unlikely that an incorrect "assumed" structure function could have produced a significant bias in the time delay measurements. However, the error estimates for each measurement did change somewhat as the structure functions were varied. Table 3.2 shows how the error estimates change as function of "true" α and "assumed" α. The "true" α has much more of an effect on the error estimates than the "assumed" α. This indicates that the magnitude of the error estimates depends mostly on the intrinsic structure function of the BL Lac object and very little on the accuracy of the fitted structure function. Thus, the reliability of our error estimates appear to be limited by our knowledge of the intrinsic structure function. In all further simulations we assume $\alpha = 1$.

Confidence Intervals

After settling on a reasonable structure function, we concentrate on our ability to determine confidence intervals for the three parameters T, R, and C_o. We expect T and possibly R to be the same for both frequencies, but the C_o parameter is likely to be different at the two frequencies. We again constructed Monte Carlo light curves, but now allowing all three parameters to vary. T was varied between 8 and 12 days; R was varied between 2 and 5; and C_o was varied between 0 and 200 mJy. For the light curves, the fitted values were compared to the true values, and 95% confidence intervals were derived and adopted as the errors on the parameter estimates. The distributions are shown in Figure 3-3. The parameters T and R for the two frequencies

Results with Monte Carlo Error Estimates (95% confidence)

ν	T (days)	R	C_o (mJy)
8 GHz	$9.6^{+1.3}_{-1.2}$	$3.2^{+0.3}_{-0.4}$	110^{+80}_{-110}
15 GHz	$11.3^{+2.0}_{-1.8}$	$4.3^{+0.5}_{-0.8}$	180^{+100}_{-140}
combined	$10.1^{+1.1}_{-1.0}$	$3.4^{+0.2}_{-0.4}$	

Table 3.3: Results of fitting the time delay (T), variable ratio (R) and excess constant component (C_o) to minimize the PRHQ statistic for the 8 GHz and 15 GHz light curves. The error bars (95% confidence) are determined from Monte Carlo simulations. The last line of the table shows the combined result from the two light curves.

were averaged, weighted according to their errors. The results are presented in Table 3.3.

3.5.2 Jackknife Samples

The confidence intervals derived in the previous section are based on the assumption that the underlying process producing the quasar light curves is a Gaussian process and on the model we assumed for the errors. This is a weakness of our Gaussian Monte Carlo technique, and we seek to explore methods that derive the statistics of the process from the data themselves. One such method is the jackknife (Tukey, 1958; see also Efron & Tibshirani, 1993), in which "jackknife samples" are formed by successively deleting one point from the data set. We applied this technique to our light curves at both frequencies, estimating the T, R, and C_o parameters for each jackknife sample and forming distributions of the fitted values, shown in Figure 3-4.

We compute errors on the parameters by forming the 95% confidence intervals from the data of Figure 3-4, multiplying each distribution by the necessary "expansion factor" $(N-1)/\sqrt{N}$ (see Efron & Tibshirani, 1993). Values from the different frequencies for T and R are combined as described above, and the results are presented in Table 3.4. We caution that since the light curve data points are not independent, the jackknife simulations are likely to underestimate the true errors.

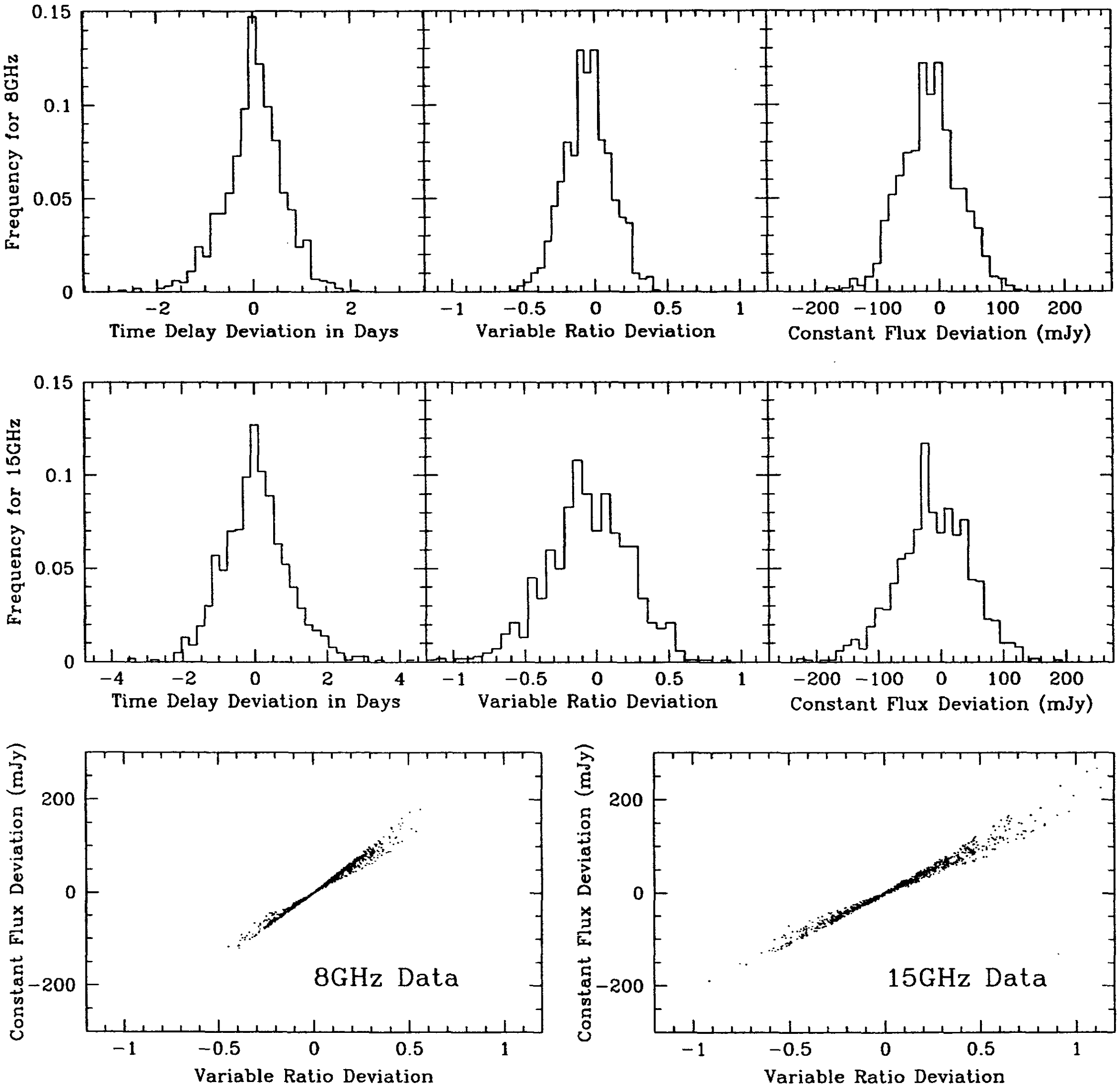

Figure 3-3: Histograms that display the error distribution for each parameter as deduced from Monte Carlo simulations of the 8 GHz and 15 GHz light curves. The "deviation" in each case is the difference between the fitted and true values. The bottom two panels compare the C_o deviation to the R deviation for each simulated data set. There is clearly a high correlation between the two. This demonstrates that if either C_o or R is known *a priori*, the other parameter is well constrained. However, the two parameters cannot be constrained simultaneously with these data.

Results with Jackknife Error Estimates (95% confidence)

ν	T (days)	R	C_o (mJy)
8 GHz	$9.6^{+1.7}_{-2.6}$	$3.2^{+0.2}_{-0.3}$	110^{+70}_{-80}
15 GHz	$11.3^{+4.3}_{-2.0}$	$4.3^{+0.4}_{-0.6}$	180^{+90}_{-150}
combined	$10.1^{+1.5}_{-1.6}$	$3.4^{+0.2}_{-0.2}$	

Table 3.4: Results of fitting the time delay (T), variable ratio (R) and excess constant component (C_o) to minimize the PRHQ statistic for the 8 GHz and 15 GHz light curves. The error bars (95% confidence) are determined from jackknife samples. The last line of the table shows the combined result from the two light curves.

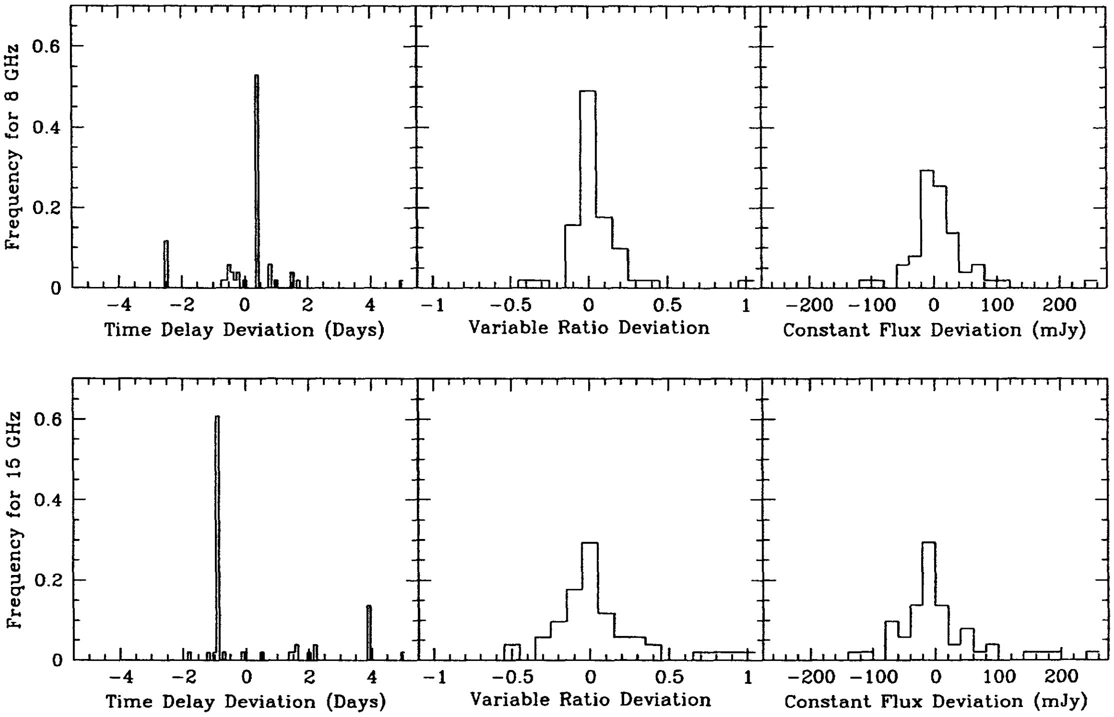

Figure 3-4: Histograms that display the error distribution for each parameter as deduced from jackknife samples of the 8 GHz and 15 GHz light curves.

3.5.3 Evaluation of Errors

If we compare the error distributions generated by the two different simulation techniques (Figures 3-3 and 3-4), a couple of interesting differences emerge. First, the jackknife distribution for the time delays is very different from the corresponding Monte Carlo distribution, and it clearly is not Gaussian. This is an indication that the Monte Carlo simulations are failing to capture the properties of the data in a way that causes estimation of the time delay distribution to be unreliable. Therefore, we adopt the jackknife errors as our errors on T. Second, the jackknife distribution for R and C_o are not as broad as the corresponding Monte Carlo distribution, but do appear Gaussian, indicating that the R and C_o estimation process is better behaved than the T estimation process. However, since there is reason to suspect the jackknife procedure may underestimate the true errors, we adopt the Monte Carlo errors as our errors on R and C_o. The differences in the distributions in Figures 3-3 and 3-4 illustrate the difficulty of reliable error estimation in these light curves, a topic that deserves further study. With the confidence intervals determined, we now see that the best-fit values of T and R for the two observing frequencies are not significantly different. Therefore, as shown in Tables 3.3 and 3.4, we form a weighted average for each of these two parameters. Our final results, with 95% confidence intervals, are: $T = 10.1^{+1.5}_{-1.6}$ days, $R = 3.4^{+0.2}_{-0.4}$, $C_o = 110^{+80}_{-110}$ (8 GHz), and $C_o = 180^{+100}_{-140}$ (15 GHz). The light curves superimposed according to the best-fit parameters are shown in Figure 3-5.

3.6 Comparison with Previous Measurement

Our time delay value of $10.1^{+1.5}_{-1.6}$ days (95% confidence) is consistent with the value of 10.5 ± 0.4 days (95% confidence) found by Biggs et al. and lends confidence to the robustness of the time delay measurements. Our results are derived from an independent set of data, very different data reduction techniques, very different parameter fitting techniques, and more general models for both the measurement errors and the variability of the background object. The light curves produced by the

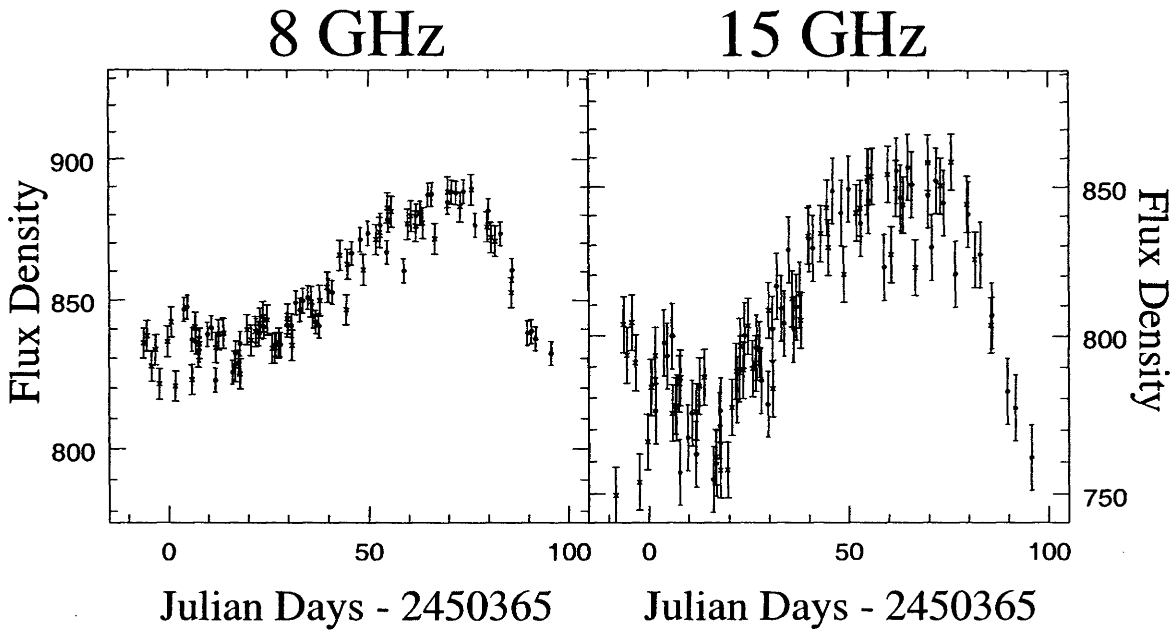

Figure 3-5: Light curves superimposed according to the best-fit time delays, magnification ratios and constant components.

two analyses are in excellent agreement, showing the same major feature. However, this is also a weakness of the comparison. It is possible that this feature is affected by microlensing or scintillation, and both analyses of the data would be biased in the same way if this is the case. Only measurements at another epoch can reduce this uncertainty.

Our error analysis results in confidence intervals for the time delay that are about a factor of four larger than those of Biggs et al. The errors on our flux density measurements are smaller than those of Biggs et al. at 8 GHz, larger at 15 GHz, but in both cases not much different. Therefore, it appears the source of the difference in confidence intervals is in the time delay fitting procedures rather than in the light curve errors. Since we parameterize our variability model differently, with three parameters associated with each light curve rather than two, it is not surprising that our confidence intervals are larger. In fact, we caution that in general an oversimplification of the model may result in deceptively small confidence intervals.

In the derivation of magnification ratios, Biggs et al. parameterized their model in terms of the ratios of the total flux densities. We separate the variable and constant parts of the flux densities, fitting for the magnification ratio associated with the variable part, and our results are not directly comparable. However, we do come to quite different conclusions concerning the size of the confidence intervals and the consistency in the magnification ratios for the two different frequencies. The fitting of our more general model shows that for the existing data there is a degeneracy between the C_o and the R parameters, so that without independent information on C_o the value of R is rather poorly determined. Therefore, we find larger confidence intervals for the values of R at the two frequencies, with the confidence intervals including the values found by Biggs et al. We believe that the more general model is plausible, and provides a natural alternative to the somewhat surprising result of Biggs et al. that the magnification ratios at the two frequencies are very significantly different. The experience of 0957+571 shows that a longer series of data that includes both variable and quiescent behavior of the quasar should determine the magnification ratios with more precision.

3.7 Conclusion

For the gravitational lens 0218+357, we find a time delay of $10.1^{+1.5}_{-1.6}$ days and a magnification ratio associated with the variable part of the light curves of $3.4^{+0.2}_{-0.4}$, both at 95% confidence. We find best-fit values (which are rather poorly determined) of the constant part of the light curves of 110^{+80}_{-110} mJy (8 GHz) and 180^{+100}_{-140} mJy (15 GHz), also at at 95% confidence. Our results, when compared to those of Biggs et al., indicate that the time delay measurement is very robust in this system, assuming the dominant feature in the light curve is not significantly affected by scintillation or microlensing.

With the time delay determined, the remaining step towards using this system to measure H_o is a model of the mass distribution in this lens. The 0218+357 system has not yet been extensively modeled. However, in this system there is a full Einstein ring in addition to the doubly imaged radio core. This ring is difficult to observe in detail because it is small (about 350 mas in diameter) and very faint compared to the radio cores. However, an accurate map of the fine structure in the ring will add many more constraints to any existing models of this system and greatly improve their accuracy. This is probably the best way to improve the measurement of the angular diameter distance to this lens. The next chapter describes our efforts to obtain such data for the purposes of improving the lens model of this system.

REFERENCES

Biggs, A. D., Browne, I. W. A., Helbig, P., Koopmans, L. V. E., Wilkinson, P. N. & Perley, R. A. 1999, MNRAS, 304, 349

Cohen, A. S., Hewitt, J. N., Moore, C. B. & Haarsma, D. B. 2000, (submitted to ApJ)

Efron, B., and Tibshirani, R. J. 1993, An Introduction to the Bootstrap (New York: Chapman & Hall, Inc.), 141-150.

Hughes, P. A., Aller, H. D. & Aller, M. F. 1992, ApJ, 396, 469

Patnaik, A. R., Porcas, R. W. and Browne, I. W. A. 1995, MNRAS, 274, L5

Pelt, J., Hoff, W., Kayser, R., Refsdal, S. & Schramm, T. 1994, A&A, 286, 775

Pelt, J., Kayser, R., Refsdal, S. & Schramm, T. 1996, A&A, 305, 97

Press, W. H., Rybicki, G. B. & Hewitt, J. N. 1992, ApJ, 385, 404

Press, W. H., Rybicki, G. B. & Hewitt, J. N. 1992, ApJ, 385, 416

Press, W. H. & Rybicki, G. B. 1998, ApJ, 507, 108

Rybicki, G. B. & Kleyna, J. T. 1994, ASP Conf. Ser. 69: Reverberation Mapping of the Broad-Line Region in Active Galactic Nuclei, 85

Tukey, J. W. 1958, Ann. Math. Statist, 29, 614.

Chapter 4

VLBA Imaging of Gravitational Lens 0218+357

4.1 Scientific Motivation

Having measured the time delay in gravitational lens 0218+357, we need a model of the mass distribution in the lensing galaxy in order to determine H_o. Most current models of gravitational lenses are constrained by the image positions of the multiply imaged point source, the flux density ratios of those images, and the center of the lensing mass (if this can be determined from high resolution optical images of the lensing galaxy). From this, a model will fit for the gravitational potential of the lensing object projected along the line of sight, $\psi(r, \theta)$. However, most reasonable parametric models of $\psi(r, \theta)$ contain parameters that are not easily constrained by the data mentioned above. This results in large uncertainties for the estimated relation between the time delay and H_o. For example, one of the more simple models of the lensing potential has $\psi(r, \theta)$ depending on radius as a power law function in r

$$\psi(r, \theta) \propto r^{\alpha} f(\theta) \tag{4.1}$$

with $f(\theta)$ included to allow for non-spherical symmetry. In most lens systems even this simple model is very difficult to constrain with the data constraints mentioned above. Just to constrain the value of α for a particular lens, it is usually necessary to observe multiply imaged emission at many different distances from the lensing center. This is usually not the case for lenses in which the only multiply imaged source is a compact (point-like) radio core. In an ideal situation there is extended emission that is multiply lensed to a wide range of distances from the lensing center. Therefore systems that contain Einstein rings or extended arcs have the greatest potential for accurate lens modeling.

This fact was demonstrated convincingly in the modeling of the Einstein ring system MG 1131+0456, (Chen, Kochanek & Hewitt (1995)). Chen et al. produced a model of that lens which predicted the relationship between a time delay between the doubly imaged radio cores and H_o to a formal accuracy of 4%. (This modeling error would be added to the time delay error in quadrature to determine the total error for the H_o measurement.) Chen et al. used an algorithm called LensClean (Kochanek & Narayan, 1992) specifically designed for lenses with a great deal of multiply imaged extended emission. This remains the most accurately modeled lens. Unfortunately no time delay has been measured for this system.

The gravitational lens 0218+357 has a very similar morphology to MG 1131+0456, with a doubly imaged radio core and a full Einstein ring. This indicates that it has the potential to be modeled with similar precision as MG 1131+0456 has been. Additionally, unlike MG 1131+0456, it already has a well determined time delay (Biggs et al., 1999; Cohen et al., 2000). However its small size (the ring has only a $\sim$0.35" diameter) has prevented the detailed mapping of the extended structure of 0218+357. For this reason, no model of this lens exists that is anywhere near as accurate as that for MG 1131+0456.

In order to model accurately the mass distribution of the lensing object in the 0218+357 system, it is necessary to image the lensed emission at much higher resolution than is possible with the VLA. The Einstein ring diameter is about 0.35", and even at 15 GHz, the VLA has a synthesized beam size of roughly 0.15". The VLBA, with its high resolution, is a much more promising choice.

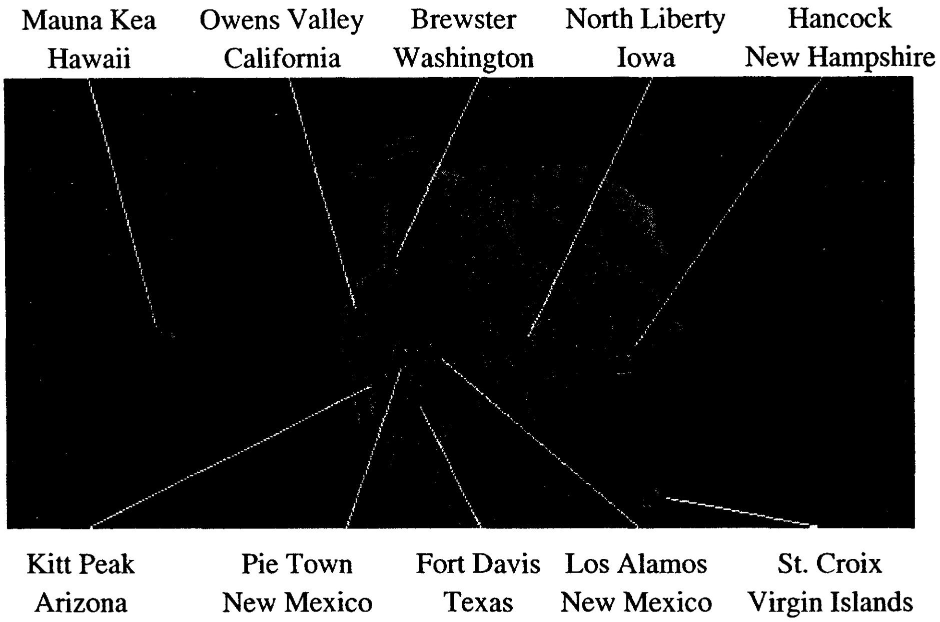

Figure 4-1: Location of each of the ten VLBA antennas.

4.2 Background on the Very Long Baseline Array

The Very Long Baseline Array (VLBA) is an array of radio telescopes designed for extremely high resolution imaging. It consists of ten 25-meter radio dishes, similar to the VLA dishes, but spread out across the continental United States, Hawaii and the island of St. Croix in the Caribbean Sea (Figure 4-1). The longest baselines are up to 8,600 km long, giving the VLBA a resolution of more than 100 times that of the VLA. However, with fewer antennas, the VLBA has lower sensitivity and poorer image fidelity than the VLA.

4.3 Planning the Observations

Resolution, however, is not the only factor that determines what can be imaged. Just as the longest baselines determine the smallest scales in which features can be resolved, the shortest baselines determine the largest scales for which emission can be detected. A baseline of length B will be positively and negatively sensitive to the sky in a striped sinusoidal pattern (see Figure 1-6) of width:

$$\theta = \frac{\lambda}{B}. \tag{4.2}$$

When B is large enough, θ becomes smaller than the feature being observed. In this case, both positive and negative stripes will "cover" the emission feature, causing the total integrated flux density detected by that baseline to be less than the total flux of the emission object as a whole. As B increases so that θ becomes smaller and smaller, the flux density detected will decrease as more and more positive and negative stripes cancel each other out. However, the noise level for the given baseline remains the same. So for very large values of B the flux density detected becomes smaller than the noise level. At this point, the baseline is almost completely insensitive to that feature. So in addition to needing long baselines to define the small scale structure, short baselines are also needed to detect large features.

The largest feature we are interested in is the Einstein ring, which is about 0.35" in diameter. If we let $\theta = 0.35''$ in equation 4.2, then that gives us:

$$B \approx 600,000\,\lambda. \tag{4.3}$$

Baselines much larger than this will be virtually insensitive to the ring. For the VLBA, one must go down to a frequency of 1.4 GHz to get any baselines at all that are smaller than that specified in Equation 4.3. At 330 MHz there are many more baselines of this size or smaller. Therefore, we chose to observe only at these two frequencies.

In addition to having effectively shorter baselines, there are other advantages to observing at low frequency. First, the steep spectrum Einstein ring becomes relatively brighter as compared to the flat spectrum cores, so the side-lobes of the cores cause much less confusion in the image. Second, the radio cores are known to vary at higher frequencies. This is obviously advantageous for time delay measurements, but it is not ideal for lens modeling because the flux ratios of varying components will change in time. Also, with varying components it becomes difficult to combine data from

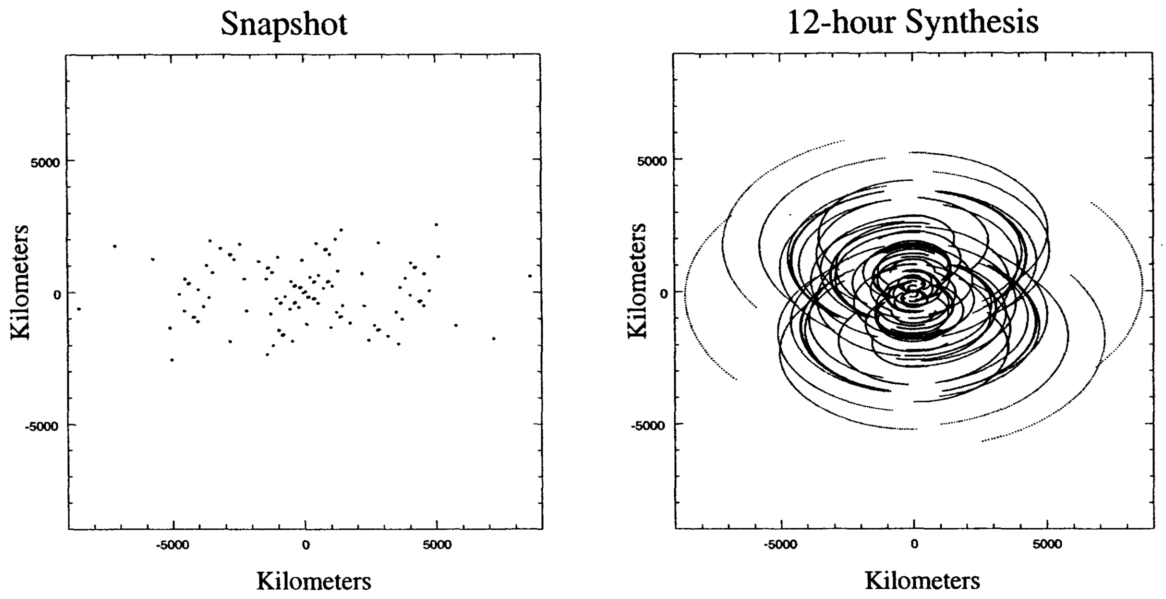

Figure 4-2: UV-coverage of the ten VLBA antennas and one VLA antenna for an object at declination 35°. The left figure shows the UV-coverage of a snapshot image taken when the object is at zenith. The left image shows the UV-coverage for a 12-hour synthesis observation.

different epochs in order to reduce the noise. Finally, there is usually much more extended emission visible at low frequencies, and therefore more potential lensing constraints.

Since short baselines are especially useful for our scientific goals, we decided to include one telescope from the VLA in addition to the ten VLBA antennas. This added to the number of short baselines between telescopes in the Southwest and produced one very short baseline from the VLA to the Pie Town station (see Figure 4-1) which at 50 km is less than half the length of the shortest VLBA baseline. Thus we had 11 telescopes yielding 55 independent baselines for the observation.

Even 55 baselines is not sufficient for high image fidelity, so we take advantage of the fact that as the Earth rotates, the projected baselines slowly change in time. The longer the observation, the more complete the UV-coverage becomes. This is why we chose to observe in 12 hour blocks, essentially from when 0218+357 rises to when it sets, to obtain the maximum UV-coverage. The UV-coverage over this 12 hour period is shown in Figure 4-2.

The reduction of VLBA data is similar to that of VLA data (see Chapter 2) except for adjustments that must be made because the baselines are hundreds of times larger. This means that the atmosphere each antenna "sees" is completely uncorrelated with any other antenna, so the relative phases become more unstable. Also, minute changes in the Earth's rotation rate and orientation which are far too small to affect VLA observations are large enough to affect the VLBA because the resolution is so much greater. Therefore it is impossible to predict precisely the relative group delays at each station that will cause the delay center of the array to coincide with the target source. With such long baselines, these group delays change very rapidly as the Earth turns, and so it is also necessary to solve for the rate of change of these group delays. To accomplish this, we use a form of self-calibration called fringe fitting. Usually this is done by observing known calibrators called fringe finders, which are point-like objects with high brightness. In practice it works very much like the phase calibration for VLA data except that it also solves for the rate of change of the phases. In doing so the total phase gain is calculated which includes not only the deviations in the Earth's orientation, but also the effects of the very different atmosphere at each antenna station. The delays and time derivatives of these delays which were solved by observing a fringe finder are then interpolated to the times when the VLBA was observing the primary target source. The AIPS task FRING was used to solve globally for the delay and rate of change of delay at each antenna. At the resolution of the VLBA, there are no reliable amplitude or phase calibrators. So after applying the solutions from fringe fitting, the rest of the data reduction is accomplished by self-calibration.

We were granted four 12-hour observation times on the VLBA, and chose to do one of them at 1.4 GHz and the other three at 330 MHz. This is because the receivers have a higher system temperature at 330 MHz and therefore we wanted to be able to combine three such data sets to increase the signal to noise ratio at that frequency. For all observations, we used two-bit sampling, channel widths of 0.5 MHz and 16 channels per intermediate frequency (IF). For the 1.4 GHz data we used four IF's for a total bandwidth of 32 MHz. At 330 MHz, radio interference prevented us from using more than three IF's, so the total bandwidth was 24 MHz. While granted 12

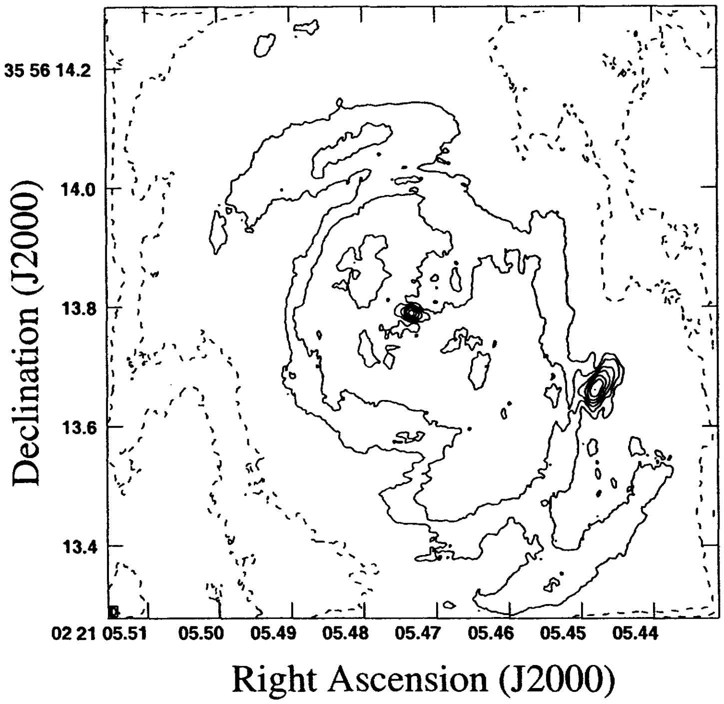

Peak Flux Density = 92.8 mJy/Beam
Contour Levels = 0.8mJy/Beam * (-4, -2, -1, 1, 2, 4, 8, 16, 32, 64, 128, 256, 512, 1024, 2028,...)

Figure 4-3: Initial map of 0218+357 at 1.4 GHz.

hours, we were limited in our data collection to two magnetic tapes per station. That gave us about 10.5 hours of observing time, which we spread out across the 12 hours for the maximum UV-coverage. We also made frequent observations of the fringe finder 3C84. All told, for each 12 hour observation we were able to spend about 9.5 hours of that on the primary source, 0218+357.

4.4 Results from the 1.4 GHz observation

The main imaging challenge at 1.4 GHz is the fact that at this frequency, there are very few baselines that are short enough to detect the large scale extended structure in the ring. After several attempts at imaging and self-calibration, it became clear that there simply was not enough data at these short baseline spacings to define the complicated structure of an object as large as the Einstein Ring in 0218+357. On the other hand, the ring does have at least a few hundred mJy of flux which is detected by a small number of baselines, and so the AIPS task IMAGR will try to put this flux somewhere. This resulted in an image with the two radio cores clearly seen and surrounded by a large blob of extended emission (see Figure 4-3). This blob is not correct, and results from the fact that the flux of the ring is detected, but not detected by enough baselines to define its true structure.

The radio cores show a great deal of extended structure themselves. Each image is extended over a length of about 70 and 100 mas. Since both of these images are lensed images of the same source, their comparative morphology has the potential to add to the model constraints. Therefore, while concluding that producing a detailed image of the ring is impossible at this frequency, we decided to concentrate on producing the best maps possible of the structure in the two radio core images.

With this goal in mind, the fact that we detect flux from the ring is actually a disadvantage because having flux detected but not constrained to an exact position adds noise to the map in general. To solve this problem two things were done. First, the one baseline (from the VLA to Pie Town) that is much shorter than any other and therefore detected much more flux from the ring than any other baseline, was simply removed from the data set. Second, the visibility data were uniformly weighted. This means that in combining the data from all the baselines, each baseline was given a weight such that all regions of the UV-plane would contribute equally. Since the center region of the UV-plane is the most densely sampled, that means that the small baselines, which might pick up some of the flux from the ring will be given weights that are smaller than normal. In this way, uniform weighting decreases the size of the synthesized beam, which causes the response to the extended emission (which is measured in flux per beam) to decrease. Therefore, the diffuse ring should appear fainter in a uniformly weighted image.

The result of removing the smallest baseline and uniform weighting the rest of the baselines was to almost completely remove the ring from the map to the level that it isn't detectable above the noise. Therefore, only the smaller scale features of the image are visible. Both radio core images show intricate and clearly distorted

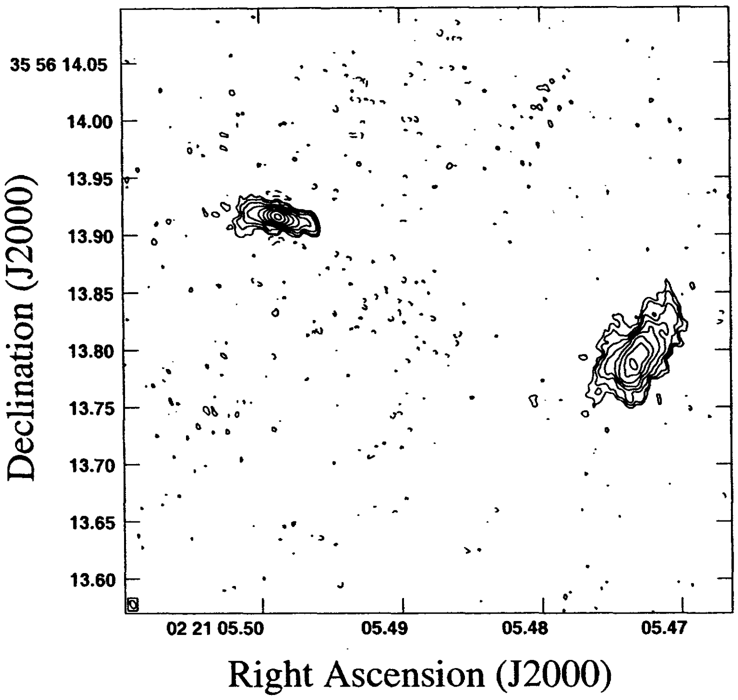

Peak Flux Density = 82.1 mJy/Beam
Contour Levels = 0.25mJy/Beam * (-4, -2, -1, 1, 2, 4, 8, 16, 32, 64, 128, 256, 512, 1024, 2028,...)

Figure 4-4: Final map of 0218+357 at 1.4 GHz. The shortest baseline was removed and the data was uniform weighted. This suppressed the flux from the ring to allow the radio cores to be imaged with much greater sensitivity and detail.

structure, which we hope will provide clues as to how the mass is distributed in the lensing object. The final map is shown if Figure 4-4.

4.5 Results from the 330 MHz observations

At 330 MHz, there are plenty of baselines short enough to define the large scale structure in the ring. However, for many reasons, this is a more difficult frequency at which to observe. The antenna receivers have a system temperature that is about eight times higher than that for 1.4 GHz observations. This results in a lower signal to noise ratio for the observation. This is compounded by the fact that in this part of the radio spectrum there is much more Radio Frequency Interference (RFI) which is interference from radio transmitters on Earth, such as radio stations, TV stations,

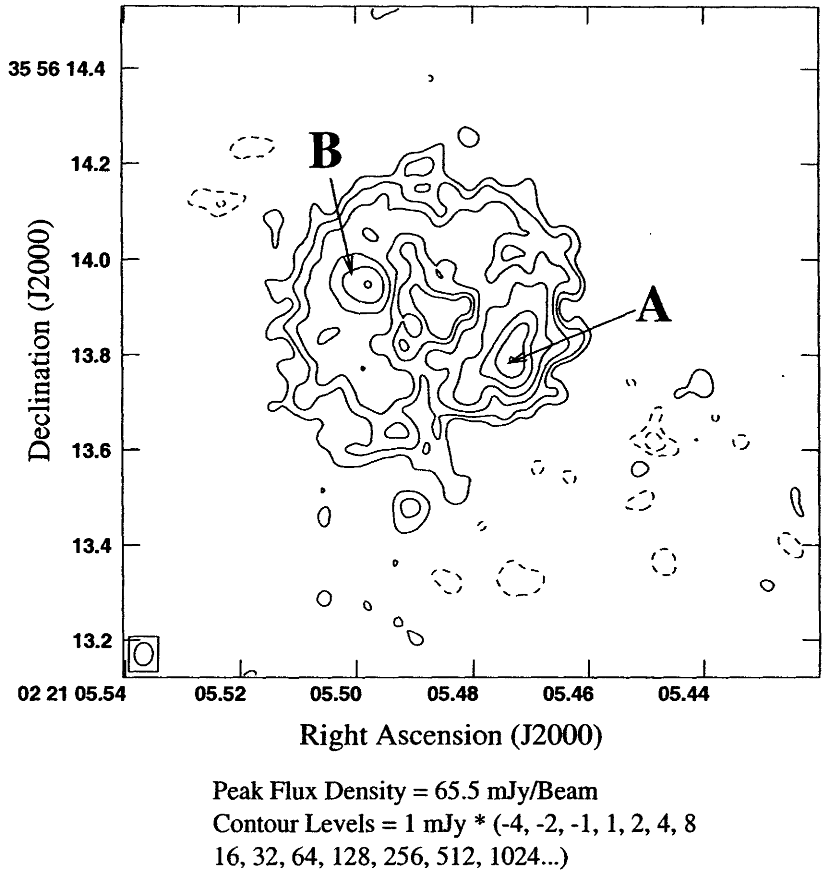

Figure 4-5: Combined map of 0218+357 at 330 MHz. The resolution is 48 by 38 mas.

cellular phones, etc. This restricted the bandwidth to 24 MHz instead of 32 MHz, which also will reduce the signal to noise ratio. Also, the ionospheric distortions (which can be calibrated) change much more rapidly at this frequency.

The first problem encountered in the data reduction was that some RFI was present in the correlated data. The RFI took the form of a single channel differing in flux from the other channels by an amount that was usually well over 10 times the standard deviation for the channels as a whole. Not many channels were affected, but the error from those channels could be significant. The AIPS task FLGIT was used to remove the channels that were suspected of having RFI contamination. All data points that differed from the mean by an amount greater than six times the standard deviation were flagged. It is possible that this removed some outlier points that were not actually affected by RFI, however the total fraction of data points removed was less than 1% so the effect on overall sensitivity from "over-flagging" is negligible.

The fringe finder 3C84 was observed about every 45 minutes. Fringe fitting was only done on 3C84 and the solutions from FRING were interpolated onto the data for 0218+357. The 0218+357 data was then phase-only self calibrated several times until the solutions began to converge. Then amplitude-and-phase self calibration was performed. One problem encountered in the self calibration was that for short solution intervals there often was not a sufficient signal to noise ratio to achieve reliable solutions for the gains. However, at 330 MHz the ionosphere is known to vary on timescales as short as our integration time of two seconds. Ideally a solution interval of two seconds should have been used in the final stages of self calibration. Unfortunately this proved too short to achieve reasonable solutions. One way of dealing with this was to average the three IF's to increase the signal to noise ratio for each time interval. This helped, but the final result was that we could not self calibrate with a solution interval less than about 10 seconds. This most likely removed the major ionospheric distortions, but it is possible that some of the faster ionospheric variations were not successfully calibrated.

Despite the RFI and high system temperatures at this frequency, images were produced from each of the three data sets that clearly show the ring structure. To lower the noise in the images, the UV-data from all three data sets were combined. Then self calibration was repeated on the combined data set. The final image is shown in Figure 4-5 and represents a total of about 28 hours on the source. In this image, the full Einstein ring is clearly visible. It is also apparent that the ring is resolved in the radial direction. Thus there is multiply imaged emission visible at a wide range of distances from the lensing center. For this reason, this image shows excellent potential for lens modeling.

REFERENCES

Biggs, A. D., Browne, I. W. A., Helbig, P., Koopmans, L. V. E., Wilkinson, P. N. & Perley, R. A. 1999, MNRAS, 304, 349

Chen, G. H., Kochanek, C. S. & Hewitt, J. N. 1995, ApJ, 447, 62

Cohen, A. S., Hewitt, J. N., Moore, C. B. & Haarsma, D. B. 2000 (submitted to ApJ)

Kochanek, C. S. & Narayan, R. 1992, ApJ, 401, 461

Chapter 5

The Mass Distribution of the Lens in 0218+357

5.1 Gravitational Lens Modeling

Gravitational lensing occurs when the light from a background source passes through the curved spacetime created by a massive lensing object on its way towards reaching Earth. The curved spacetime in the vicinity of the lensing object will distort the image of the background source as seen from Earth. All we can observe directly is the distorted image. From this it is a complicated mathematical process to determine both the location and morphology of the undistorted image as well as the nature of the mass distribution of the lensing object that could have so distorted its image. In principle, there is never enough information in the distorted image to solve this problem.

This problem can be partially solved if it is known that parts of the distorted image are multiple images of the same source object. If it can be determined for example, that two radio cores seen in the distorted image are in fact two images of a single radio core in the source object, than this immediately produces constraints on the mapping function from the source object to the distorted image. The mapping function is directly related to the mass distribution of the lensing object. The more multiply imaged emission there is, the more constraints can be placed on the nature of how the lensing object is acting to distort the light rays from the original source object.

The only way to exploit the limited information available is by making reasonable assumptions about the lensing object. For example if it is a galaxy, one can make the assumption that it is most dense at its center and that the density falls off monotonically with distance from the galaxy center. One can also exploit the symmetries that are known to exist in most galaxies. Ultimately, one can create a parametric model of the mass distribution of the galaxy. This parametric model is constrained by the data from the multiply imaged regions and can be fit to the data set as a whole.

Once a model of the mass distribution of the lensing object is determined, one can use Equation 1.25 and the measured time delay to determine H_o. The challenge is not only to fit for a model, but also to determine the error and statistical confidence level for that model. In this chapter we seek to use our VLBA observations (presented in Chapter 4) of the gravitational lens 0218+357 to determine the mass distribution of the lensing object to much greater precision than previous attempts at modeling this system. In particular, we wish to exploit the 330 MHz VLBA map (Figure 4-5) which reveals multiply imaged emission over a wide range of positions relative to the lensing center to extract the constraints necessary to accomplish this.

5.2 Previous Modeling of 0218+357

The gravitational lens 0218+357 has been modeled by Biggs, et al. (1999) using the constraints from 15 GHz VLBA observations including the positions of the subcomponents of the cores (A1, A2 and B1, B2) (Patnaik, Porcas & Browne, 1995; hereafter PPB). With these constraints, data sets with Gaussian-distributed errors were produced and they solved for the model parameters by minimizing χ^2. Their best fit model (with a time delay of 10.5 ± 0.4 days which is also derived in that paper and is close to the value we derived in Chapter 3) gives $H_o = 69^{+13}_{-19}$ km/s/Mpc at 95% confidence which is largely dependent on their derived position of the lens center (Figure 5-4).

A recent paper (Lehar et al., 1999; hereafter Lehár) attempted to reproduce the Biggs et al. model. Using the same constraints as did Biggs et al., they found that the position of the lens center was very poorly determined. Lens center positions ranged over a roughly horizontal degenerate region over which the derived H_o value ranged from over 80 to less than 20 km/s/Mpc. Lehár attempted to measure the lens center position with NICMOS images they took (NICMOS1) as well as archival data (NICMOS2) (Figure 5-4). Using these positions however, along with the Biggs et al. time delay, they found H_o to be very low and not well determined at 20 $\pm$20 km/s/Mpc. This is mainly because of the lens center position indicated by the NICMOS data. They concluded that to obtain a well constrained model would require a more accurate determination of the lens center position than currently exists.

Another indication of the lens center could be the centroid of the Einstein ring. This was measured by Patnaik, et al., 1993. However, as pointed out by Biggs et al., if the extended source object that gives rise to the ring is asymmetricly positioned with respect to the caustic, the ring centroid could be offset from the lens center. In fact the Einstein ring shown by Patnaik et al., 1993, in their 5 GHz Merlin map, seems to have a significantly different center from that shown in our 330 MHz VLBA map. This could be due to the fact that the extended source object is shaped differently at each frequency and therefore has different levels of asymmetry with respect to the caustic. If this is the case, it indicates that a ring centroid can vary with frequency and therefore is certainly a poor estimator of the lens center position.

In this chapter, we will attempt to exploit the data from our 330 MHz VLBA observations which show much extended emission including the full Einstein ring to better constrain the position of the lens center and therefore produce a better constrained lens model.

5.3 Quantitative Overview of Lens Modeling

5.3.1 How To Determine H_o

Before proceeding to the method we use to constrain mass models, it is necessary first to review the notation used for quantitative discussions of gravitational lensing. Some of the following is also covered in Chapter 1.

Normally we think of the gravitational potential as a function of position in three dimensional space: $\phi(x, y, z)$. However, the relevant quantity for a thin lens is $\phi(x, y, z)$ integrated over the line of sight at each angular position in the lens plane. This results in a two dimensional "effective" potential defined as follows:

$$\psi(\theta_x, \theta_y) \equiv \frac{2\,D_{LS}}{c^2\,D_{OL}D_{OS}} \int \phi(\theta_x, \theta_y, l)\,dl \tag{5.1}$$

where θ_x and θ_y are angular coordinates in the image plane, l is the coordinate along the axis parallel to the line of sight, and D_{LS}, D_{OL} and D_{OS} are the angular diameter distances from the lens to the source, the observer to the lens and the observer to the source respectively.

It is useful to define a scaled distance in the lens system called the effective distance which we define as:

$$D_{eff} \equiv \frac{D_{OL}D_{OS}}{D_{LS}} \tag{5.2}$$

The angular diameter distance between an object at redshift z_1 and and object at redshift z_2, both along the line of sight, is defined as:

$$D(z_1, z_2) = \frac{c}{H_o}\, f(z_1, z_2) \tag{5.3}$$

where $f(z_1, z_2)$ is given by Equations 1.28 and 1.29. The function $f(z_1, z_2)$ is independent of H_o and depends only on the cosmological model we use (specifically the values of Ω_o and Λ_o). Therefore the effective distance is:

$$D_{eff} = \frac{c}{H_o}\, \frac{f(0, z_L)\, f(0, z_S)}{f(z_L, z_S)} \tag{5.4}$$

Ω_o	Λ_o	$\frac{f(0,z_L)\,f(0,z_S)}{f(z_L,z_S)}$
1	0	1.39
0.25	0.75	1.47
0.25	0	1.50

Table 5.1: The value of $\frac{f(0,z_L)\,f(0,z_S)}{f(z_L,z_S)}$ for several different cosmologies. This assumes that $z_L = 0.685$ and $z_S = 0.96$ as is the case for the gravitational lens 0218+357.

where z_S is the redshift of the source and z_L is the redshift of the lensing object. For the given redshifts, z_L and z_S, the quantity $\frac{f(0,z_L)\,f(0,z_S)}{f(z_L,z_S)}$ depends only on the values of Ω_o and Λ_o in the model we choose. In the case of gravitational lens 0218+357, we already know that $z_L = 0.685$ and $z_S = 0.96$, so we can determine $\frac{f(0,z_L)\,f(0,z_S)}{f(z_L,z_S)}$ for various cosmological models by numerically calculating Equations 1.28 and 1.29. The results for a few reasonable cosmological models are shown in Table 5.1.

It is clear from Table 5.1 that the quantity $\frac{f(0,z_L)\,f(0,z_S)}{f(z_L,z_S)}$ does not change very much depending on the cosmology we assume. There is only an 8% difference between the highest and lowest values here. Therefore, for the rest of this chapter, we will use the value resulting from a cosmology in which $\Omega_o = 1$ and $\Lambda_o = 0$, while keeping in mind the fact that if this cosmological model is incorrect the true value could be up to 8% higher. Thus we have for the case of 0218+357 that:

$$D_{eff} = 1.39\,\frac{c}{H_o}. \tag{5.5}$$

Now if we apply Equation 5.5 and the value $z_L = 0.685$ to Equation 1.24 we get:

$$H_o = \frac{1.17}{\Delta\tau}\left[|\vec{\nabla}\,\psi(\vec{\theta_A})|^2 - |\vec{\nabla}\,\psi(\vec{\theta_B})|^2 - 2\,\psi(\vec{\theta_A}) + 2\,\psi(\vec{\theta_B})\right] \tag{5.6}$$

where $\Delta\tau$ is the time delay. In Chapters 2 and 3 we measured $\Delta\tau$ for this system. In this chapter, with the data from Chapter 4, we will try to constrain the function $\psi(\vec{\theta})$ and thus complete the measurement of H_o.

5.3.2 Parametric Mass Models of the Lens

Before applying a lens modeling algorithm to the 330 MHz VLBA data to determine $\psi(\vec{\theta})$, we first need a reasonable parametric model for $\psi(\vec{\theta})$.

Let us start with a very simple case in which the lensing mass is a singular isothermal sphere (SIS). Physically, a SIS is the mass distribution of a gas cloud of uniform temperature which is held together by its own gravity. In this case, the mass within any given radius, $M(r)$, is directly proportional to r. It is thought that the mass distribution of a typical frontier galaxy is roughly that of a SIS out to the very edges of the luminous part of the galaxy. For a SIS, the parametric mass model is:

$$\psi(\vec{\theta}) = b\,|\vec{\theta}| \tag{5.7}$$

where b is a constant value measured in angular units and $\vec{\theta}$ is measured from the angular position of the center of the lensing mass. If we let σ equal the one dimensional velocity dispersion in the SIS then we can relate b to the physical qualities of the lens as follows:

$$b = 4\pi \frac{\sigma^2}{c^2} \frac{D_{LS}}{D_{OS}} \tag{5.8}$$

The quantity b is also significant in that it is the critical radius of the gravitational lens. This means that a source object will be multiply imaged only if it is separated from center of the lens by less than the angle b.

Of course we can make the model more general by not assuming that the potential falls off exactly as it does for a SIS. With an SIS, $M(r) \propto r$ and this can be generalized by adding a new parameter α so that $M(r) \propto r^{\alpha}$, where for a SIS, α would be 1. Allowing α to vary allows us to test a variety of mass falloff rates. The mass model in this case is:

$$\psi(\vec{\theta}) = \frac{b^{2-\alpha}}{\alpha}\,|\vec{\theta}|^{\alpha} \tag{5.9}$$

This model can be further generalized by not requiring the potential to be spherically symmetric, but allowing an elliptical mass distribution.

To first order this results in the following mass model:

$$\psi(\vec{\theta}) = \frac{b^{2-\alpha}}{\alpha} |\vec{\theta}|^{\alpha} \left(1 + \gamma \cos 2(\theta - \theta_\gamma)\right) \tag{5.10}$$

This adds two additional parameters: γ, which represents the magnitude of the ellipticity and θ_γ, which is the angle of the ellipticity. Overall, the model now has four free parameters: b, α, γ and θ_γ. There is no end to how general we can make the model, and therefore no limit to the number of independent parameters it can contain. There is, however, a limit to the data at hand to constrain such a model. The model should be general enough to reasonably approximate the mass distribution in a real galaxy (although this is not presently well known) but not so general that there are too many parameters to be well constrained by the available data.

5.4 LensClean

5.4.1 Basic Concept of LensClean

One very powerful lens modeling technique was developed by C. S. Kochanek and R. Narayan and is called LensClean (Kochanek & Narayan, 1992). The basic strategy of LensClean is first to assume a trial mass model for the lens. That mass model determines a mapping function between the source plane and the image plane. For some regions of the source plane, the mapping function will map points to more than one location in the image plane. This is defined as the multiple image region of the source plane. Therefore for any given point in the image plane, there could be one or more other points in the image plane that share a common inverse mapping point in the source plane. With LensClean, the normal CLEAN algorithm for deconvolving the synthesized beam from an interferometer image is adjusted to take multiple imaging into account. This algorithm was later generalized to work directly from the visibility data in what is sometimes referred to as "visibility LensClean" (Ellithorpe, Kochanek and Hewitt, 1996). This is the version of LensClean we apply.

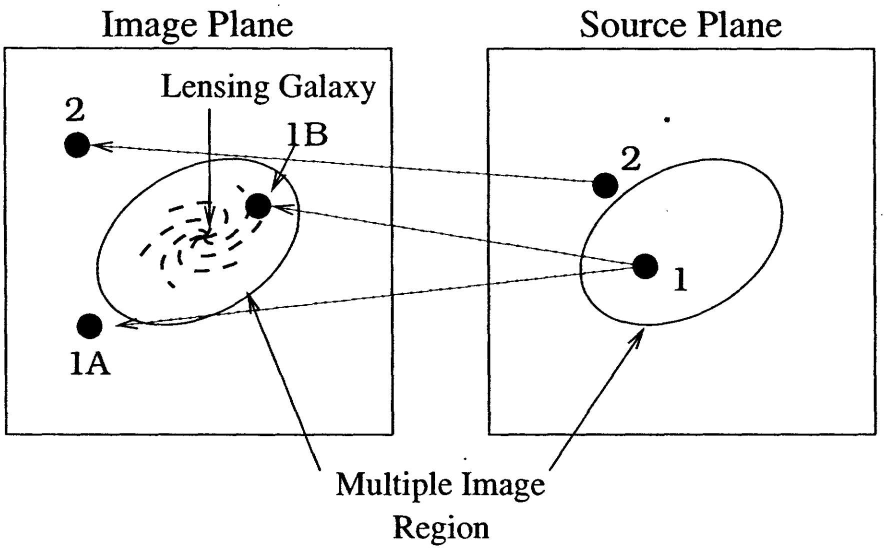

Figure 5-1: The lensing mass caused each point in the source plane to appear at a different apparent location in the image plane (see point 2). In the case of strong lensing, there is a region surrounding the line of sight to the lensing mass which is multiply imaged. Points here appear in more than one location in the image plane (see point 1). LensClean is a modification of the CLEAN algorithm which takes into account the fact that some points in the image (see points 1A and 1B in the image plane) are from the same source point. If flux is cleaned from the point 1A, it must also be cleaned from 1B at the same time.

5.4.2 Review of the CLEAN Algorithm

With normal CLEAN, the first step is to identify the point in the image with the highest flux density. At that location, the dirty beam with peak flux density equal to some small fraction (usually 0.03 to 0.15) of the flux density at that point is subtracted. CLEAN then moves on to the location of the peak flux density in the resulting image. This continues until the absolute peak flux density of the residual image is lower than some value determined beforehand (usually this value is two or three times the expected RMS noise in the final image). At that point, most of the flux in the image has been removed. But CLEAN has in the process created a point-source model of the image based on the points at which it subtracted the dirty beam and how much flux was subtracted at each of these points. This point-source model is then convolved with a CLEAN beam which is a two-dimensional Gaussian with the same dimensions as the primary peak in the dirty beam. Therefore the flux is replaced in the form of Gaussians to restore the proper image resolution, but without restoring the sidelobes of the dirty beam. Over time there have been improvements made to both the efficiency and stability of the CLEAN algorithm (see Högbom (1974), Schwarz (1978), Clark (1980) and Cornwell (1983)). However, the core idea of CLEAN remains the same.

5.4.3 Overview of LensClean

LensClean adjusts the CLEAN algorithm to take into account the effects of the distortions due to the lens. While CLEAN deals with one point source at a time, LensClean also checks to see if (based on the trial mass model) each point is the image of a point in the source plane that is multiply imaged. If so, the dirty beam will be subtracted from all points in the image plane to which this source point is mapped. In addition to identifying where these points are in the image plane, the trial mass model also determines the relative magnifications at each of these points, so the algorithm can subtract the dirty beams with the correct flux density ratio from each of these points. LensClean chooses the location of successive clean component so as to maximally reduce the root-mean-square noise in the residual image. As with CLEAN, LensClean continues this process until some previously specified stopping criteria is reached. Typical stopping criteria are a maximum number of clean components or a minimum value for the peak flux in the residual map. At this point, a point-source model of the image is produced. The trial mass model can then be evaluated based on how well that point-source model fits the original *uv* data. Clearly a trial mass model much different from the actual mass distribution in the lens will cause LensClean to remove flux from the wrong points in the map, causing the final point-source model to be a poor fit to the original *uv* data. For a parametric mass model, all the free parameters can be fitted so as to produce, from LensCleaning, the point-source model that best matches the original *uv* data. The average deviation of the real *uv* data from that expected from a given point-source model, given in units of the expected RMS noise per visibility, is used as the measure of the goodness of the fit, which we use as our χ^2 statistic. If N_{vis} is the number of visibilities, V_i is the complex value of the ith visibility, σ_V is the average noise per visibility and V_i^m is the predicted value of the ith visibility based on the clean component model then we have:

$$\chi^2 = \sum_{i=1}^{N_{vis}} \frac{|V_i - V_i^m|^2}{\sigma_v^2} \tag{5.11}$$

LensClean determines the model parameters for the lensing mass by fitting them so as to minimize χ^2.

One great advantage of this method is that LensClean works directly with the *uv* data, rather than taking as input an image, which may have deconvolution errors. Of course LensClean does perform deconvolution from the *uv* data, but the resulting image is never used. All that is used is the point-source model obtained from the deconvolution process. This is then directly compared to the original *uv* data to measure the goodness of fit for the trial model used.

5.5 Applying LensClean to 0218+357

The original *uv* data set for the 330 MHz VLBA data contained over 2 million visibilities at 3 different IF's. LensClean is a very computationally intensive algorithm in that the deconvolution must be done many times to find best fit values. With a data set this large, a single deconvolution with LensClean takes nearly a full day on a Sun Ultra 1 workstation, thus making its use highly impractical. One way we chose to reduce computation time was to average this data in time from 2 seconds to 90 seconds integration times. This was the maximum value that would still provide sufficient field of view. The three IF's were also averaged together. This greatly reduced the size of the data set and reduced the computation times by a similar factor.

With LensClean we hope to use the structure of the Einstein Ring as well as other extended emission in 0218+357 to constrain a mass model. However, the 330 MHz VLBA image has a resolution which is too high to be useful given the map noise. Therefore we restricted the *uv* data to only those baselines which are shorter than 2 million wavelengths. This removed approximately half the data leaving 25,215 visibilities. This dramatically improved the speed of the LensClean algorithm not only by reducing the size of the data set, but also by increasing the size of the synthesized beam which allowed deconvolution with far fewer iterations. By removing the long baselines, the synthesized beam went from 23 by 32 mas to 69 by 73 mas, a factor of almost seven increase in area.

5.5.1 Finding the Center of the Lensing Mass

For any given mass model, such as those of Equations 5.7, 5.9 and 5.10, the effective potential $\psi(\vec{\theta})$ is a function of the variable $\vec{\theta}$ which is measured with respect to the central position of the lensing mass. Therefore, knowing the location of the center of the lensing mass is crucial for lens modeling. This can sometimes be determined empirically with high resolution optical images, but in the case of 0218+357, the angular size of the lens is too small to isolate the lens position to the roughly 0.01″ accuracy needed for this lens. Therefore, we must use LensClean to constrain the location of the lens center.

We apply a singular isothermal ellipsoid (an SIE) as a mass model. An SIE is a mass distribution which is a SIS with critical radius b, but stretched so that is has a sheer of γ at the angle θ_γ measured east of north. For this mass model there is a rather simple relation between H_o and the time delay, $\Delta\tau$:

$$H_o = \frac{1+z_L}{\Delta\tau}\,\frac{f(0,z_L)\,f(0,z_S)}{f(z_L,z_S)}\,\frac{1}{2}\left(|\vec{\theta_A}-\vec{\theta_c}|^2-|\vec{\theta_B}-\vec{\theta_c}|^2\right) \tag{5.12}$$

(Witt, Mao & Keeton, 2000; adjusted for notation). Here $\vec{\theta_c}$ is the position of the lens center, $\vec{\theta_A}$ and $\vec{\theta_B}$ are the positions of the A and B images respectively and $f(z_1,z_2)$ is the normalized angular diameter distance between redshifts z_1 and z_2 as defined in Equations 1.28 and 1.29. Notice that H_o depends only on the lens center position and not on the other mass model parameters.

In principle we would use the SIE mass model and fit all five parameters (b, γ, θ_γ, x_{center} and y_{center}) using LensClean so as to minimize the goodness of fit parameter χ^2. This would tell us the most likely position for the lens center which, along with

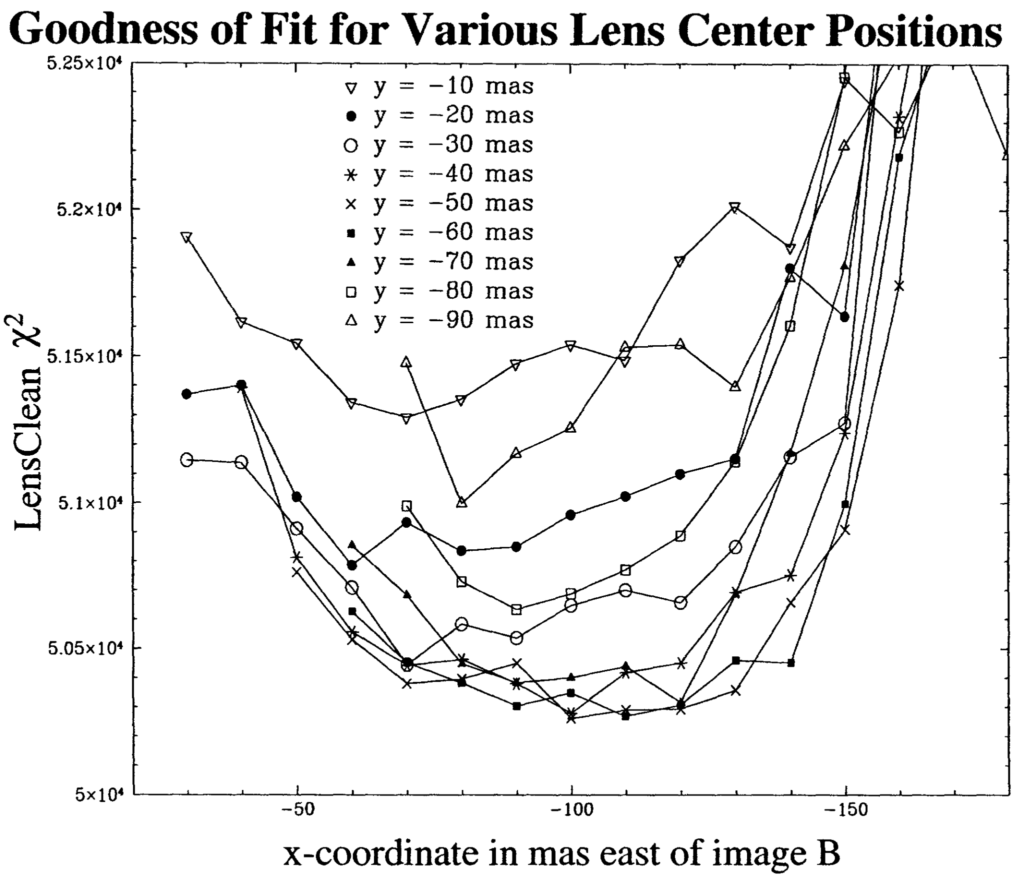

Figure 5-2: The LensClean χ^2 values as a function of the lens center position, (x, y), measured relative to the B image. At each location, the parameters other model parameters b, γ and θ_γ were fit with LensClean. The minimum value is χ^2 = 50,260 at (x, y) = (-100, -50) mas.

the time delay, determines H_o. However, through experience, we learned that the χ^2 surface is very poorly behaved due to systematics as the x and y coordinates of the lens center are varied. This prevented us from directly fitting these parameters. What we did instead was to choose trial values of x_{center} and y_{center} and fit for b, γ and θ_γ at that trial lens center position. The χ^2 value for the best fitting model was thus calculated as a function of the lens center position.

At each trial lens center position, we began the fitting of the other three mass model parameters, b, γ and θ_γ, with their values calculated using other data as modeling constraints. The three constraints we used were: two from the relative positions of the radio cores as measured with the VLBA at 15 GHz to sub-milliarcsecond accuracy by Patnaik, Porcas & Browne, 1995 and one from the flux ratio of the radio cores as measured in Chapter 3 of this thesis. From this initial guess, LensClean was allowed to fit these parameters based only on the data from our 330 MHz VLBA data. We used as stopping criteria for the image deconvolution a limit of 10,000 clean components. This minimization was performed over a large grid of trial lens center positions with a periodic spacing of 10 mas. The results are shown in Figure 5-2.

It is apparent from the data in Figure 5-2 that there is a clear minimum in the χ^2 surface. The region surrounding the χ^2 minimum is relatively flat but increases steeply at its edges. The minimum value χ^2 is 50,260 and occurs at a lens center position of (x_{center}, y_{center}) = (-100 mas, -50 mas) relative to the B component. Assuming a time delay of 10.1 days and a cosmology with $(\Omega_o, \Lambda_o) = (1,0)$, this lens center position corresponds to $H_o = 37$ km/s/Mpc. The other lens parameters for this best fitting model are: $b = 180$ mas, $\gamma = 0.11$, $\theta_\gamma = -48.2^o$.

The best fitting value we obtain for γ of 0.11 is rather high and indicates a potential ellipticity (1 - b/a) of 0.2 and a mass ellipticity of 0.55 (or more depending on the orientation angle). The orientation of the ellipticity is more than 60^o from the line joining the two core images. The lens galaxy is quite difficult to observe at a redshift of 0.685, and Lehár stated that they were unable to fit for an ellipticity in the light distribution based on their HST images. Nevertheless, the fact that the galaxy image would appear roughly circular for an ellipticity as large as 0.55 is difficult to imagine.

Before this final run of LensClean we also experimented with CLEANing much less deeply than 10,000 clean component by: a) using only 2,000 and 5,000 clean components in the deconvolution and b) by including the longer baselines which resulted in a smaller beam size and therefore a less deep CLEAN. The result was a lens center that was even farther away from the B image and therefore resulted in an ever lower H_o estimate. However, the residual maps for the best fitting models in each of these cases showed residuals much higher than the map noise, indicating that by not CLEANing deeply enough, systematic errors were introduced. Therefore we judge the results from the 10,000 clean component run to be much more reliable. We could have used even more than 10,000 clean components. However this would have increase the computation time, and since the residuals for the 10,000 clean component

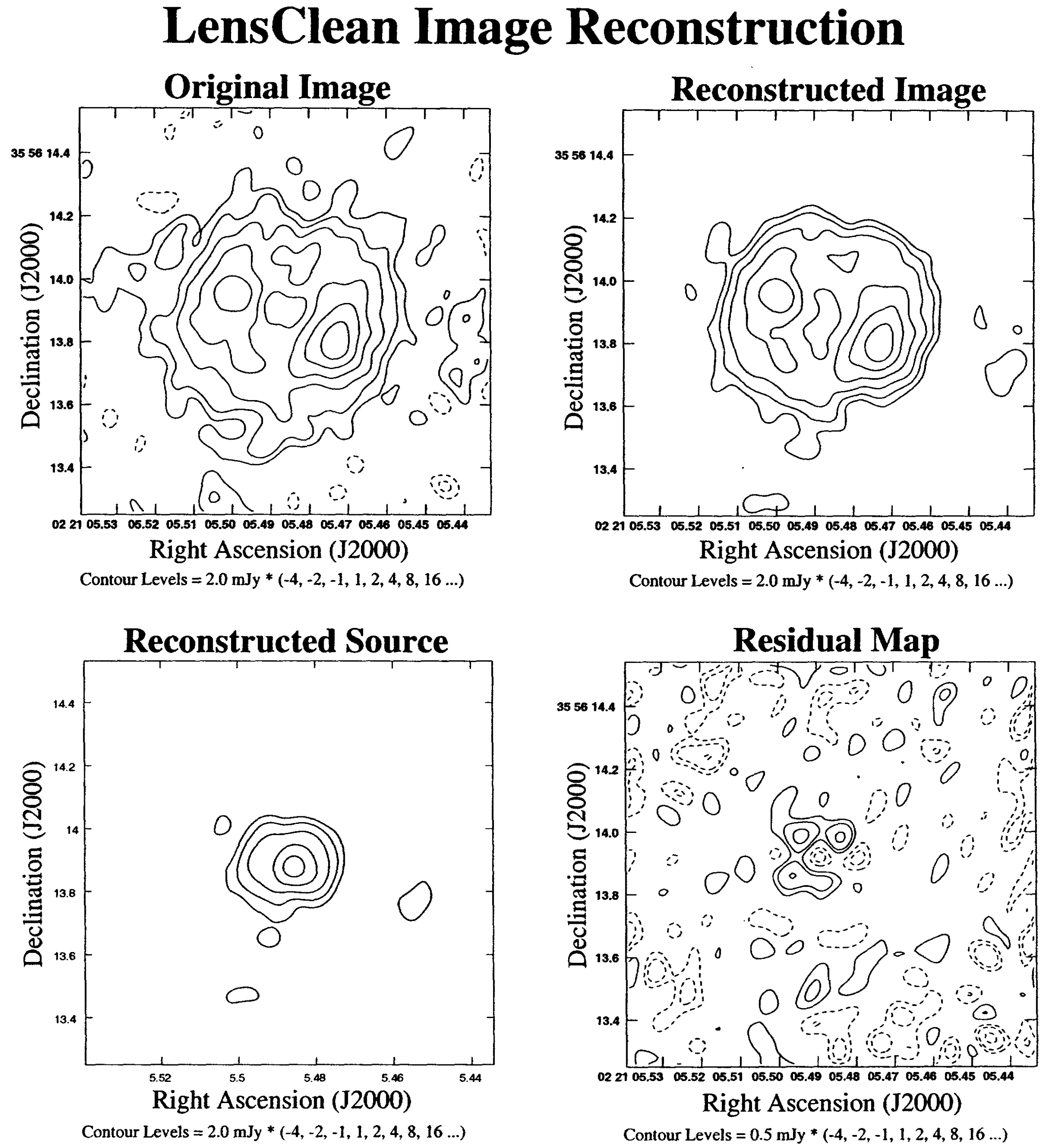

Figure 5-3: Maps for the various outputs of LensClean compared to the original observed map. In each map a 75 by 75 mas restoring beam was used to provide easier comparisons. Note that the contours are lower for the residual map. The peak of the residual map is only 2.5% that of the observed image.

case are already very close to the map noise (see Figure 5-3), it is unlikely that there would be any improvement.

In order to determine how good a fit our χ^2 values are, it is necessary to compare them to the number of degrees of freedom, N_{dof} in the model. We apply a formula used by Ellithorpe et al. (1996) to estimate the total number of degrees of freedom:

$$N_{dof} = 2\,N_{vis} - 3\,N_{grid} - N_{parm} - 2\,N_{gain} \tag{5.13}$$

where N_{vis} is the number of visibilities, N_{grid} is the number of grid points for the clean components, N_{parm} is the number of parameters in the mass model and N_{gain} is the number of gain parameters used in the data calibration. The values N_{vis} and N_{gain} are multiplied by two because they are complex numbers. N_{grid} is multiplied by three because each grid point contains three free parameters: its x and y coordinates and the total flux at that point. For our model, we have N_{vis} = 25,215, N_{grid} = 16,384, N_{parm} = 5 and N_{gain} = 60 which results in N_{dof} = 1,153. Thus our best fit model has a χ^2 value that is far from the theoretical optimum fit. One might argue that a more appropriate formula for the number of degrees of freedom is

$$N_{dof} = 2\,N_{vis} - N_{grid} - N_{parm} - 2\,N_{gain} \tag{5.14}$$

since the (x, y) coordinates are not free to vary. This would give N_{dof} = 33,921, still much smaller than our minimum χ^2. However, only a 20% underestimate of the of our measurement errors would account for the difference in the minimum value of the χ^2 and the number of degrees of freedom. As we discuss below, the technique we choose to determine confidence intervals does not depend on the value of N_{dof}, so we do not discuss this further here. See Ellithorpe, Kochanek and Hewitt (1996) for some discussion of this issue.

With the χ^2 surface mapped out in the $x - y$ plane, we would like to measure the uncertainties in our best fitting lens center position. Formally, the 68% confidence region (1σ region) is determined by the set of points for which $\chi^2 - \chi^2_{min} = \Delta\chi^2 \leq 1$. Figure 5-2 clearly shows that the noise level in the χ^2 surface is much greater than 1, (probably due to systematic errors) so this method is not feasible. Instead we estimate the noise in the χ^2 surface as the root mean square of the differences between adjacent points in the sample grid. Restricting this measurement to the relatively flat base of the χ^2 well, we calculate the average variation to be 99. Adding this to 1, we conclude that points for which $\Delta\chi^2 \geq 100$ are eliminated as being the lens center position at the 68% confidence level. The 1σ region is then the set of points for which $\Delta\chi^2 \leq 100$. We define $\Delta\chi^2$ for the 2σ region as twice the noise, 198, plus 4 or $\Delta\chi^2 \leq 202$. Similarly the 4σ region is defined by $\Delta\chi^2 \leq 408$. This allows us to define confidence regions in the image plane for the position of the lens center (see Figure 5-4).

This allows us to set confidence limits on H_o as well. With a time delay uncertainty from Chapter 3 of about 8% (68% confidence), we can conclude that $H_o = 37^{+12}_{-20}$ km/s/Mpc at 68% confidence. At 95% confidence we conclude that H_o is between 9 and 68 km/s/Mpc.

5.6 Discussion of Results

It is clear that the combination of these data and LensClean are unable to constrain usefully the lower limit on H_o. However, given the current range of H_o estimates, the upper limit of 68 km/s/Mpc at 95% confidence is a rather interesting result. It indicates an H_o that is on the low end of current measurements which range from about 60 to over 80 km/s/Mpc.

The 1σ region we determine for the position of the lens center does overlap that calculated by Lehár which is based on high resolution VLBA maps of the cores by PPB. However, the lens center in the Biggs et al. (1999) model as well as the position of the ring centroid calculated from 5 GHz data are both ruled out by our model at greater than 4σ confidence. The two NICMOS estimates of the galaxy center by Lehár are similarly ruled out, but the average of the two (which was used by Lehár for their model) does fall within our 2σ region. Not surprisingly both our model and Lehár's model give extraordinarily low most-likely values for H_o.

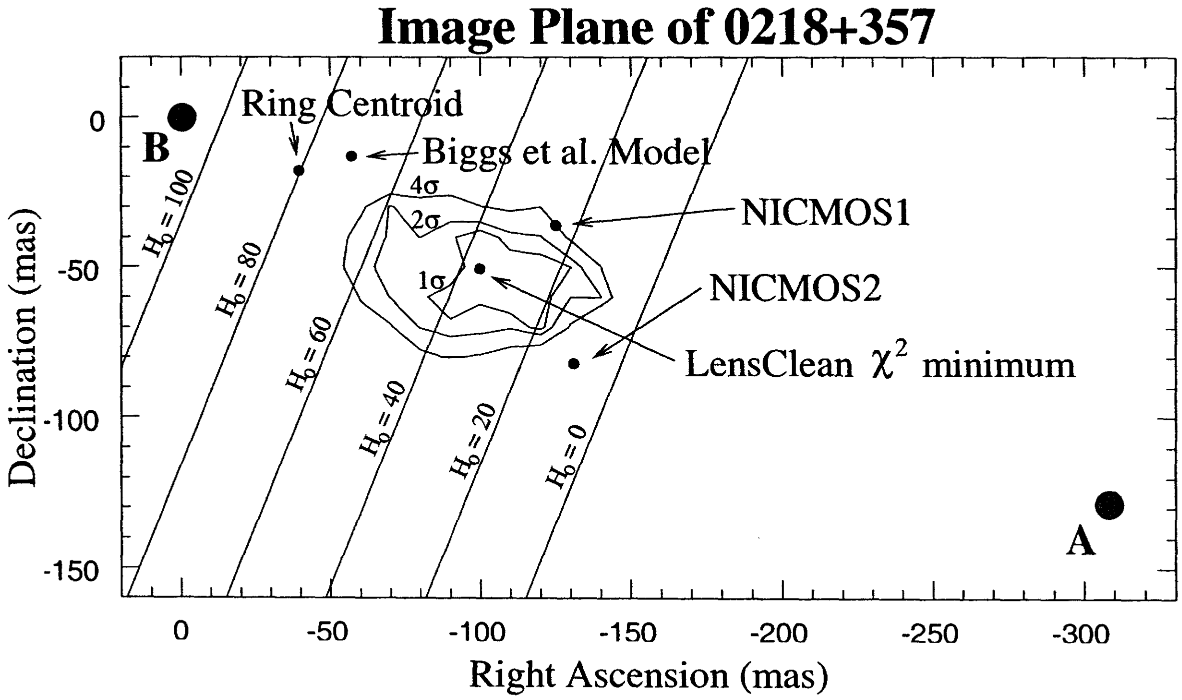

Figure 5-4: The image plane of the gravitational lens 0218+357. Here we measured χ^2 as a function of lens center position and plot the χ^2 minimum and the 1σ, 2σ and 4σ confidence regions. Also shown are the lens center positions indicated by: the ring centroid (Patnaik, Porcas & Browne, 1995), the Biggs et al. model (Biggs, et al. (1999)), the "NICMOS1" and "NICMOS2" images (Lehar et al., 1999). If we assume a SIE mass model then, for a given cosmology and time delay, H_o is a function of the lens center position. We plot H_o contours in units of km/s/Mpc for a time delay of 10.1 days and a cosmology with $(\Omega_o, \Lambda_o) = (1,0)$. The positions of the A and B radio core images are also shown.

5.7 Comparison with Existing Data

In using the Einstein ring in this system as our primary lensing constraint, we are using nearly independent data as has been used in previous modeling efforts based on the small scale morphology of each image core. It is therefore of interest to determine the consistency of our best fitting model with data other than the Einstein ring.

In particular, PPB measures the vector between the double cores in each component (A1-A2 and B1-B2). These data have been used for modeling by Biggs et al. (1999) and Lehár. Lehár defines a region in the image plane in which the lens center can be and still be consistent with the PPB data. The best fitting model we derive based on the 330 MHz VLBA data does not fall within this region, and therefore it is not consistent with the data from PPB. However there is overlap between our 2σ confidence region (Figure 5-4) and Lehár's region. We estimate the region that is consistent with both data sets at the 95% confidence level to be the intersection of our 2σ region with the Lehár region defined by $\Delta\chi^2 \leq 10^{1/2}$. This intersection region (along with the uncertainty in the time delay measurement) restricts H_o to between 12 and 50 km/s/Mpc at 95% confidence.

The fact that our confidence region overlaps that of Lehár shows that there is a set of models that is consistent with two very different sets of data. One data set is our 330 MHz VLBA observation of the Einstein ring. The other is the sub-milliarcsecond resolution images of the double cores by PPB with the VLBA at 15 GHz. We wish to compare our lens models to a third data set, our 1.4 GHz VLBA image (Figure 4-4). That image has one tenth the resolution of the PPB image, so the double cores are not resolved. However, extended emission appears at 1.4 GHz that is not seen (or more likely is resolved out) at 15 GHz. Unlike the 330 MHz image, the extended emission is only seen in the vicinity of the cores, so the information in the Einstein ring is unavailable. We test the consistency of the 1.4 GHz data and a lens model by mapping the image of both the A and B components back into the source plane according to that model. If the model is consistent with the data, the pre-images of A and B should have the same morphology. In Figure 5-5 we show the original A and B images along with their pre-images determined according to two models. One model (Model 1) is the best fitting model determined with LensClean as discussed previously. The other model (Model 2) is chosen so that the lens center of that model lies near the center of the intersection of our region of allowable lens centers and that of Lehár. The parameters of Model 2 are: $x_{center} = -120$ mas, $y_{center} = -40$ mas, $b = 183$ mas, $\gamma = 0.13$ and $\theta_\gamma = 81.4^o$. Model 1 actually lies outside the region determined by Lehár. The result is that the pre-images for Model 1 seem to have somewhat different morphologies, indicating that Model 1 is not consistent with these data. This is not surprising since Model 1 is not consistent with the PPB data. The pre-images of Model 2 are very similar in morphology and in particular have nearly identical ellipticity angles. It is encouraging that a model determined mainly by the Einstein ring and from a data set in which structure of each radio core is not resolved produces a lens model with the right strength and internal sheer to cause the drastically different A and B morphologies from the 1.4 GHz data to map back to virtually the same morphology in the source plane. We conclude that models in the intersection region are consistent with all three data sets.

5.7.1 Future Work

The mass model of the gravitational lens 0218+357 can be improved in two major ways. One is to refine the lens modeling technique. Perhaps more important than this is to obtain data of higher quality. Here we discuss both of these possibilities.

One way to improve the modeling is to make the mass model more general. This can be done by adding more parameters such as an exponent α to the radial dependence of the effective potential, allowing for an external sheer or allowing for a core radius. It must be emphasized that for each extra dimension that must be minimized the computational time increases *very* rapidly. However one must recognize the possibility that assuming a SIE mass distribution could have biased the results if the true mass distribution is very different from this. For example, with an effective potential dependent on radius as $\psi(r) \propto r^\alpha$ the time delay changes by a factor of roughly $(2-\alpha)$ (Witt, Mao & Keeton, 2000). Romanowsky et al. (1997) shows plots of line-of-sight

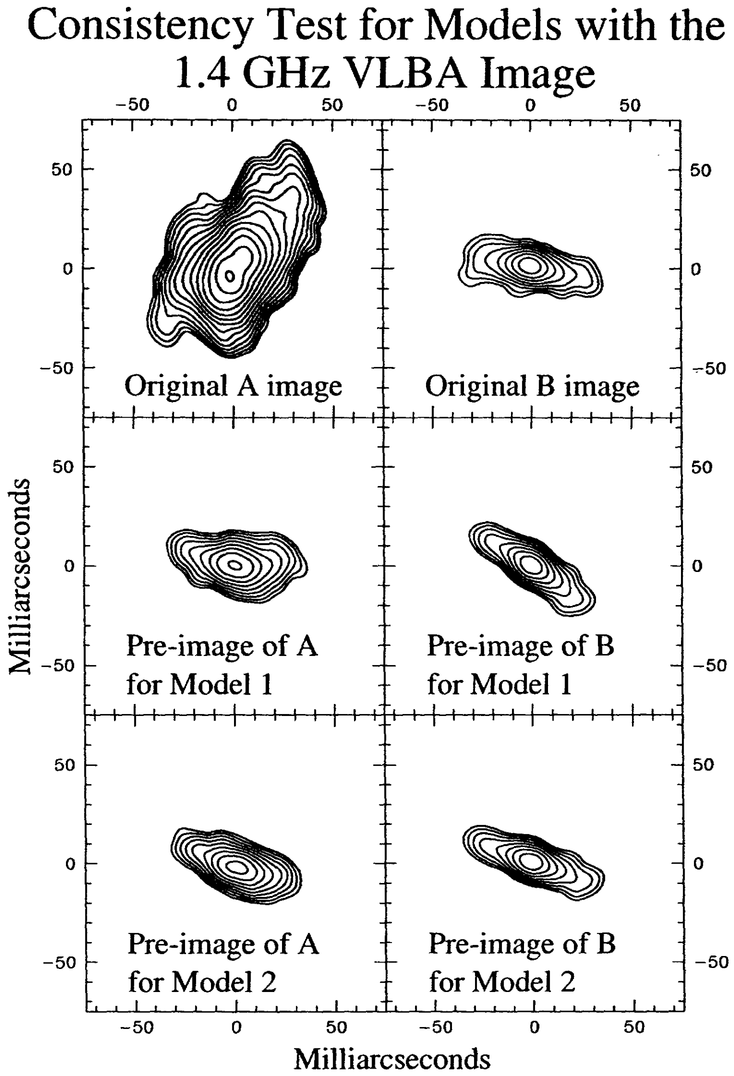

Figure 5-5: Comparison of morphologies of the A and B image in the 1.4 GHz VLBA map of 0218+357 and their pre-images in the source plane according to two different models.

velocities as a function of radius for galaxies NGC 7619 and NGC 1439. From the data in these plots, we estimate that these galaxies both have $\alpha = 0.7$. Similarly, modeling the gravitational lens MG1131+0456, in which the ring is resolved in the radial direction gives $\alpha = 0.6 \pm 0.2$. On the other hand, the gravitational lens models of MG1654+1346 gives $\alpha = 1.15 \pm 0.01$ (Ellithorpe, Kochanek and Hewitt, 1996). Clearly our inability to constrain α in 0218+357 is a major source of uncertainty in our determination of H_o. Adding an external sheer of γ would change the time delay by roughly factor of $(1 - \gamma \cos 2\theta)$ where θ is the angle between the sheer and the component separation. The region around 0218+357 was explored optically by Lehár to estimate the external sheer. They found that the lensing galaxy was unusually isolated, and any external sheer was likely to be at the 1% level.

As for the determination of the errors, rather than assuming that the 1σ error bars would extend to parameter values which produced a $\Delta\chi^2$ less than a given value, the best way to determine the errors is through Monte Carlo simulations. However, to achieve reasonable results through Monte Carlo simulations, it is necessary to perform at least several hundred samples, each of which done in the same method as the real data. Therefore, Monte Carlo simulations necessarily take at least several hundred times the computing time as the original measurement. This obviously was not a practical option for contemporary computers.

As for the data we used, there are two major areas which could be improved. These are the *uv* coverage and the sensitivity of the images. We used only the VLBA baselines plus a singe VLA antenna which gave only 55 independent baselines. Adding data from MERLIN and the entire VLA would greatly increase the *uv* coverage near the center of the *uv* plane. This would greatly expand the dynamic range of baseline lengths, producing images of higher image fidelity. Additionally this would make the extended features we are interested in visible at higher frequencies. This will help our second goal of higher sensitivity not only by increasing the amount of data, but also because at higher frequencies the receivers are many factors more sensitive.

REFERENCES

Biggs, A. D., Browne, I. W. A., Helbig, P., Koopmans, L. V. E., Wilkinson, P. N. & Perley, R. A. 1999, MNRAS, 304, 349

Chen, G. H., Kochanek, C. S. & Hewitt, J. N. 1995, ApJ, 447, 62

Clark, B. G. 1980, A&A, 89, 377

Cornwell, T. J. 1983, A&A, 121, 281

Dyer, C. C. & Roeder, R. C. 1972, ApJ, 174, L115

Ellithorpe, J. D., Kochanek, C. S. and Hewitt, J. N. 1996, ApJ, 464, 556

Fukugita, M., Futamase, T., Kasai, M. & Turner, E. L. 1992, ApJ, 393, 3

Högbom, J. A. 1974, A&AS, 15, 417

Kochanek, C. S. & Narayan, R. 1992, ApJ, 401, 461

Lehar, J., Falco, E., Kochanek, C., McLeod, B., Munoz, J., Impey, C., Rix, H-W., Keeton, C., Peng, C. 1999, Preprint: astro-ph/9909072, accepted to ApJ(Lehár)

Patnaik, A. R., Browne, I. W. A., King, L. J., Muxlow, T. W. B., Walsh, D. and Wilkinson, P. N. 1993, MNRAS, 261, 435

Patnaik, A. R., Porcas, R. W. & Browne, I. W. A. 1995, MNRAS, 274, L5 (PPB)

Romanowsky, A. J. and Kochanek, C. S. 1997, MNRAS, 287, 35

Schwarz, U. J. 1978, A&A, 65, 345

Witt, H. J., Mao, S. & Keeton, C. R. 2000, Preprint: astro-ph/0004069, submitted to ApJ

Chapter 6

Conclusion

6.1 Implications for Cosmology

By measuring light curves for the gravitational lens 0218+357, we were able to determine its time delay to be $10.1^{+1.5}_{-1.6}$ days at 95% confidence. With further VLBA observations of this system, we were able to put constraints on the lensing mass. Together, we determine that $H_o = 37$ km/s/Mpc with a 95% confidence interval of 9 to 68 km/s/Mpc. With our measurement of H_o, it is useful to discuss what this implies for cosmology and how this result fits into current work being done in the field of observational cosmology.

6.1.1 Age of the Universe

Knowing the cosmological model (i.e. the parameters Ω_o and Λ_o) as well as H_o allows a direct calculation of the age of the universe. The quantities Ω_o and Λ_o determine how the expansion rate of the universe changes over time. Combined with knowledge of the current expansion rate, H_o, the scale factor can be determined at all times in the past back to the time when it was zero. The time in the past at which the scale factor was zero is defined as the beginning of the universe.

This is demonstrated for several cosmological models in Figure 6-1. This figure shows that even for the same value of H_o, the age of the universe will change by

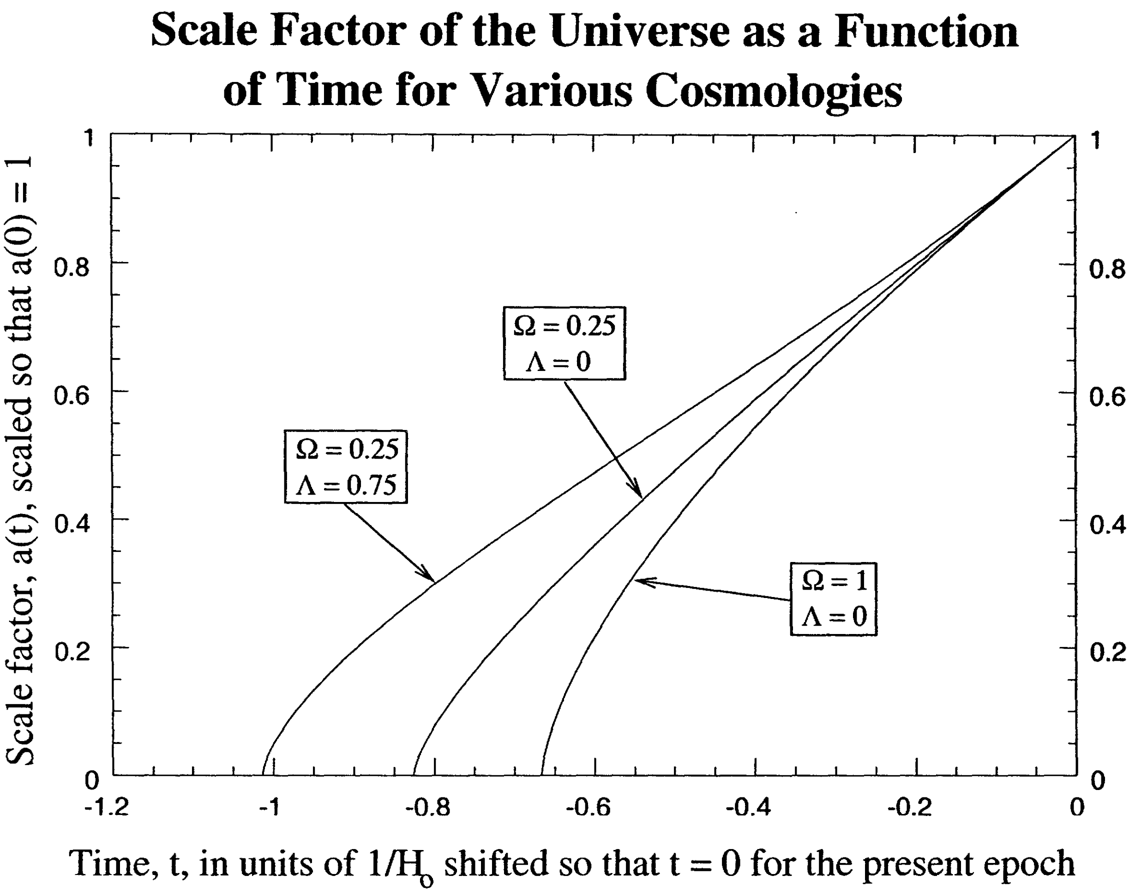

Figure 6-1: The scale factor of the universe for three plausible cosmological models as a function of time. Time, t, is measured in units of $1/H_o$ and shifted so that t = 0 at the present epoch. The time in the past at which the scale factor is zero defines the age of the universe for that particular model.

quite a bit depending on the cosmological model used. In Chapter 5, we determined an upper limit for H_o of 68 km/s/Mpc at 95% confidence. This upper limit to H_o corresponds to a lower limit on the age of the universe for each cosmology. This results in a universe that is at least 9.6 billion years old for a flat universe with $\Omega_o = 1$. If $\Omega_o = 0.25$ and $\Lambda_o = 0.75$ then this value of H_o leads to a universe that is a minimum of 13.8 billion years old. For an open universe in which $\Omega_o = 0.25$ and $\Lambda_o = 0$, then the universe is at least 11.0 billion years old. For the two cases where $\Omega_o \neq 1$ the fact that the H_o value implied by our modeling results is different is taken into account.

6.2 Comparison with Other Results

The last few years have seen a flurry of publications of H_o measurements using gravitational lenses (as we have done in this thesis) as well as other methods. Results from gravitational lenses include $H_o = 64 \pm 13$ km/s/Mpc (95% confidence) for 0957+561 (Kundic, et al. (1997)), $H_o = 44 \pm 4$ km/s/Mpc (68% confidence) for PG1115+080 (Schechter, et al. (1997) and Impey, et al. (1998)), $H_o = 59 \pm 7 \pm 15$ km/s/Mpc (95% confidence) for 1608+656, (Fassnacht, et al. (1999) and Koopmans & Fassnacht (1999)) and $H_o = 69^{+13}_{-19}$ km/s/Mpc (95%confidence) for 0218+357 (Biggs, et al. (1999)). Using Cepheid distances to nearby galaxies to calibrate other distance scales has resulted in a value of $H_o = 71 \pm 6$ km/s/Mpc (68% confidence) (Mould, et al. (1999)). Recent work on calibrating the Cepheid distance scale based on a geometric distance to NGC 4258 has resulted in a value of $H_o = 81 \pm 4$ km/s/Mpc (68% confidence) (Maoz, et al. (1999) and Herrnstein, et al. (1999)).

It seems that recently reported values are beginning to center around a value of about $H_o = 70$ km/s/Mpc but there are outliers. Our result of $H_o \leq 68$ km/s/Mpc is on the low end of recently reported measurements however it is consistent. Our best fit value of $H_o = 37$ km/s/Mpc is much lower than any of these results. Interestingly, another measurement of H_o with 0218+357, by Lehar et al. (1999), was also extremely low at $H_o = 20 \pm 20$. A lower value of H_o implies an older universe and larger spacings between galaxies than that for higher values of H_o.

There are several possible explanations for why our H_o measurement is so much lower than other measurements. The time delay, measured by us as well as Biggs et al. (1999), is based on a single feature of the light curve which (given effects such as microlensing and scintillation) could bias the results. Incorrect redshifts for the lens and source in this system are an unlikely explanation because our ratio of source to lens redshift is higher than normal, and if it were lower, our H_o measurement would actually *decrease*. As discussed in Chapter 5, a different mass profile than that for flat rotation curves could also be biasing our answer. Other galaxies have measured mass profiles which, if applied to 0218+357, could increase our H_o measurement by

40% or so. Lehar et al. (1999) determined that there was not likely to be an external sheer of more than about 1% in this system, so it is unlikely that not including an external sheer in our model has biased the results significantly. More detailed study of this lens and others will be needed to resolve this discrepancy in H_o measurements.

6.3 Future Work

Gravitational lensing is a phenomenon that is just beginning to prove useful in experimental cosmology. For individual lenses, there is great room for improvement in the measurement of the time delays and mass modeling which would lead to more and more accurate H_o estimates. And, as more lenses are discovered the distribution of their statistical properties will also begin to constrain many aspects of cosmology.

6.3.1 Improving the Accuracy of the H_o Measurement

The measurement of H_o depends on two independently determined factors, the time delay and the mass model. In the case of 0218+357, both need to be determined with more accuracy in order to constrain H_o to within a significantly smaller range of values than it is currently.

The time delay measurement can be improved in two major ways. First, the accuracy of the flux measurements in the light curves can be improved. This can occur either with longer dwell times on current telescopes, or with the construction of new telescopes with more sensitivity and higher resolution. Perhaps more important however, is obtaining light curves over much longer time intervals. This would result in light curves with many more variation features to match up among the multiple components. It would also minimize the effects of possible one time deviations due to microlensing or scintillation. Again, this could be helped with the construction of new telescopes because the currently most sensitive radio telescope array is the VLA, which changes configuration every few months and therefore cannot continuously monitor lenses for more than a few months. Another option for improving radio monitoring is to use stationary arrays, such as the MERLIN array in England or the

VLBA in North America. These telescopes are not as sensitive as the VLA, but can monitor lenses continuously for years if necessary. As telescopes are improved and as more and more data is acquired, the accuracy of time delay measurements can only increase in time.

As for improvements in the mass modeling of gravitational lenses more data is likely to play a large role. Most lenses, including 0218+357, have not been fully investigated even with existing telescopes let alone new and improved telescopes. For the best chance at accurate lens modeling one would ideally make deep maps of a lens at various frequencies and resolutions and use this complete set of morphological data to constrain the lens mass. One example related to 0218+357 would be to combine the 1.4 GHz VLBA data shown in Chapter 4 and combine it with similar data taken from the Merlin array and possibly even the VLA to increase the number of short baselines. With a data set containing such a large dynamic range of baseline lengths not only would the image fidelity and sensitivity be greatly improved, but the observation would be sensitive to emission on a wider range of angular scales, probably with the result of detecting the Einstein ring in 0218+357 even at 1.4 GHz or higher frequencies. Of course "next generation" telescopes would also help greatly.

Ironically for these times, another limiting factor in lens modeling is the speed of computers used in the modeling. This is a factor because of the large amounts of data used in the modeling and the computationally intensive nature of the modeling process itself. Of course computer speed is increasing exponentially with time, which will certainly allow more complete and sophisticated modeling techniques in the near future. Also of use would be a modeling technique that could use all the data that LensClean uses, but in a more time-efficient manner.

6.3.2 Determining More than the Effective Distance

The estimate of H_o presented in this thesis was based on measuring the effective distance, D_{eff}, of the gravitational lens 0218+357. At no point was the angular diameter distance to either the lens or the source determined individually. This degeneracy can be broken most easily by obtaining independent information on the velocity dispersion in the lensing mass. Recall that the critical radius of the lens is related to the physical qualities of the lens in the following way:

$$b = 4\pi \frac{\sigma^2}{c^2} \frac{D_{LS}}{D_{OS}} \tag{6.1}$$

The critical radius, b, is determined very accurately in the lens modeling as was demonstrated in Chapter 5. If the one dimensional velocity dispersion, σ, can be determined, then the ratio $\frac{D_{LS}}{D_{OS}}$ could then be solved for, allowing one to isolate the angular diameter distance to the lens, D_{OL}, from the effective distance, D_{eff}. The most straightforward way to measure σ is to obtain optical spectra of the lensing galaxy and measure the widths of the absorption lines. The width of the lines indicates the range of frequencies that line emits and therefore the range of Doppler shifting due to the radial velocity dispersion of the stars and gas in the galaxy. For most high redshift galaxies, this takes a great amount of time on a telescope with large collecting area. In some cases it is beyond the capability of current telescopes.

The advantage of isolating D_{OL} from D_{eff} is most evident when this measurement can be made for several gravitational lenses at a variety of lens redshifts. This allows one to construct an empirical plot of angular diameter distance versus redshift, which could determine not only H_o, but also the expansion rate of the universe at times in the past which would help determine both Ω_o and Λ_o.

6.4 Summary

The original goal of this thesis was to use gravitational lensing to measure H_o. Considering what is being measured, the method is amazingly simple. It comes directly from the first principles of cosmology and general relativity with virtually no reliance on independent empirical data such as intermediate distance indicators, many of which cannot be derived from first principles (for example the Cepheid frequency-luminosity relation, the assumption that Type 1a supernovae are standard candles, the Tully-Fisher relation, etc...). Therefore this method is completely independent of all other methods of measuring H_o, which provides (if nothing else) a very valuable check on other efforts in experimental cosmology.

For all its theoretical simplicity, it is in practice a challenging measurement to make. In the process, one needs to be able to reliably measure the flux density of the variable components to an accuracy many times greater than the average flux density variation, which is often only a few percent of the total flux density (see Chapter 2). Accomplishing this only produces light curves. Deriving the time delay from these light curves is a complex statistical process, for which no standard method has emerged either for measuring the best fit time delay or determining the error bars for that value (see Chapter 3). In order to determine a mass model of the lensing object, the morphology of the multiply imaged emission must be imaged in detail. In our case this was done with separate VLBA observations at 1.4 GHz and 330 MHz to explore the morphology of the Einstein ring and the radio cores (see Chapter 4). We then used another statistical algorithm, LensClean, to determine the best fitting parametric model of the lens potential (see Chapter 5). In this thesis, we describe our efforts to accomplish each of these steps for the gravitational lens 0218+357. The final result is a measurement of Hubble's Constant with a value of $H_o \leq 68$ km/s/Mpc at 95% confidence.

This project is also intended to be an exploration of many of the steps needed to investigate many other areas of science in addition to H_o. First of all, extremely accurate light curves taken of two objects known to be images of the same source could be compared to investigate propagation phenomenon, such as microlensing and scintillation. Lens modeling itself promises much in the efforts to determine the mass distribution in galaxies, clusters of galaxies and even the universe as a whole. Finally, as mentioned above, in combination with independent data about the velocity dispersion in the lensing object, the angular diameter distance to the lensing object can be measured directly. Therefore, gravitational lenses could become distance markers across the known universe, helping us to understand the geometry and dynamics of the universe as a whole.

REFERENCES

Biggs, A. D., Browne, I. W. A., Helbig, P., Koopmans, L. V. E., Wilkinson, P. N. & Perley, R. A. 1999, MNRAS, 304, 349

Fassnacht, C. D., Pearson, T. J., Readhead, A. C. S., Browne, I. W. A., Koopmans, L. V. E., Myers, S. T. & Wilkinson, P. N. 1999, ApJ, 527, 498

Herrnstein, J. R., et al. 1999, Nature, 400, 539

Impey, C. D., Falco, E. E., Kochanek, C. S., Lehar, J., McLeod, B. A., Rix, H. -W., Peng, C. Y. & Keeton, C. R. 1998, ApJ, 509, 551

Koopmans, L. V. E. & Fassnacht, C. D. 1999, ApJ, 527, 513

Kundic, T. , et al. 1997, ApJ, 482, 75

Lehar, J., Falco, E., Kochanek, C., McLeod, B., Munoz, J., Impey, C., Rix, H-W., Keeton, C., Peng, C. 1999, Preprint: astro-ph/9909072, accepted to ApJ(Lehár)

Maoz, E., Newman, J. A., Ferrarese, L., Stetson, P. B., Zepf, S. E., Davis, M., Freedman, W. L. & Madore, B. F. 1999, Nature, 401, 351

Mould, J. R. et al. 1999, preprint astro-ph/9909260

Schechter, P. L., et al. 1997, ApJ, 475, L85